UNIVERSITY OF CALIFORNIA SAN DIEGO

Multiscale Computational Modeling of Novel Treatments for Heart Failure with Reduced Ejection Fraction

A dissertation submitted in partial satisfaction of the
requirements for the degree Doctor of Philosophy

in

Bioengineering with a Specialization in Multi-Scale Biology

by

Abigail Elizabeth Teitgen

Committee in charge:

Professor Andrew D. McCulloch, Chair
Professor Ju Chen
Professor Jeffrey H. Omens
Professor Padmini Rangamani
Professor Daniela Valdez-Jasso

2024

The Dissertation of Abigail Elizabeth Teitgen is approved, and it is acceptable in quality and form for publication on microfilm and electronically.

University of California San Diego

2024

DEDICATION

This dissertation is dedicated to my family and friends - I truly could not have done this without you.

EPIGRAPH

Science, for me, gives a partial explanation for life. In so far as it goes, it is based on fact, experience and experiment.

Rosalind Franklin

TABLE OF CONTENTS

LIST OF FIGURES

LIST OF TABLES

ACKNOWLEDGEMENTS

I would like to acknowledge my primary advisor, Dr. Andrew McCulloch, for his guidance, mentorship and support throughout my PhD. His expertise in cardiac biomechanics and modeling was instrumental in my research development. I would also like to thank Dr. Jeff Omens for his feedback, help, and valuable advice throughout my PhD. Additionally, I would like to thank Dr. Ju Chen, Dr. Padmini Rangamani, and Dr. Daniela Valdez-Jasso for serving on my committee and providing feedback on my work.

I would also like to thank Dr. Michael Regnier for his continued mentorship throughout my PhD. His extensive expertise on dATP and cardiac disease was invaluable in guiding my research, and it has been an incredible opportunity to work with him and members of your lab - I truly could not have completed this project without his input. I would also like to thank Dr. Andrew McCammon, Dr. Rommie Amaro, and Dr. Gary Huber for their guidance on the biochemistry and molecular modeling aspects of my work. I would like to acknowledge Dr. Dan Beard for his contributions to the mechanoenergetics piece of my work, and for development of the cellular and ventricular mechanics models that were instrumental in my modeling work.

I would also like to acknowledge the members of the Cardiac Mechanics Research Group who have made my time in San Diego so rewarding, fun, and meaningful. In particular, I would like to thank Dr. Sachin Govil, Dr. Ariel Wang, Dr. Kim McCabe, Dr. Nick Forsch, Dr. Joe Powers, Ethan Kwan, Dr. Stephanie Khuu, and Marcus Hock for their friendship, guidance, and support, and for keeping me sane throughout graduate school.

I would also like to acknowledge Marcus Hock for his many contributions to this dissertation, particularly the MD, MD, and MSM components, and for his advice throughout my PhD. I would further like to thank Dr. Kim McCabe for her mentorship and feedback during my PhD. Her work formed the basis of much of my PhD research, and I could not have carried out this work without her contributions. I would also like to acknowledge Dr. Kevin Vincent for his mentorship and advice. I would also like to thank Jennifer Stowe for her help and support.

I would like to thank my family, Jan Teitgen, Bob Teitgen, and Emma Teitgen for

supporting me throughout college and through my PhD, and for all of their love and guidance. Thank for for always supporting and encouraging me in pursuing my goals, and for all the opportunities you have given me. I would also like to thank my friends for all of their support, and for being here through all of it. Finally, I would like to thank my partner, Will Valdez, for his unconditional love and support throughout this journey. I truly couldn't have done it without you.

Chapter 1, in part, is a reprint of material as it appears in A. E. Teitgen, M. T. Hock, K. J. McCabe, M. C. Childers, G. A. Huber, B. Marzban, D. A. Beard, J. A. McCammon, M. Regnier, and A. D. McCulloch. Multiscale modeling shows how 2'-deoxy-ATP rescues ventricular function in heart failure. *In review at PNAS*, 2024. The dissertation author is the primary investigator and first author of this publication.

Chapter 2, in part, is a reprint of material as it appears in A. E. Teitgen, M. T. Hock, K. J. McCabe, M. C. Childers, G. A. Huber, B. Marzban, D. A. Beard, J. A. McCammon, M. Regnier, and A. D. McCulloch. Multiscale modeling shows how 2'-deoxy-ATP rescues ventricular function in heart failure. *In review at PNAS*, 2024. The dissertation author is the primary investigator and first author of this publication.

Chapter 3, in part, is a reprint of material as it appears in M. T. Hock*, A. E. Teitgen*, K. J. McCabe*, S. P. Hirakis, G. A. Huber, M. Regnier, R. E. Amaro, J. A. McCammon, and A. D. McCulloch. Multiscale computational modeling of the effects of 2'-deoxy-ATP on cardiac muscle Ca^{2+} handling. *J. Appl. Phys.* 134(7):074905, 2023. *Equal contribution. The dissertation author was the co-first author of this publication.

Chapter 4, in part, is a reprint of material as it appears in J. D. Powers, K. B. Kooiker, A. B. Mason, A. E. Teitgen, G. V. Flint, J. C. Tardiff, S. D. Schwartz, A. D. McCulloch, M. Regnier, J. Davis, and F. Moussavi-Harami. Modulating the tension-time integral of the cardiac twitch prevents dilated cardiomyopathy in murine hearts. *JCI Insight*, 5(20):e142446, 2020. The dissertation author was a contributing author on this publication, and contributed computational simulations of WT and D230N twitches, as well as computational predictions on the effects of

modulating crossbridge binding and Ca^{2+} sensitivity.

VITA

2017	Bachelor of Science, Biomedical Engineering, University of Virginia
2017–2018	Whitaker International Fellow, Auckland Bioengineering Institute
2018–2021	Teaching Assistant, Department of Bioengineering, University of California San Diego
2018–2024	Research Assistant, Department of Bioengineering, University of California San Diego
2024	Doctor of Philosophy, Bioengineering with a Specialization in Multi-Scale Biology, University of California San Diego

PUBLICATIONS

K. J. McCabe, Y. Aboelkassem, **A. E. Teitgen**, G. A. Huber, J. A. McCammon, M. Regnier, and A. D. McCulloch. Predicting the effects of dATP on cardiac contraction using multiscale modeling of the sarcomere. *Arch. Biochem. Biophys.*, 695:108582, 2020.

J. D. Powers, K. B. Kooiker, A. B. Mason,, **A. E. Teitgen**, G. V. Flint, J. C. Tardiff, S. D. Schwartz, A. D. McCulloch, M. Regnier, J. Davis, and F. Moussavi-Harami. Modulating the tension-time integral of cardiac twitch prevents dilated cardiomyopathy in murine hearts. *JCI Insight*, 5(20):e142446, 2020.

M. T. Hock*, **A. E. Teitgen***, K. J. McCabe*, S. P. Hirakis, G. A. Huber, M. Regnier, R. E. Amaro, J. A. McCammon, and A. D. McCulloch. Multiscale computational modeling of the effects of 2'-deoxy-ATP on cardiac muscle calcium handling. *J. Appl. Phys.* 134(7):074905, 2023. *Equal contribution.

A. E. Teitgen, M. T. Hock, K. J. McCabe, M. C. Childers, G. A. Huber, B. Marzban, D. A. Beard, J. A. McCammon, M. Regnier, and A. D. McCulloch. Multiscale modeling shows how 2'-deoxy-ATP rescues ventricular function in heart failure. *In review at PNAS*, 2024

A. Stokely, L. Votapka, M. T. Hock, **A. E. Teitgen**, A. D. McCulloch, and R. E. Amaro. NetSci: A library for high performance scientific network analysis computation. *Manuscript in preparation*, 2024.

FIELDS OF STUDY

Major Field: Bioengineering with a Specialization in Multi-Scale Biology

ABSTRACT OF THE DISSERTATION

Multiscale Computational Modeling of Novel Treatments for Heart Failure with Reduced Ejection Fraction

by

Abigail Elizabeth Teitgen

Doctor of Philosophy in Bioengineering with a Specialization in Multi-Scale Biology

University of California San Diego, 2024

Professor Andrew D. McCulloch, Chair

Heart failure is a major healthcare challenge, and most existing treatments mitigate its symptoms without addressing underlying mechanical dysfunction. Therefore, recent advancements aim to directly target the contractile machinery of the heart. In this work, we utilized a combination of multiscale modeling approaches spanning from the atom to whole heart to investigate the therapeutic potential of targeting proteins within the sarcomere to improve cardiac contractile function in heart failure with reduced ejection fraction. We specifically investigated 2-deoxy-ATP (dATP), a potential myosin-activating therapeutic. dATP improves cardiac function by increasing the rate of crossbridge cycling and Ca^{2+} transient decay. However, the molecular

mechanisms of these effects and how therapeutic responses to dATP are achieved, especially for small fractions of dATP, remain poorly understood. This is especially true in heart failure, where energy metabolism is impaired. We utilized a combination of molecular dynamics (MD), Brownian dynamics (BD), and Markov state modeling, to show that dATP increases the actomyosin association rate *via* stabilization of pre-powerstroke myosin. We also showed using MD and BD that dATP acts on the sarcoendoplasmic reticulum Ca^{2+}-ATPase (SERCA) pump to accelerate Ca^{2+} re-uptake into the sarcoplasmic reticulum during cardiac relaxation by increasing the rate of Ca^{2+} association to SERCA. We then employed a spatially explicit model of the sarcomere to show that dATP increases the pool of myosin heads available for crossbridge cycling, increasing steady state force development at low dATP fractions due to mechanosensing and nearest-neighbor cooperativity. We extended our analysis to assess cardiomyocyte mechanics and excitation-contraction coupling, and found that the effects of dATP on SERCA, along with increased myosin recruitment, contributed to improved cell contraction and relaxation. These mechanisms extended to the ventricular level to improve contractility and metabolism, especially in heart failure, where our model of ventricular mechanics and circulation predicted that dATP increased ejection fraction and the energy efficiency of cardiac contraction. We finally extended our approach to demonstrate how our multiscale computational modeling approach can be utilized to provide insight into the link between genotype and phenotype in heart failure and to develop novel therapeutics.

Introduction

0.1 Heart Failure: A Major Healthcare Challenge

Cardiovascular disease is the leading cause of death globally, with 23.6 million people projected to die from stroke and heart disease by 2030 [58]. Further, adults over 40 have a 20% risk of developing heart failure [118]. Heart failure thus remains a significant cause of morbidity, mortality, and cost to the healthcare system [178]. Heart failure is a clinical syndrome with a number of potential causes and contributing factors including coronary artery disease, high blood pressure, and cardiomyopathy [27]. There are several different cardiomyopathies, including hypertrophic cardiomyopathy (HCM), dilated cardiomyopathy (DCM), restrictive cardiomyopathy (RCM), arrhythmogenic right ventricle cardiomyopathy (ARVC), and other non-classified cardiomyopathies. Further, heart failure can be classified as heart failure with reduced ejection fraction (HFrEF) or heart failure with preserved ejection fraction (HFpEF), which guides treatment strategies. There are a variety of causes and underlying mechanisms, as well as phenotypic presentations and responses to treatment for each of these classifications [183]. Thus, there is a need to better understand why different types of heart failure develop, make better clinical predictions, and explore novel treatment options based on these predictions.

0.1.1 Heart Failure with Reduced Ejection Fraction

HFrEF, the focus of this work, comprises approximately 50% of cases of heart failure overall [137]. It is typically defined as heart failure where the left ventricular ejection fraction (EF) is 40% or less. Symptoms of HFrEF include dyspnea, fatigue, exercise intolerance,

and congestion [137]. Typically, patients with HFrEF tend to be younger than patients with HFpEF. Further, male patients, as well as those with a history of myocardial infarction, bundle branch block, or smoking, were more likely to develop HFrEF than HFpEF, while smoking and high blood pressure were equally likely to contribute to HFrEF and HFpEF [17]. Coronary artery disease and hypertension are the largest risk factors for developing HFrEF, followed by cardiomyopathy and other causes such as myocardial infarction and infection [17]. In HFrEF, ventricular contraction is reduced, leading to reduced stroke volume (SV) and cardiac output (CO). This typically leads to compensatory mechanisms such as activation of the renin-angiotensin-aldosterone system [17]. These compensatory mechanisms initially increase CO but can lead to worsening of heart failure in the long term, including increased hypertrophy and fibrosis [17].

The progression of HFrEF also includes alterations in excitation-contraction coupling. In heart failure, it has been shown that the sarcoplasmic reticulum Ca^{2+} ATPase (SERCA) and the plasma membrane Ca^{2+} ATPase (PMCA) are down-regulated, and the Na^{+}/Ca^{2+} exchanger (NCX) is up-regulated. This leads to decreased sarcoplasmic reticulum (SR) Ca^{2+} load, decreasing the amount of Ca^{2+} available for contraction and leading to reduced systolic function. Na^{+} is also elevated in heart failure, and the action potential is prolonged [15, 160, 227].

Further, myocardial energetics are also altered in HFrEF. The myocardium switches from fatty acid oxidation to glucose and lactate utilization, which is more efficient in the short term but leads to mitochondrial uncoupling in the long term. This results in reactive oxygen species accumulation, which has been linked to mitochondrial damage, hypertrophy, and fibrosis. Heart failure also leads to reduced ATP, creatine phosphate (CrP), and Pi levels, and increased ADP levels [40]. The CrP/ATP ratio, which has been shown to be an indicator of cardiac function, is also decreased in heart failure [229]. Generally, there is a linear relationship between ATP utilization and cardiac work rate, but this relationship is altered in failing hearts, which indicates an inefficient transduction of chemical energy from ATP hydrolysis to mechanical work [40, 201]. The failing heart is therefore in a state of energy starvation where mitochondria are

unable to synthesize ATP rapidly enough to maintain normal function. A recent study showed that alterations in energetics can be directly related to changes in mechanics in heart failure, and that modulation of metabolites may restore mechanical function [229, 40, 201].

0.1.2 Genetic Underpinnings of Dilated Cardiomyopathy

DCM, which can lead to the progression of HFrEF, is characterized by ventricular dilation, decreased ventricular wall thickness, tricuspid and mitral regurgitation, and dilated atria, leading to systolic dysfunction, where ventricular ejection is impaired [183]. The incidence of DCM is 36 cases per 100,000 people, and DCM accounts for 8-47% of all heart failure patients; 77% of DCM patients die within 2 years of diagnosis [183]. Heart failure is the most frequent cause of death in DCM, followed by sudden cardiac death [183]. There are a number of causes of DCM including genetics and myocardial damage caused by infections, toxins, metabolic dysfunction, autoimmune disease, and myocardial ischemia [183, 127].

More than 60 genes coding for sarcomere proteins, the cytoskeleton, the nuclear envelope, the sarcolemma, ion channels, Ca^{2+}-handling proteins, and intercellular junction proteins have been identified in DCM [183]. In particular, 35-40% of DCM cases are caused by mutations in sarcomere genes [127]. Several sarcomere mutations leading to DCM have been identified in the thin filament, which often lead to reduced Ca^{2+} sensitivity. The *TNNT2* del210K mutation in troponin (Tn) and *TPM1* D230N mutation in tropomyosin (Tm) are two such mutations [127]. Mutations can also occur in myosin, such as the *MYH7* S532P and F764L mutations, which occur in the myosin head domain. These mutations were shown to lead to reduced ATPase activity and sliding motility, as well as a reduction of myosin motor step size [127]. The net effect of these mutations is thus often a reduction in force production at the protein and sarcomere level, and/or reduced energetic efficiency of contraction. It is not fully understood how we can link genotype to heart failure phenotype, including growth and remodeling of the whole heart over time as a result of a single or multiple mutations. It is also not always well understood how we can use this information to better treat heart failure patients, especially as genetic screening becomes

more common.

0.1.3 Current Treatment Approaches

Most existing treatment strategies for HFrEF slow the progression of the disease or treat its symptoms, but do not fully restore cardiac function [202]. Existing treatments include angiotensin-converting-enzyme (ACE) inhibitors, angiotensin-receptor blockers, and beta-adrenergic blockers to reduce blood pressure, and diuretics to reduce fluid retention [126, 137]. Patients may also require the use of implantable cardiac defibrillators, left ventricular assist devices, cardiac resynchronization therapy, mitral valve repair, or heart transplants in more severe cases [183, 137]. Lifestyle changes may also be recommended [126].

Another treatment strategy is the use of inotropic agents to improve contractility [50]. Digoxin, one such inotrope, acts to increase intracellular Ca^{2+} levels, leading to improvements in cardiac function. However, it can increase mortality rate, and its use has declined in recent years [183]. Other inotropes including dobutamine, norepinephrine, milrinone and levosimendan each have their own potential negative side effects including increased myocardial oxygen consumption and arrhythmogenesis [50, 118, 198].

In recent years, researchers have investigated a new class of ionotropic agents that target myosin directly to improve contractile function while avoiding many of these negative side effects. Omecamtiv mecarbil (OM) is a myosin activator that has been shown to improve contractile function without altering intracellular Ca^{2+} or increasing energy demand on the heart [118, 198]. OM acts by stabilizing the myosin lever arm in the pre-powerstroke state to increase the number of myosin heads that can bind to actin, thus increasing the transition rate from the weakly- to strongly-bound state and increasing force production [118, 226, 162]. Recent studies including a recently completed phase 3 clinical trial have shown that OM is effective at improving ventricular function and promoting reverse remodeling [14, 48]. However, OM may prolong systole at higher doses, which could have deleterious effects such as impairing relaxation. Danicamtiv, a myosin activator similar to OM, has also shown promise in improving

ventricular function, but additional data is needed to determine if it may also prolong systole [14].

0.2 2-deoxy-ATP as a Potential Heart Failure Therapeutic

The naturally occurring nucleotide 2'-deoxy-ATP (dATP) is another candidate myosin activator for treating HFrEF [202]. Experimental studies have shown that dATP is a more efficient energy source for contraction in cardiac muscle [170, 172]. dATP has been shown to have a larger effect on cardiac muscle than skeletal muscle, increasing force production only at sub-maximal Ca^{2+} levels in skeletal muscle [202, 172, 171]. dATP was also shown not to act on cardiac smooth muscle [147]. When ribonucleotide reductase (R1R2), a naturally-occurring enzyme that converts ADP to dADP, was delivered to myocytes using a recombinant adenoviral system, even small increases in dATP (to 1-2% of the overall nucleotide pool), were sufficient to increase myocyte shortening and relaxation, contractile force, and Ca^{2+} sensitivity [97]. dATP thus has several advantages over similar inotropes such as OM, because it improves contractile function without impairing relaxation. Similar results were observed in isolated myocytes from canines and humans [135, 28]. Nowakowski *et al.* [147] saw enhanced contractility, fractional shortening (FS), and EF with no signs of adverse remodeling in a transgenic mouse model over-expressing R1R2. Kolwicz *et al.* [96] found that adenoviral delivery of R1R2 to mice increased systolic function, even at 13 weeks post-transduction. Further, Kodota *et al.* [87] saw similar results in post-MI pigs, with no evident safety or toxicity concerns. Additionally, Lundy *et al.* [112] showed that dATP can diffuse through gap junctions between transduced and non-transduced cardiomyocytes, and found that when human embryonic stem cell-derived cardiomyocytes transduced with R1R2 were transplanted into adult rat hearts *in vivo*, cardiac function was significantly improved. This suggests that dATP could potentially be delivered clinically *via* a targeted gene therapy approach, but additional research and clinical data is needed.

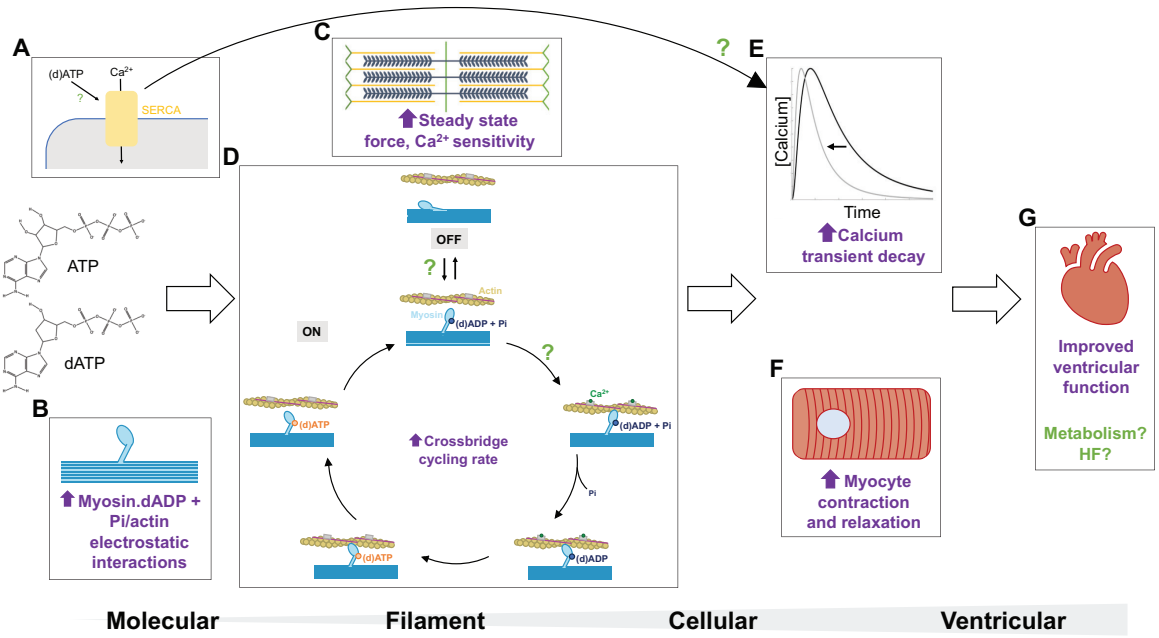

Figure 0.1. Overview of existing data on dATP and remaining questions at multiple scales. Existing information obtained through prior experimentation or computation is highlighted in purple, and remaining questions are highlighted in green.

Despite these promising results, several key questions remain, illustrated in Figure 0.1. dATP has been shown to act on myosin to increase the rate of crossbridge binding and cycling [202], and electrostatic interactions between actin and myosin [167, 148] (Figure 0.1B), but the mechanisms behind this and how small amounts of dATP (1-2% of the overall nucleotide pool) are sufficient to significantly improve sarcomere contraction are not fully understood (Figure 0.1C). Recent studies suggest that dATP may also affect the myosin OFF state [216, 115, 116, 167] (Figure 0.1D), but the mechanisms behind this and the degree to which this leads to improved cellular and ventricular function has not been fully investigated (Figure 0.1F,G). Further, dATP has been shown to increase the rate of Ca^{2+} transient decay, and thus relaxation, in cardiomyocytes [97] (Figure 0.1E), but the mechanisms behind this are unclear, although we have hypothesized that this may be due to dATP acting on SERCA (Figure 0.1A). It is also not known how this translates to changes in contractility and lusitropy at varying levels of mechanical function (Figure 0.1F,G). Additionally, it is not clear whether the increased rate of crossbridge

cycling with dATP treatment exacerbates energy starvation in heart failure, due to faster ATP turnover and/or increasing myocardial oxygen consumption (Figure 0.1G). Further, although it has been demonstrated that altered energetics in heart failure directly contribute to mechanical dysfunction, it is unknown how changes in Ca^{2+} handling with dATP will interact with these effects.

0.3 Multiscale Computational Modeling

A computational modeling approach allows for assessment of the specific mechanisms of small molecules such as dATP or mutations in sarcomeric proteins, and synthesis of information across spatial and temporal scales in a way that would be difficult to accomplish experimentally. Modeling can also be utilized to generate predictions that can be tested experimentally. Significant progress has been made in the past several decades in developing computational models of cardiac behavior at scales ranging from atomistic protein dynamics and protein-protein interactions to patient-specific models of whole heart contraction and excitation-contraction coupling. Still, combining these models into a cohesive, multiscale modeling framework that accurately represents behavior at each of these scales simultaneously and integrates different sources of experimental data remains a major challenge in the field.

0.3.1 Modeling at the Molecular Level

Computational techniques including MD and BD have allowed for simulation of sarcomere proteins including myosin, actin, and their associated regulatory proteins, as well as other proteins involved in excitation-contraction coupling such as SERCA. This has allowed researchers to gain a better understanding of how mutations linked to heart failure in these proteins affect their function, as well as to study how small molecule therapeutics including OM [9] and dATP [147] affect protein dynamics. Molecular dynamics simulations involve solving the equations of motion for each atom in a given protein or system over anywhere from a few femtoseconds to a few microseconds [30]. The major limitation in these simulations is

the computational power needed to run longer simulations for larger atomic systems, although super computing has allowed for significant advances in recent years. Additionally, Gaussian accelerated MD (GaMD) can be utilized to allow for broader conformational sampling [30].

Further, more detailed crystal structures of sarcomeric proteins obtained using X-ray crystallography, NMR spectroscopy, or CryoEM have been solved in recent years, allowing for improved MD simulations. In 2023, a complete structure of the thick filament obtained using Cryo-EM was published, which is a major step forward in the field [44]. Further, a detailed model of the cardiac thin filament has been developed [38]. Still, a complete, atomistic model of actomyosin interactions including the complete thin and thick filaments as well as regulatory proteins has yet to be accomplished, largely because of limitations in computing power. Further, additional work is needed to better understand the structural underpinnings of the myosin OFF state. Recent studies have provided insight into the structure of the interacting heads motif [59, 35], but how this structure may be affected by small molecules or mutations, and how this relates to the super-relaxed (SRX) state of myosin, remain to be determined. Further, detailed structures and MD simulations for SERCA and other Ca^{2+} handling proteins have been published [206], but their molecular interactions with myosin activating drugs have not been widely studied. Some additional limitations can be overcome through homology modeling of structures that are unavailable and by introducing mutations or small molecules *in silico* [30].

BD is another simulation tool that allows for a more coarse-grained assessment of protein-protein or protein-ligand dynamics by modeling molecules of interest as rigid bodies [70]. In BD, electrostatic fields around each protein are estimated, and one of the proteins (or ligands) is placed on a sphere some distance away from the second protein and allowed to diffuse. If the protein of interest comes within a certain reaction distance and satisfies pre-defined reaction criteria, it is considered a binding event. Thousands of these trajectories are simulated, and utilized to estimate a binding constant [70]. The Simulation Enabled Estimation of Kinetic Rates package (SEEKR) is another recently developed computational tool that combines Brownian dynamics with molecular dynamics and milestoning to more accurately estimate association

rates [215]. Additionally, Marov modeling can be utilized in combination with these techniques to investigate protein dynamics [168].

0.3.2 Modeling at the Sarcomere Level

Our current understanding of sarcomere contractile mechanics is largely based on the sliding filament hypothesis developed by Huxley in 1954 [73, 75]. Huxley proposed a model where each myosin head is modeled as a simple spring, which can bind to actin with a rate dependent on its position relative to the actin binding site [74, 76]. The detachment rate also depends on position. The attached myosin head generates force by pulling on actin, and force is calculated with respect to its displacement from the binding site [7, 8]. This model also couples ATP hydrolysis with force production. This foundational modeling framework has been expanded upon over the years to create more complex models of sarcomere mechanics. In 1999, Hunter *et al.* proposed a model of active and passive mechanics based on a variety of experimental data, with the aim of incorporating this model in a larger whole heart model [72, 7]. The Rice *et al.* model, published in 2008, expands upon the original Huxley *et al.* model, and allows for modeling of steady state force-sarcomere and force-Ca^{2+} relationships, steady state force-velocity relationships, isometric twitches, and slack-restretch protocols, where force generated depends on spatial overlap between the thick and thin filaments, thus allowing it to reproduce the length-tension relationship [174]. Similar models incorporating viscoelastic properties, and allowing for modeling of passive and active mechanics, as well as thin filament regulation by calcium, have been developed in recent years [200, 101], using data from rodents and human cardiomyocytes. More detailed models that include mechanisms of cooperativity have also been developed [100, 24], as well as models including the myosin OFF state [131, 22, 201].

Most of these models utilize ordinary differential equations to reproduce the behavior of the sarcomere as a whole, with distribution functions indicating the fraction of crossbridges in a given state at a given time. However, it can also be useful to model the dynamics of each individual myosin head and nonlinear stochastic mechanical properties that vary throughout the

sarcomere. This can be accomplished using Monte Carlo methods [223, 166, 130, 123], which typically significantly increase computational cost but allow for a more detailed representation of sarcomere mechanics and cooperative mechanisms.

0.3.3 Modeling at the Cellular Level

Many computational models of cardiac excitation-contraction coupling (ECC) have also been developed. The Luo-Rudy model developed in 1994 was one of the first such models [113]. More recently developed models incorporate stochastic behavior of calcium channels and graded calcium release [173]. Coupled electromechanics models have also been developed, incorporating both sarcomere mechanics and electrophysiology, including the Nickerson *et al.* 2001 [144] model (based on the Noble *et al.* 1998 guinea-pig electrophysiology model [145]). Further, researchers have developed more detailed continuum models of cell electromechanics [52]. Human cardiomyocyte models have also been developed in recent years, since older models typically relied on rodent data [150, 56, 66, 199]. In addition, detailed mitochondria models can be coupled to mechanoelectric cellular models to assess how excitation-contraction coupling interacts with cellular metabolism [201]. These cardiomyocyte electrophysiology models have been successfully utilized to predict the effects of cardiac drugs on the action potential and screen for potential arrhythmogenicity [122].

Models of SERCA pump function have been developed by several researchers, including the Shannon *et al.* model [184], which has widely been utilized in cellular electrophysiology models. In this model, SERCA flux is reversible and depends on both cytosolic and SR Ca^{2+} concentrations. Tran *et al.* developed a more complex model of SERCA containing more states and formulated based on thermodynamics [210]. This model can be implemented in larger whole-cell electromechanics models.

0.3.4 Modeling at the Whole Heart Level

A number of modeling frameworks for simulating ventricular and whole heart mechanics, as well as the whole cardiovascular system, have been developed. The TriSeg model published by Lumens *et al.* in 2009 [111] utilizes a simplistic representation of the left and right ventricles and septum, where the ventricles are modeled as hemispheres. This allows for changes in shape as the ventricles contract and relax to be calculated using relatively simple geometric equations. This model has also been coupled to the CircAdapt model of the circulation [111], which has also widely been implemented by other researchers. The CircAdapt model is a lumped parameter model, where the ventricles, blood vessels, and valves are represented as resistors and capacitors.

More complex models of the heart can be constructed using a finite element approach, which allows for more complex, realistic geometries and modeling of regional differences in wall mechanics. Finite element models of the heart have significantly improved over the past several decades [140]. The earliest models of the heart used a simplified cylinder [61], which were later extended to axisymmetric geometries[60]. Biventricular models have been developed more recently [98], as well as anatomically relevant four-chamber models [82]. Early models utilized a simple Hill-type active contraction model to simulate cardiac contraction, while more recent models incorporate more complex contraction mechanisms [231]. Patient-specific models can also be developed using cardiac imaging data to reproduce geometry and diffusion tensor MRI data to reproduce fiber architecture [98, 230]. Constitutive models can be utilized to represent behavior at the tissue scale based on this fiber architecture [232]. Recent work has also focused on modeling fluid-solid interactions [146, 88, 169]. Further, detailed whole heart models of cardiac elecrtrophysiology have been utilized to model the electrical behavior of the heart, especially in conditions such as arrhythmia [232]. Still, work remains to be done in creating fully detailed, fully patient-specific, electromechancial finite element models that are relevant in the clinic. Some researchers are moving towards a population-based atlas approach, which may cut down on computational costs and improve clinical predictions [157, 233, 49].

Additionally, growth laws can be incorporated to simulate growth and remodeling over time. This allows for better simulation of conditions like heart failure, which result in morphological changes to the heart over time. Rodriguez *et al.* developed a framework for modeling stress-dependent cardiac growth and remodeling in 1994 [175]. Kerckhoffs *et al.* [93] successfully modeled hypertrophy in a finite element model of the ventricles coupled to a circulation model. Growth laws have been further implemented in modeling hypoplastic left heart syndrome [39], growth in response to hemodynamic overload [228], and in subject-specific models [156].

0.3.5 Integrating Spatial and Temporal Scales

A major remaining challenge is linking these models at varying spatial and temporal scales to create multiscale models. In 2004, Smith *et al.* developed a multiscale computational model of the heart including biomechanics and electrophysiology, using a simplified contraction model [189]. In 2008, Campbell *et al.* utilized a multiscale modeling approach to assess transmural differences in electromechanical function[23]. Sheikh *et al.* [186] utilized models of myofilament Ca^{2+} activation, twitch dynamics, and 3D LV torsion to investigate the role of myosin light chain 2 in regulating regulating cardiac contraction. Sharifi *et al.* [185] recently developed a multiscale model that spans from the level of the sarcomere to the cardiovascular system, with a finite element representation of the left ventricle. This builds upon an earlier multiscale model developed by Campbell *et al.* [21], including a myocyte electrophysiology model, model of sarcomere mechanics, single ventricle model, and lumped parameter circulation model. It also incorporates the baroreflex, which is physiologically important in maintaining arterial pressure. Mann *et al.* [119] recently developed a multiscale framework that incorporates a cellular-level contraction model in a finite element model with detailed, rat-specific geometry, which accounts for the myosin OFF and ON states.

Patient-specific models spanning from the cellular to ventricular scale are progressing towards being utilized in the clinic in assessing the arrhythmogenicity of drugs, and in creating digital twins to facilitate medical device design [89, 156, 34]. However, these models often

lack mechanistic detail below the cellular level, and typically use a simplified active contraction model. For assessment of whether patients should receive cardiac resynchronization therapy, assessment of arrhythmia risk, or similar clinical decision-making this modeling approach may be sufficient, but for assessing the molecular mechanisms of a novel mutation or small molecule therapeutic more detail is needed at the molecular and protein levels. This has largely yet to be accomplished by existing modeling frameworks, especially in the context of inotropic drugs for treating heart failure.

Further, an additional challenge in developing multiscale modeling approaches is determining the appropriate level of detail needed at varying spatial and temporal scales, and choosing models at each scale that are sufficient to answer questions of interest [157]. It is important to consider available data at each scale, and which parameters can be measured or must be fit. Additionally, determining which model outputs at each scale can be utilized to connect to higher level models, especially when linking models developed by different researchers, potentially in different species and based on data from different experimental protocols, remains a major challenge.

In this work, we utilize a novel computational multiscale modeling approach to address several remaining questions about dATP, spanning from molecular mechanisms to biventricular contractile function. This modeling framework serves to address several challenges in integrating models across scales, and includes high levels of mechanistic detail at the molecular and protein levels. Additionally, our approach provides significant advances in specifically modeling an inotrope at each of these scales based on experimental data. We utilize molecular modeling techniques including molecular and Brownian dynamics approaches to assess how dATP affects myosin and SERCA protein dynamics. We then utilize Monte Carlo modeling techniques to translate these molecular level results to changes in sarcomere force, and utilize models of cardiomyocyte mechanics and EC coupling to assess cell-level changes in contraction and relaxation as a result of altered crossbridge cycling and Ca^{2+} dynamics. We then assess how these mechanisms scale to produce changes in ventricular function and energetics in heart failure

using a mathematical biventricular heart model and lumped-parameter model of the circulation. Finally, we demonstrate how this modeling approach can be extended to assess new small molecule therapeutics and treatment options for patients with heart failure.

Chapter 1

Modeling the Effects of dATP on Myosin and the Sarcomere

1.1 Abstract

dATP has been shown to improve contractile function, but the mechanisms by which small amounts of dATP lead to significant improvements in force production are not fully understood. To investigate how dATP affects myosin kinetics and sarcomere mechanics, we utilized atomistic simulations of pre-powerstroke myosin and BD simulations of actomyosin association. These association rates were then incorporated in a mechanistic, spatially explicit Monte Carlo Markov Chain model of cooperative sarcomere contraction, which we modified to include transition dynamics between the myosin ON and OFF states. MD and BD simulations showed that dATP increases the actomyosin association rate by 1.9 fold *via* stabilization of pre-powerstroke myosin. Markov state models predicted that dATP also increases the pool of myosin heads available for crossbridge cycling, increasing steady state force development at low dATP fractions by 1.3 fold. This was shown to be due to thick filament mechanosensing and thin filament nearest-neighbor cooperativity, which had the greatest impact on large increases in force with small amounts of dATP.

1.2 Introduction

dATP has been studied experimentally *in vitro* and *in vivo* and has been shown to improve contractile function, but the specific mechanisms by which dATP improves force production are not fully known [202, 172, 171, 147, 112, 96, 87, 97, 180]. Further, how levels of dATP as low as 1-2% of the ATP pool significantly improve muscle contraction is not well-understood. dATP has been previously shown to affect actomyosin affinity and the overall crossbridge cycling rate, by also increasing the powerstroke rate and detachment rate [123]. dATP has also been shown to increase electrostatic interactions between actin and myosin, but it is not known whether additional mechanisms contribute to the increase in actomyosin association rate [147, 148, 172, 167, 123]. Further, recent studies in cardiac and skeletal muscle suggest that dATP may also increase the pool of myosin available for crossbridge cycling [115, 116, 167, 216].

To investigate these potential mechanisms, we utilized MD simulations and Markov state modeling of pre-powerstroke myosin to assess how dATP affects myosin protein dynamics. We then utilized atomistic BD simulations to estimate the actomyosin binding rate with ATP and dATP. These association rates were then applied to constrain a novel model of thin filament activation and crossbridge cycling, which builds upon previously developed models of the contractile biophysics of the sarcomere [24, 174, 100, 195, 123]. Our model includes a spatially explicit description of the half-sarcomere and detailed description of cooperative mechanisms as in previous iterations of this model developed in our group [123]. We further modified the model to include transition kinetics between the myosin ON and OFF states based on the hypothesized mechanosensing mechanism. Further, this model allows for explicit tracking of ATP throughout the crossbridge cycle, as well as competitive binding of ATP and dATP at varying ratios, as in McCabe *et al.* [123]. This modeling approach allowed us to asses the distinct molecular mechanisms by which dATP acts on myosin to improve force generation.

1.3 Methods

1.3.1 Molecular Dynamics Simulations of ADP.Pi-Myosin and dADP.Pi-Myosin

We first conducted MD simulations of pre-powerstroke ADP.Pi-myosin and dADP.Pi-myosin. Starting coordinates for Atlantic bay scallop (*Argopecten irradians*) myosin II S1 in the pre-powerstroke state (ADP.Pi) were obtained from an X-ray crystal structure in the Protein Data Bank (PDB, www.rcsb.org [13]) solved by [55] (PDB ID: 1QVI, 2.54 Å resolution). The original structure includes myosin II with ADP and vanadate (VO_4) [53], a Ca^{2+}-bound essential light chain (ELC), and a Mg^{2+}-bound regulatory light chain (RLC). The VO_4 ion was replaced with inorganic phosphate (Pi). To increase the computational efficiency of simulations investigating motor domain dynamics, myosin II was truncated after residue 810 and residues in the RLC were removed. Then, missing heavy atoms were built using Modeller [221]. These starting coordinates were used to generate an additional system in which ADP was replaced by dADP *via* removal of the 2' oxygen. These systems will be referred to as ADP.Pi-myosin and dADP.Pi-myosin, respectively. Next, hydrogen atoms were modeled onto the structures using the leap module of AMBER and each protein was solvated with explicit water molecules in a periodic, truncated octahedral box that extended 10 Å beyond any protein atom. Finally, Na^+ and Cl^- counterions were added to neutralize the systems and then 120 mM Na^+ and Cl^- ions were added.

All simulations were performed with the AMBER package [26, 177] and the ff14SB force field [117]. Water molecules were treated with the TIP3P force field [85]. Metal ions were modeled using the Li and Merz parameter set [104, 106, 105]. ADP, dADP, and Pi molecules were treated with the GAFF2 force field [220] with custom parameters derived from QM simulations using ORCA [142, 141]. The SHAKE algorithm was used to constrain the motion of hydrogen-containing bonds [63, 133]. Long-range electrostatic interactions were calculated using the particle mesh Ewald (PME) method.

Each system was minimized in three stages. First, hydrogen atoms were minimized

for 1000 steps in the presence of 100 kcal mol^{-1} restraints on all heavy atoms. Second, all solvent atoms were minimized for 1000 steps in the presence of 25 kcal mol^{-1} restraints on all protein atoms. Third, all atoms were minimized for 8000 steps in the presence of 25 kcal mol^{-1} restraints on all backbone heavy atoms (N, O, C_α and C atoms) After minimization, systems were heated to 310 K during three successive stages. In each stage, the system temperature is increased by $\sim$100 K over 100 ps (50,000 steps) using the canonical NVT (constant number of particles, volume, and temperature) ensemble. During all heating stages, 25 kcal mol^{-1} restraints were present on the backbone heavy atoms (N, O, C_α and C atoms). After the system temperatures reached 310 K, the systems were equilibrated over 5 successive stages using the isobaric-isothermal NPT (constant number of particles, pressure, and temperature) ensemble. During the first 4 stages, the systems were equilibrated for 0.4 ns in the presence of restraints on backbone atoms. The strength of the restraints was decreased from 25 kcal mol^{-1} during the first stage to 1 kcal mol^{-1} during the fourth stage. During the final equilibration stage, the systems were equilibrated for 5 ns in the absence of restraints.

Production dynamics for conventional MD simulations were then performed using pmemd in the canonical NVT ensemble using an 8 Å nonbonded cutoff, a 2 fs time step, and coordinates were saved every ps. Simulations were run in triplicate for 2,000 ns each (12 μs net sampling). Unless specified otherwise, simulations were analyzed separately, and the results of replicate simulations were averaged together.

1.3.2 Markov State Model Construction

These triplicate simulations of ADP.Pi-bound and dADP.Pi-bound myosin were used to construct two Markov state models (MSM) for each of the nucleotide conditions (ADP and dADP) (Figure 1.1A). Feature selection to inform these MSM was carried out, focusing on the behavior of the actin binding surface. The cardiomyopathy loop, loop 2, and loop 4, and closure of the cleft have all been associated with myosin binding to actin during the powerstroke [95], [43]. Therefore, we used a collection of these features, based on the distances between their centers of

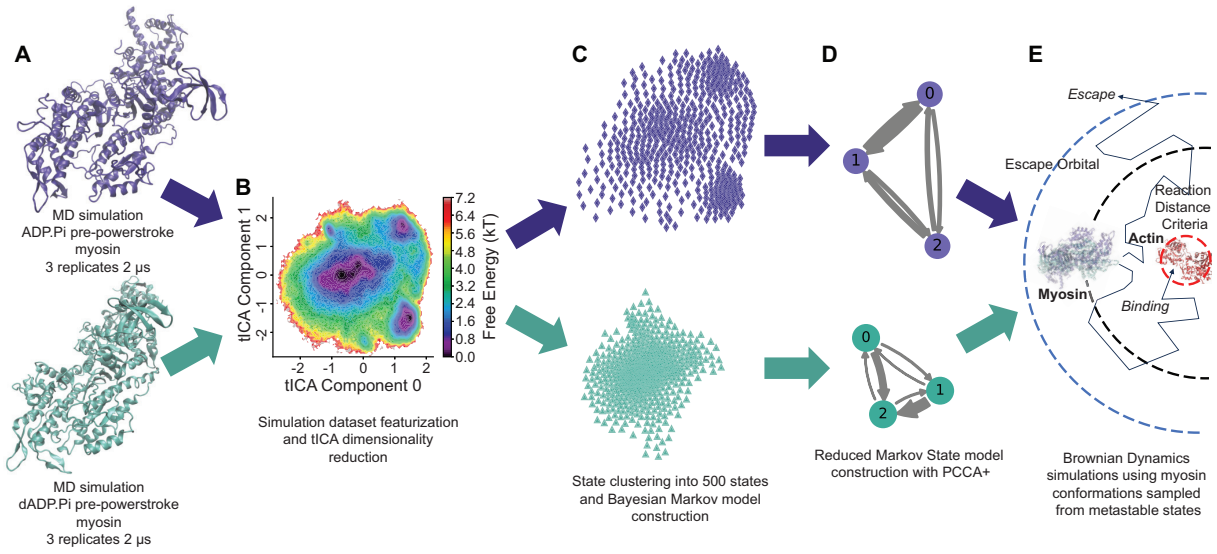

Figure 1.1. Workflow of the MD to Markov state model construction used. The ADP and dADP trajectories were first reduced in dimensions to 22 features measured on different loops and surfaces on the actin binding surface of myosin (A). From the input features, time-lagged Independent Component Analysis (tICA) was used to further reduce the simulation to two dimensions (B). A *k*-means clustering algorithm was used to cluster the MD trajectory into a 500 microstate Markov model using a Bayesian estimation approach (C). PCCA+ fuzzy clustering were used to further reduce the Markov state models of ADP and dADP into 3 metastable state models each (D). From each metastable state, 15 conformations were sampled, and used as inputs to the BD simulations using an ensemble based approach (E). BD simulations were carried out over a range of reaction distances to generate a binding curve.

mass of either the tip, base or entire loops of interest, as well as two different measurements of the cleft opening. To reduce the number of dimensions, time-lagged Independent Component Analysis (tICA) was used to reduce these 22 features to only two primary features, using a time lag of 200 ps (Figure 1.1B). tICA is widely used in MSM construction because it effectively identifies the slow kinetics of MD simulations (as compared to principal component analysis or other dimensionality reduction techniques) [181]. All six trajectories were used in featurization and dimensionality reduction steps.

A *k*-means clustering algorithm was applied to the 2-D tICA spaces, to reduce the MD simulations into 500-state space using the two primary features from the tICA analysis, where each frame of the simulation is classified into one of the 500 states, and transitions between states were counted using a Bayesian approach (Figure 1.1C) [179, 211]. Implied timescales (IT)

analysis was utilized to determine an appropriate lag time for MSM construction. This analysis indicated that at a lag time of 900 ps, the timescales plateaued. Therefore, a lag time of 900 ps was used to construct Markov models for both ADP.Pi-bound myosin as well as dADP.Pi-bound myosin. IT analysis also revealed two major motion components for both ADP and dADP myosin simulations, suggesting that these 500-state MSMs could be reduced to three metastable states (Figure 1.1D). Note that states 0, 1 and 2 are used purely for naming convention, and state 0 in the ADP MSM is not analagous to state 0 in the dADP MSM. A Chapman-Kolmogorov test was used to validate the MSMs, and showed minimal deviation between the observed and predicted transition kinetics within the expected bounds [168]. From each of the three metastable states, 15 frames were sampled to be used in the BD simulations, for both the ADP model and dADP model, cumulatively leading to 45 structures per nucleotide condition to be used in BD simulations (Figure 1.1E). Analysis was carried out in Python using PyEMMA [179].

1.3.3 Brownian Dynamics Simulations of Actomyosin Association

We used rigid body BD simulations to estimate the association rate of pre-powerstroke myosin to actin. In this work, we improved upon previous BD simulations [123] by using an ensemble of representative structures from the MD trajectories that have been sampled from metastable states in the MSM as described above. Traditional approaches using BD typically require a single frame from the MD simulation to be selected and used for the BD simulations. However, our approach using an ensemble of conformations avoids this frame selection challenge. In BD simulations, the first protein of interest (myosin) is placed randomly on a sphere and allowed to diffuse, either binding to the second protein of interest (actin) if it reaches a set reaction distance criteria, or escaping if it reaches a set escape orbital (Figure 1.1E).

BD simulations were carried out with Browndye 2.0 [70]. From each independent conformation sampled from the ADP and dADP MSMs, independent BD simulations were carried out to estimate the association rate between the myosin S1 head and a scallop actin dimer homology model. The homology model was built using the source sequence from *p. magellanicus*

and template structure (PDB ID: 3J8A) [214]. We defined reaction pairs within Browndye based on possible hydrogen bonding pairs within 3.5 Å from sampled conformations within each metastable state of the MSM (15 per metastable state), defined in the bound actomyosin state. The bound state was constructed by aligning the myosin structure with actin using a crystal structure of bound actin and myosin (PDB ID: 6X5Z) as a reference [43]. Alignment was done in VMD [190, 191, 45]. PQR files were created for all structures using the Amber20 force field with PDB2PQR [42, 41]. Electrostatic fields were generated for both myosin and actin structures using APBS [11]. Rather than define a reaction distance, we simulated BD trajectories without a reaction endpoint and recorded the closest distance between actin and myosin during the trajectory in order to calculate association rates at a range of reaction distance criteria. BD simulations were carried out with 250,000 trajectories per conformation, leading to 3.75 million total trajectories for each metastable state of each Markov model, and 11.25 million BD trajectories for ADP and dADP each. The binding curves were then averaged based on the stationary distributions of the metstable states in the three-state MSM for both ADP and dADP. These binding curves were then used for analysis and comparison. The full mechanics and simulation approach of the BD methods are described in more detail in [70].

1.3.4 Spatially Explicit Sarcomere Model

We next modeled the effects of dATP on sarcomere mechanics, incorporating the association rates determined from the BD simulations. To do this, we modified a spatially explicit cooperative model of the sarcomere previously published in our group [123, 24] (Figure 1.2). This model is constructed using a Monte Carlo Markov Chain and contains 26 regulatory units (RUs). Each RU represents seven actin monomers, one myosin S1 head, troponin, and tropomyosin. This model consists of five states: blocked, with no Ca^{2+} bound to the thin filament (B_0), blocked, with Ca^{2+} bound to the thin filament (B_1), closed (C), strongly bound (M_1), and post-powerstroke (M_2). Parameters k_{Ca}^{+} and k_{Ca}^{-} determine transition between B_0 and B_1, representing Ca^{2+} binding to the thin filament; parameters k_b^{+} and k_b^{-} determine the

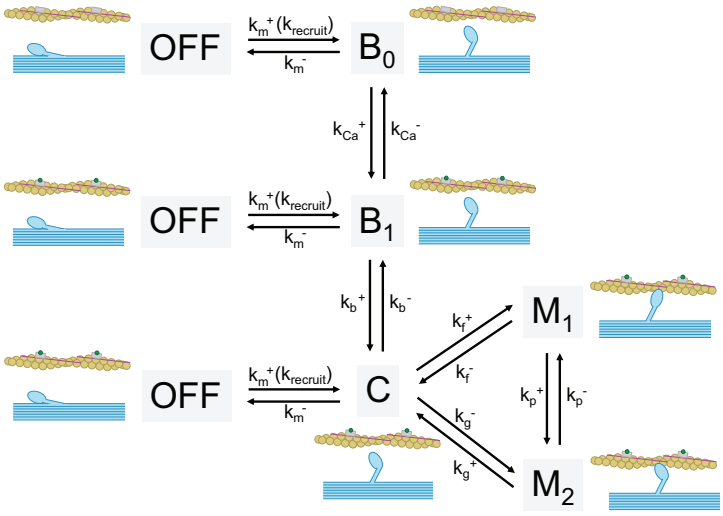

Figure 1.2. Model of spatially explicit cooperative sarcomere mechanics, adapted from [123]. Inactive (OFF) state was added to original model, and parameter k_m^+ is a function of force-dependent parameter $k_{recruit}$ (Equation 1.20). Parameters k_b^+, k_f^+, and k_g^+ depend on nearest-neighbor cooperativity (Equations 1.6, 1.13, and 1.19)

transition between B_1 and C, representing the movement of Tm across the actin surface to expose the myosin binding site; parameters k_f^+ and k_f^- determine the transition between C and M_1, representing myosin binding to actin; parameters k_p^+ and k_p^- determine the transition between M_1 and M_2, representing the powerstroke; parameters k_g^+ and k_g^- determine transition from M_2 to C, representing detachment.

Cooperativity was represented in the model in the same way as in previous studies [24, 123], incorporating mechanisms of both thin filament Tm overlap and strain dependence from neighboring bound myosin heads. Transition rates between states B_1, C, M_1, and M_2 for a given RU depend on the states of the two neighboring RUs. Equilibrium constants for a B to C transition follow the following form:

$$k_{BC}^{XY} = \gamma(XY)k_{BC}^{ref} \tag{1.1}$$

Where k_{BC}^{ref} is defined based on a reference state, which for a B to C transition is where both neighboring RUs are in the C state (and the middle RU is in the B state). This reference

equilibrium constant is thus defined using the Gibbs relation as:

$$k_{BC}^{ref} = exp\frac{-\Delta G_{BC}^{ref}}{RT} \tag{1.2}$$

Additional energy barriers are added if either or both of the neighboring RUs are not in the C state. These energy barriers are represented as cooperative coefficients for different possible combinations of neighboring RUs (X and Y):

$$\gamma(XY) = \gamma(YX) = \begin{cases} \gamma_B^{-2} & B,B \\ \gamma_B^{-1} & B,C \\ \gamma_B^{-1}\gamma_M & B,M \\ 1 & C,C \\ \gamma_M & C,M \\ \gamma_M^2 & M,M \end{cases} \tag{1.3}$$

where

$$\gamma_B = \left(exp\frac{-\Delta G_{BC}^{B}}{RT}\right)^{-1} \tag{1.4}$$

and

$$\gamma_M = exp\frac{-\Delta G_{BC}^{M}}{RT} \tag{1.5}$$

γ_B represents the effect of neighboring RUs pulling the middle RU back into the B state due to Tm filament overlap, while γ_B represents the effect of neighboring RUs in the M state pulling the middle RU into the C state due to strain from bound crossbridges. Finally, these cooperative coefficients are weighted using coefficient q. Thus, for a B to C transition,

$$k_{b+}^{XY} = k_{b+}^{ref} \gamma(XY)^{q} \tag{1.6}$$

$$k_{b-}^{XY} = k_{b-}^{ref} \gamma(XY)^{(q-1)} \tag{1.7}$$

Similarly, for a C to M transition, equilibrium constants follow the following form:

$$k_{CM}^{XY} = \mu(XY) k_{CM}^{ref} \tag{1.8}$$

Where k_{CM}^{ref} is defined based on a reference state, which for a C to M transition is where both neighboring RUs are in the C state (and the middle RU is in the C state). This reference equilibrium constant is thus defined using the Gibbs relation as:

$$k_{CM}^{ref} = exp \frac{-\Delta G_{CM}^{ref}}{RT} \tag{1.9}$$

Additional energy barriers are added if either or both of the neighboring RUs are not in the C state. These energy barriers are represented as cooperative coefficients for different possible combinations of neighboring RUs (X and Y):

$$\mu(XY) = \mu(YX) = \begin{cases} \mu_B^{-2} & B,B \\ \mu_B^{-1} & B,C \\ \mu_B^{-1}\mu_M & B,M \\ 1 & C,C \\ \mu_M & C,M \\ \mu_M^2 & M,M \end{cases} \tag{1.10}$$

where

$$\mu_B = \left(exp \frac{-\Delta G_{CM}^B}{RT} \right)^{-1} \tag{1.11}$$

and

$$\mu_M = exp \frac{-\Delta G_{CM}^M}{RT} \tag{1.12}$$

μ_B is set equal to γ_M to maintain reversibility. μ_B represents the effect of neighboring RUs pulling the middle RU back into the B state due to Tm filament overlap, while μ_M represents the effect of neighboring RUs in the M state pulling the middle RU into the M state due to strain from bound crossbridges. Finally, these cooperative coefficients are weighted using coefficient r. Thus, for a C to M transition,

$$k_{f+}^{XY} = k_{f+}^{ref} \mu(XY)^r \tag{1.13}$$

$$k_{f-}^{XY} = k_{f-}^{ref} \mu(XY)^{(r-1)} \tag{1.14}$$

$$k_{g+}^{XY} = k_{g+}^{ref} \mu(XY)^{(r-1)} \tag{1.15}$$

$$k_{g-}^{XY} = k_{g-}^{ref} \mu(XY)^r \tag{1.16}$$

As described in [123], the Ca^{2+} binding step is not cooperative, and depends only on the Ca^{2+} concentration (Equations 1.17 and 1.18).

$$k_{Ca}^{+} = k_{Ca}^{+ref} \left[Ca^{2+} \right] \tag{1.17}$$

$$k_{Ca}^{-} = k_{Ca}^{-ref} \tag{1.18}$$

The powerstroke rate (k_p^+ and k_p^-) depends on the ATP, ADP, and Pi concentrations in the system, as well as the free energy of crossbridge distortion (Equation 1.19).

$$k_p^- = \frac{k_p^+}{e^{G_{M1}(x) - G_{M2}(x)}} \tag{1.19}$$

where $G_{M1}(x)$ and $G_{M2}(x)$ are the free energy in the M1 and M2 states, respectively, as a result of crossbridge distortion.

In addition to these five states, we added a sixth state to represent the pool of inactive myosin heads not available for crossbridge cycling (OFF). To do this, we incorporated the transition between the active and inactive states based on [22] and [121], governed by parameters k_m^+ and k_m^-, as well as $k_{recruit}$, which describes the force dependence of this transition (Equation 1.20), where $[M_2]$ is the fraction of RUs in the M_2 (post-powerstroke, force-producing) state.

$$k_m^+ = k_m^{+ref}(1 + k_{recruit}[M_2]) \tag{1.20}$$

The transition from ON to OFF is simply defined as

$$k_m^- = k_m^{-ref} \tag{1.21}$$

After addition of this state, all other state occupancies were approximately the same as in the original model formulation, except for a lower occupancy in the C state (Figure 1.3). Model parameters were optimized such that OFF state occupancy is approximately 30% at baseline in the new model, based on experimental measurements. Further description of this model can be found in [123]. External RUs were clamped in the B_0 state, and all other RUs were initially set to the OFF state. 640 simulations were run for steady state force-pCa simulations, and transition probability was determined using a random number from 0 to 1, using a time step of 5×10^{-4} as

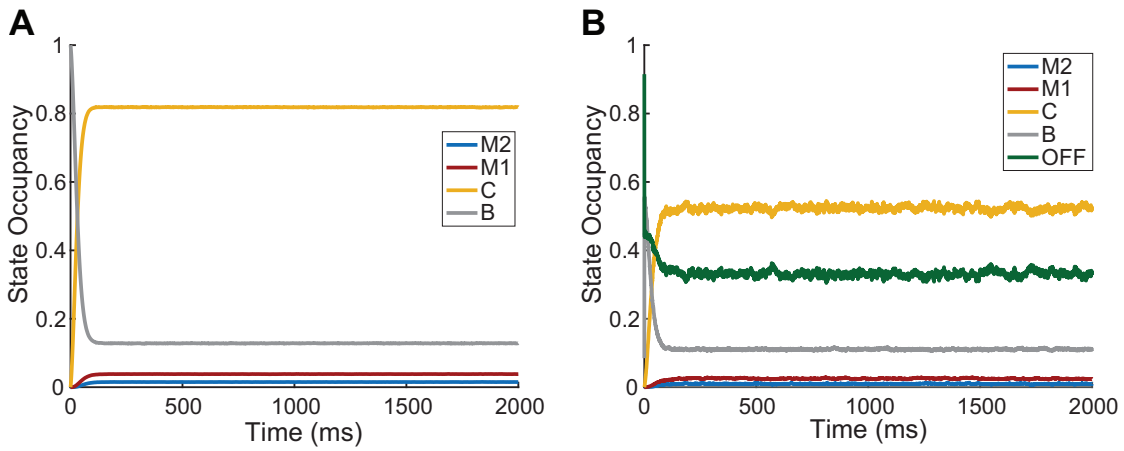

Figure 1.3. State occupancies for original spatially explicit sarcomere model developed by McCabe *et al.* [123] (A) and updated model with inactive (OFF) state added (B). State occupancies are similar between the two models, but occupancy in the C state is reduced in the updated model. Model parameters were optimized such that OFF state occupancy is approximately 30% at baseline in the new model, based on experimental measurements.

in [123]. Analysis was carried out using CUDA 11.7 [149] and Python 3.9.13 [213].

Default parameters from [123] were utilized for this study, except those that were optimized: parameters k_m^+, k_m^-, and $k_{recruit}$ were optimized to match the approximate steady state percentage of myosin heads in the OFF state (30%) based on X-ray diffraction data [216, 116], as well as to match steady state force-pCa data for ATP from [171]. Parameters k_p^+ and k_g^+ were adjusted to simulate dATP treatment in the same way as in [123], further detailed in Table 1.1. $k_{recruit}$ was further adjusted to maximize steady state force with 1% dATP, and k_f^+ was set based on BD results (Table 1.1). Fitting was done to minimize the sum of squared error between data and model and was conducted using parameter sweeps carried out in Python 3.9.13 [213].

Simulations were carried out in the same manner as [123], where the probability of a given transition p_{ij} at a given time step is calculated as:

$$p_{ij} = r_{ij}\Delta t \tag{1.22}$$

where r_{ij} is the reaction rate considering the state of the left and right neighboring RUs

and Δt is the time step. At each time step, a random number between 0 and 1 was generated, and transition probabilities were calculated for each RU based on its current state and the states of its neighbors. For force pCa simulations, maximum steady state force was calculated for a range of Ca^{2+} concentrations based on experimental data from [171]. Hill curve fits were utilized to smooth model outputs for force-pCa simulations.

Table 1.1. Summary of parameter changes made to spatially explicit sarcomere model from [123]. All original parameters from [123] were utilized in updated model after addition of the OFF state, except for transition parameters k_m^+, k_m^-, and $k_{recruit}$, which were optimized to match steady state ATP force-pCa data [171] and to maintain a baseline OFF state occupancy of approximately 30%, based on experimental data [116, 216]. In the updated model, k_f^+ was increased to 478 s^{-1} compared to 567 s^{-1} in the original model based on updated BD data, but k_p^+ and k_g^+ were increased by the same amount to simulate dATP. $k_{recruit}$ was also increased to simulate dATP. Values shown are for 100% dATP.

	Original Spatially Explicit Model		**Updated Spatially Explicit Model**	
Parameter	ATP	dATP	ATP	dATP
k_{Ca}^+ $(\mu M^{-1}\, s^{-1})$	90		90	
k_{Ca}^- (s^{-1})	570		570	
k_b^+ (s^{-1})	13000		13000	
k_b^- (s^{-1})	100		100	
k_f^+ $(M^{-1}s^{-1})$	250	567	250	478
k_f^- (s^{-1})				
k_w^+ $(N^{-1}m^{-2})$				
k_p^+ (s^{-1})	50	80	50	80
k_g^+ (s^{-1})	135	230	135	230
γ_B	45		45	
γ_M	21		21	
μ_M	2		2	
k_m^+ (s^{-1})			16	
k_m^- (s^{-1})			15	
$k_{recruit}$ $(N^{-1}m^{-2}$			0.2	779

1.4 Results

1.4.1 dADP Stabilizes Pre-Powerstroke Myosin, Increasing its Affinity for Actin

A combination of molecular modeling techniques showed that dADP and ADP differentially affect the pre-powerstroke conformation of myosin at a molecular level. Analysis of MSM constructed from three MD trajectories of 2 μs each for ADP.Pi-myosin and dADP.Pi-myosin showed that overall, pre-powerstroke dADP.Pi-myosin has a lower probability of transitioning to a new conformational sub-state (within the pre-powerstroke structure) than ADP.Pi-myosin (Figure 1.4). Specifically, MD featurization and time-lagged Independent Component Analysis (tICA) dimensionality reduction revealed that myosin loop 2 motion is the most important kinetic feature of the actin binding surface on myosin (Figure 1.4A, Figure 1.1). The first two tICA components were therefore utilized to construct three-state MSM for pre-powerstroke ADP.Pi- and dADP.Pi-myosin to capture their major conformational dynamics ((Figure 1.4B, C). Representative conformations from the three states are shown in Figure 1.4G and H. The stationary distribution of the ADP.Pi MSM for states 0, 1 and 2 was 34.1%, 40.7% 25.2%, respectively. However, for the dADP.Pi MSM, the stationary distribution was 5.00% , 8.17%, 86.8% for states 0, 1 and 2, respectively, suggesting that dADP.Pi-myosin is more stable. Further, based on mean first passage time (MFPT) analysis of the transition times between metastable states, the dADP.Pi model shows much more rapid transitions into state 2 as the dominant state, whereas the ADP.Pi model has much more balanced kinetic transitions between all of the states (Figure 1.4E, F). We further found that the overall root mean square fluctuation (RMSF) of the protein was lower overall for dADP.Pi-myosin than ADP.Pi-myosin (Figure 1.4D), supporting the conclusion that dADP stabilizes pre-powerstroke myosin.

An ensemble-based approach was used to carry out rigid body BD simulations of actomyosin association, with conformations sampled from the metstastable states of the MSM. dADP.Pi-myosin showed a significantly higher ensemble-averaged crossbridge formation rate

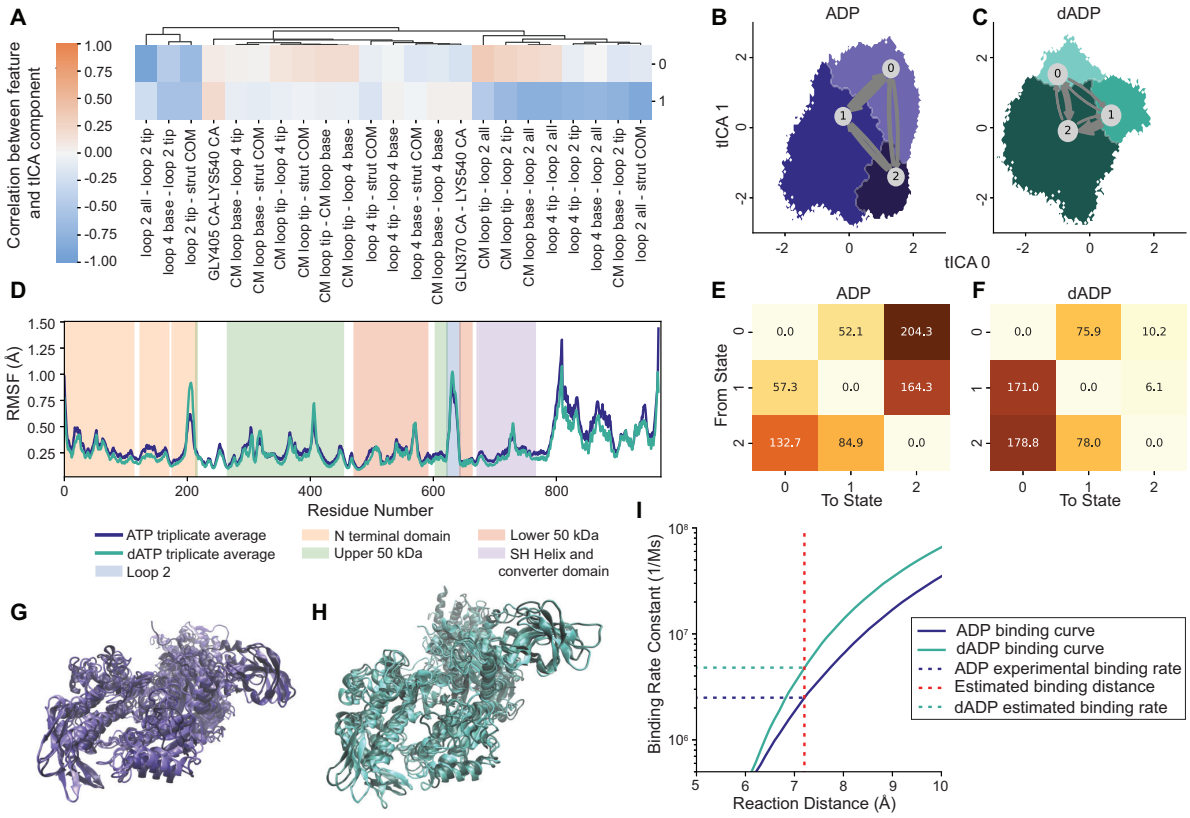

Figure 1.4. MD simulations and MSM demonstrate that binding of dADP.Pi stabilizes the pre-powerstroke myosin head compared with binding of ADP.Pi, increasing its affinity for actin. (A) Correlation analysis between input features from MD simulations (distances between key structural features on myosin) and first (0) and second (1) tICA components. Clustered with 'City-Block' metric. Center of mass is abbreviated as COM, and alpha carbons are abbreviated as CA. (B)-(C) tICA space visualization of MD simulations, with three metastable states shown for each Markov model based on first and second tICA components. Arrows represent flux between states. (D) Root mean square fluctuation (RMSF) shown for ADP and dADP, averaged across three MD trajectories for each. Regions of interest on myosin are highlighted. (E) Mean first passage times between metastable states show in (B) of ADP.Pi-bound myosin simulations (ns). (F) Mean first passage times between metastable states shown in (C) of dADP.Pi-bound myosin simulations (ns). (G) Representative conformations from three metastable states for ADP.Pi-bound myosin. (H) Representative conformations from three metastable states for dADP.Pi-bound myosin. (I) Binding rate constant estimates of myosin binding to actin using BD simulations.

than ADP.Pi-myosin at all simulated reaction distances, where reaction distance is a parameter in the simulation which defines the distance at which the two molecules are considered to bind (Figure 1.1). The previously reported ADP.Pi-myosin.actin association rate of 2.50×10^6 $M^{-1}s^{-1}$ based on experimental measurements [123, 51, 222] corresponds to a reaction distance of 7.17 Å (indicated by the dashed vertical line in Figure 1.4I). Using this reaction distance, the predicted association rate for dADP.Pi-myosin.actin was 4.78×10^6 $M^{-1}s^{-1}$, a 1.9-fold increase over ADP.Pi-myosin.actin. For reaction distances between 6.5 Å and 10 Å, association rates were 1.54 to 2.13 fold greater for dADP than ADP. Thus, our results suggest that dADP increases the actomyosin association rate *via* stabilization of the pre-powerstroke myosin structure.

1.4.2 Increased Force-Dependent Recruitment of Myosin and Nearest-Neighbor Cooperativity Explain Significantly Increased Steady State Tension Development with Low Fractions of dATP

We next assessed how the predicted increase in actomyosin association affects sarcomere mechanics with 1% dATP using a spatially explicit Markov state sarcomere model (Figure 1.2) [123, 24]. After prescribing the ADP.Pi-myosin.actin association rate ($k_f^+ = 2.50\times10^6$ $M^{-1}s^{-1}$) based on reported measurements [123, 51, 222], increasing the actomyosin association rate to 4.78×10^6 $M^{-1}s^{-1}$ as predicted for dADP.Pi-myosin.actin by the BD simulations resulted in an 3% increase in overall sarcomere steady state force at maximal Ca^{2+} activation (Figure 1.5B). A previous study in our group showed using this sarcomere model that dATP increases the crossbridge cycling rate (the powerstroke and crossbridge detachment rates, specifically) in addition to increasing the actomyosin association rate, and that these parameter changes were sufficient to explain experimental changes for simulations with 100% dATP [123]. However, increasing parameters k_p^+ (powerstroke rate) and k_g^+ (detachment rate) in addition to k_f^+ by the same amount as in [123] resulted in an 8% increase in steady state force with 1% dATP. Experimentally, 100% dATP was shown to increase maximum steady state force by 31% in demembranated rat cardiac trabeculae [171]. Experimental data on changes in steady state

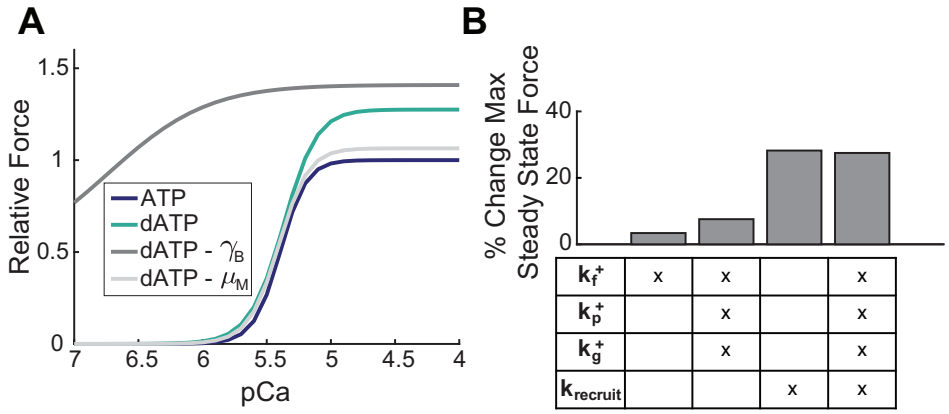

Figure 1.5. dATP increases the pool of myosin available for crossbridge cycling, which leads to disproportionate increases in force with 1% dATP. (A) Model-predicted force-pCa curves are shown for ATP (purple) and 1% dATP (teal). ATP curve was fit to experimental steady state force-pCa data from [171]. dATP simulation includes increases in actomyosin association rate (k_f^+), powerstroke rate (k_p^+), and detachment rate (k_g^+), as well as increased force-dependent recruitment of myosin ($k_{recruit}$). Effects of setting cooperative parameters γ_B and μ_M to one, thus removing their effects from the model, are also shown. (B) Relative contributions of increased crossbridge binding and cycling and increased myosin recruitment to increases in maximum steady state force (at pCa 4.0) relative to ATP. Differences are expressed as percentages relative to ATP.

force with 1% dATP are not available, but given data showing that small fractions of dATP are sufficient to significantly increase force production, we would expect a larger increase in force with 1% dATP. This suggests that although our previous modeling results were sufficient to explain the effects of 100% dATP, additional mechanisms must be considered for small fractions of dATP (Figure 1.5B).

We then modified the model to include the active (ON) and inactive (OFF) states of myosin, and found that increasing parameter $k_{recruit}$ from 0.2 $N^{-1}m^{-2}$ to 779 $N^{-1}m^{-2}$, in addition to k_f^+, k_p^+, and k_g^+, resulted in a 28% increase in steady state force with 1% dATP, which was the maximal increase in force that could be achieved and is close to the observed increase of 31% for 100% dATP (Figure 1.5A, B, additional details found in Table 2.1). $k_{recruit}$ was the only parameter in the model which could be increased to produce such a dramatic increase in steady state force (Figure 1.6). $k_{recruit}$ determines the force dependence of the recruitment of

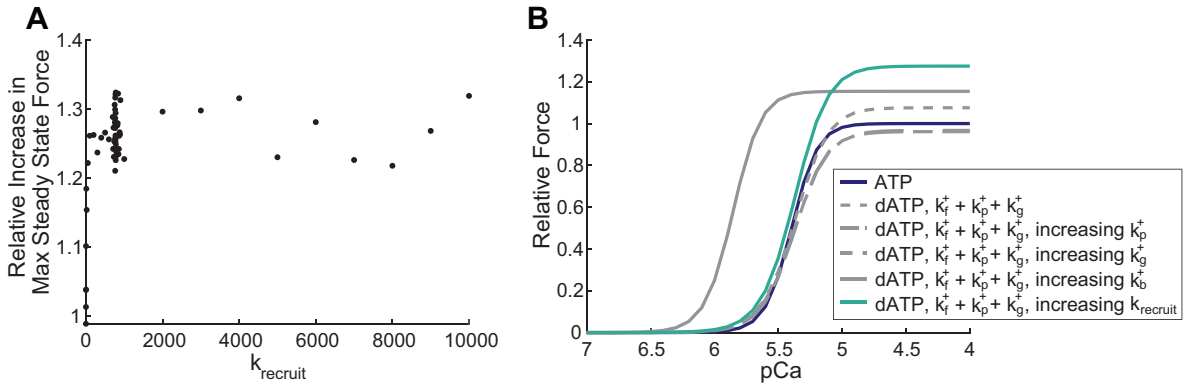

Figure 1.6. Sensitivity analysis of parameter $k_{recruit}$ in spatially explicit sarcomere model. Relative increase in maximum steady state force vs a range of $k_{recruit}$ values. $k_{recruit}$ was set to 779 in the model (for 100% dATP) since this resulted in the maximum increase in steady state force. (B) $k_{recruit}$ is the only parameter in the model which can be increased to produce a disproportionate change in shortening with 1% dATP. Increasing k_p^+ or k_g^+ did not substantially change maximum force, and increasing k_b^+ resulted in a leftward shift of the force pCa curve that does not match experimental observations. k_p^+ was increased to 1.5, k_g^+ was increased to 0.5, and k_b^+ was increased to 30 (to produce the largest possible changes in force).

myosin from the thick filament backbone, and is regarded as a mechanism of thick filament mechanosensing [22]. Previous computational work [167] showed that dATP activates the resting conformation of cardiac myosin, and X-ray diffraction data [116] and fluorescent assays [216] showed decreases in the fraction of myosin heads in an ordered or low ATPase activity state (respectively) with increased dATP [115]. Therefore, our results suggest that dATP-mediated recruitment of myosin to state(s) that can contribute to contraction is the dominant mechanism by which it increases steady state force, especially at low dATP fractions.

We further assessed whether nearest-neighbor cooperativity could explain this increase in steady state force with increased myosin recruitment. After increasing k_f^+, k_p^+, k_g^+, and $k_{recruit}$, we set each of the cooperative parameters (γ_B, γ_M, and μ_M) to one, thus eliminating their effects from the model, and assessed their relative impacts on maximum steady state force. We found that setting γ_B to one resulted in increased steady state force (41% increase relative to ATP) but flattened the force-pCa curve (Figure 1.5A). Further, the fraction of RUs in the B state is decreased relative to the dATP simulation, while the fraction of RUs in the C and M states

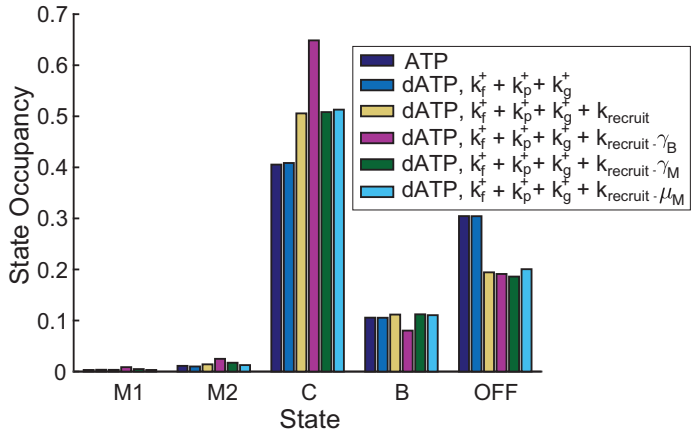

Figure 1.7. Effects of setting each of the cooperative parameters in the spatially explicit sarcomere model (γ_B, γ_M, and μ_M) equal to one, thus removing their effects from the model.

is increased, due to a loss of cooperativity between neighboring Tm molecules, which would normally prevent RUs in the B state from transitioning to the C or M states if its neighboring RUs are also in the B state (Figure 1.7). When γ_M is set to one (γ_M is equal to μ_B in the model to maintain reversibility), the fraction of RUs in the M states goes up, leading to an overall increase in steady state force (Figure 1.7). This is due to the fact that γ_M represents the cooperative effects of neighboring RUs in the M state pulling neighboring RUs into the C state from the B state, while μ_B represents the cooperative effects of neighboring RUs in the B state preventing neighboring RUs from transitioning from the C to M state. Setting μ_M to one resulted in reduced steady state force (6% increase relative to ATP) (Figure 1.5A). The fraction of RUs in the OFF state is increased, and the fraction of RUs in the M states is reduced, due to a loss of cooperativity from neighboring bound crossbridges that would make it more likely for neighboring crossbridges to bind (Figure 1.7).

These results support the hypothesis that by increasing the pool of myosin available for crossbridge cycling, a small fraction of dATP can have a disproportionate effect on sarcomere mechanics by promoting the formation of ATP-myosin.actin crossbridges *via* nearest-neighbor cooperative interactions, both from neighboring bound crossbridges and Tm overlap.

1.5 Discussion and Conclusions

Our modeling approach allowed us to gain new mechanistic insight into the effects of dATP on myosin, which agrees well with previous MD simulations [148, 115, 116, 29]. Featurization and dimensionality reduction analysis using tICA showed that loop 2 motion was the most important kinetic feature in the MD simulations. This could increase actomyosin association rates and possibly other steps in the crossbridge cycle such as nucleotide binding, and warrants further investigation [31]. This aligns with previous work suggesting that switch 1 provides an allosteric mechanism for transmitting changes in the nucleotide binding pocket to loop 2 and the actin binding surface, increasing the electrostatic affinity of myosin for actin [167]. The novel MSM framework utilized in this study therefore allowed us to gain insight into the mechanisms by which dATP increases the actomyosin association rate, suggesting a combination of stabilization of the pre-powerstroke myosin structure and conformational changes in key protein regions, as well as overall changes in electrostatics. Stabilization of the pre-powerstroke state of myosin may also decrease the likelihood of transition back into the OFF state, which could be further investigated in future computational studies.

Interestingly, our BD simulations showed that dATP increases the actomyosin association rate to a slightly lesser extent than was shown previously [123], although our results were generally consistent (we observed a 1.9 fold change in the association rate compared with a 2.3 fold change in [123]). This is likely because our simulations covered a broader range of possible myosin conformations. Further, the metastable conformation that was most dominant in our analysis, state 2 of the dATP simulation, also had the fastest association rate according to our ensemble BD approach. Generally all of these structures in state 2 can be described by having a more pronounced loop 2 extension. Even within this subsample of conformations found in state 2, the conformation that associated most quickly according to the BD simulations had an even greater extension of loop 2 relative to the other structures in the state, again pointing to loop 2 as a key structural and electrostatic feature. This analysis also matches with experimental

assessments of loop 2 function, which highlights how additional positively charged lysines inserted into the loop increases weak binding [84]. This improved method therefore overcomes a major limitation of BD in which molecules are treated as rigid bodies, by accounting for the conformational variability in several distinct sub-states, and allowing us to analyze the impact of structural features on protein-protein association. The accuracy of these simulations could be further improved in the future by including a more complete representation of the thin filament and multiple myosin heads.

Our model predictions indicate that thick filament mechanosensing largely contributes to the disproportionate effects of dATP on force. This has been proposed as a mechanism underlying length-dependent activation, where force development coincides with myosin heads transitioning from the thick filament backbone towards thin filaments [22, 107, 116, 20]. It is plausible that this may explain how elevated dATP leads to increased recruitment of myosin S1 heads from the thick filament backbone, but the underlying mechanism is still unclear. Furthermore, our model predictions indicated that nearest-neighbor cooperativity was also necessary to explain the large increases in force observed at low dATP percentages, which is consistent with results published in [22, 123]. This may point to a mechanism in which a greater number of thin-filament binding myosin heads (with 1% dATP) leads to a greater displacement of Tm, contributing to larger increases in thin filament activation; this in turn allows more myosin heads to bind and generate force, leading to increased recruitment from the thick filament backbone *via* a strain-dependent positive feedback mechanism [167, 22]. Further, our results suggest that myosin recruitment is the dominant mechanism by which dATP treatment leads to large increases in force with small amounts (1%) of dATP, while increases in crossbridge binding and cycling were sufficient to explain experimental data with 100% dATP, as shown previously [123]. This may be due to the fact that relatively low amounts of dATP may be sufficient to fully deplete the inactive myosin pool. Indeed, recent work showed that with 100% dATP, most myosin heads in the inactive pool have likely been recruited [116, 216]. Thus, with 100% dATP, increased crossbridge binding and cycling may be the dominant mechanism by which dATP further increases force production,

since all available myosin heads have already been recruited. A combination of experimental techniques and molecular modeling would allow us to fully explore how dATP interacts with nearest-neighbor cooperativity and the inactive state of myosin at varying percentages.

This modeling approach provided insight into the mechanism by which dATP increases actomyosin association and rate of crossbridge cycling, and our novel BD and MSM modeling approach overcomes many of the limitations of previous BD simulations by better representing a range of possible protein sub-states, which could be further extended in the future to assess novel therapeutics. This study also supports the hypothesis that the main mechanism by which small amounts of dATP lead to disproportionate changes in force is *via* recruitment of myosin into the crossbridge cycling pool, and additional studies in the future may shed more light on the specific mechanisms behind this, including mechanosensing and cooperativity as predicted by our model.

1.6 Acknowledgements

Chapter 1, in part, is a reprint of material as it appears in A. E. Teitgen, M. T. Hock, K. J. McCabe, M. C. Childers, G. A. Huber, B. Marzban, D. A. Beard, J. A. McCammon, M. Regnier, and A. D. McCulloch. Multiscale modeling shows how 2'-deoxy-ATP rescues ventricular function in heart failure. *In review at PNAS*, 2024. The dissertation author is the primary investigator and first author of this publication.

Chapter 2

Multiscale Modeling Shows How 2'-deoxy-ATP Rescues Ventricular Function in Heart Failure

2.1 Abstract

In this study, we extended our previous analysis to assess the mechanisms by which dATP improves ventricular function, and the extent to which molecular and cellular level mechanisms of dATP contribute to changes in contractile function, particularly in heart failure. We further utilized this modeling framework to assess how dATP affects myocardial energetics in heart failure. We integrated cell-scale analysis of myocyte Ca^{2+} dynamics and contraction, organ-scale modeling of biventricular mechanoenergetics, and systems level modeling of circulatory dynamics with our previous findings using MD, BD, and Markov state modeling at the molecular and filament levels. Together with faster myocyte Ca^{2+} handling, increased actomyosin association, crossbridge cycling, and myosin recruitment led to improved ventricular contractility, especially in a failing heart model in which dATP increased EF by 16% and the energy efficiency of cardiac contraction by 1%. Together with the previous chapter, this work represents a complete multi-scale model analysis of a small molecule myosin modulator in the heart from single molecule to organ system biophysics, and elucidates how the molecular mechanisms of dATP may improve cardiovascular function in heart failure.

2.2 Introduction

We showed that at the molecular and cellular levels, dATP increases the rate of crossbridge binding and cycling *via* stabilization of pre-powerstroke myosin, as well as the transition rate of myosin out of the OFF state. Further, dATP has been shown experimentally to speed Ca^{2+} transient decay [97]. This may contribute to faster relaxation of cardiomyocytes post-contraction and/or changes in ventricular lusitropy. It is unclear how the these distinct molecular and cellular mechanisms of dATP integrate into improved ventricular pump function, especially in HFrEF when energy metabolism is typically impaired [229, 40]. It is also not known whether dATP treatment may lead to exacerbated energy starvation in heart failure.

Here, we assess how the molecular mechanisms of dATP interact with altered myocyte Ca^{2+} handling to enhance contractility and lusitropy, using a model of cardiomyocyte mechanics and Ca^{2+} dynamics. We then assess how these myocyte responses contribute to observed improvements in left ventricular mechanoenergetics and hemodynamics in the normal and failing heart by incorporating this cardiomyocyte model into a biventricular mechanics and lumped-parameter circulatory system model. This comprehensive multiscale model analysis of the heart can be used to predict organ system scale cardiovascular function from atomic resolution simulations of molecular mechanisms and shows how very low fractions of dATP are able to significantly improve pump function and efficiency in the failing heart. Our modeling approach may additionally be a useful tool to study other sarcomere-targeted small molecule activators and inhibitors.

2.3 Methods

Figure 2.1 provides an overview of the multiscale modeling approach used for this study, including molecular and filament level modeling detailed in Chapter 1.

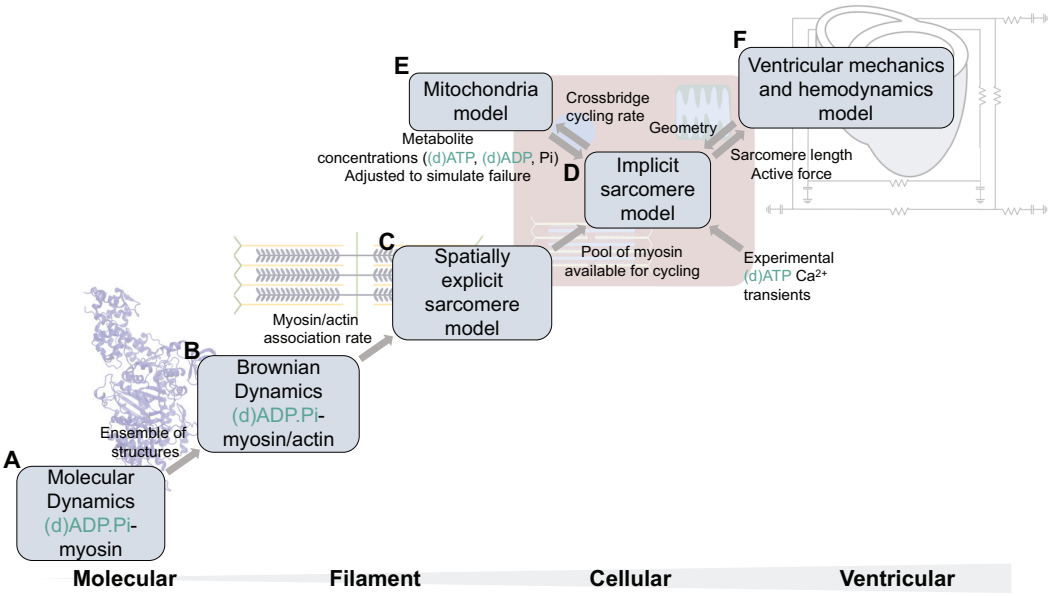

Figure 2.1. Multiscale modeling overview. Gray arrows indicate coupling between models. MD simulations of ADP.Pi-myosin and dADP.Pi-myosin binding to actin (A) in combination with BD simulations (B) were utilized to determine myosin.actin association rate, which was used to constrain a spatially explicit model of cooperative sarcomere mechanics (C). The effects of dATP on myosin predicted by this model were extended to a myocyte model containing an implicit sarcomere mechanics model (D), which is driven by experimental Ca^{2+} data, and is coupled to a mitochondrial energetics model (E). The myocyte model ((D), (E), and experimental Ca^{2+} data) is embedded within a biventricular mechanics and hemodynamics model of the failing heart (F).

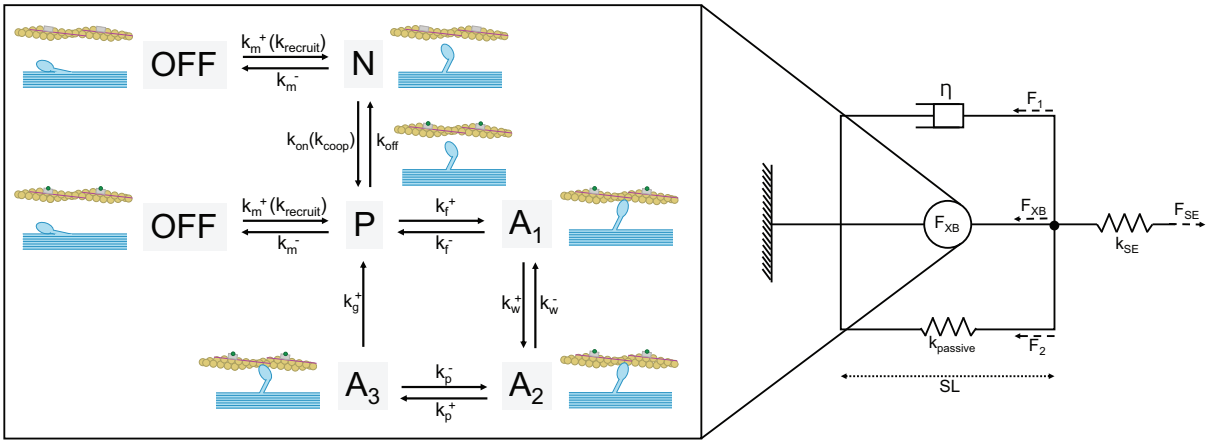

Figure 2.2. Model of implicit sarcomere and viscoelastic mechanics model, adapted from [109, 121]. Parameter k_{on} is a function of cooperative parameter k_{coop}. Parameter k_m^+ is a function of force-dependent parameter $k_{recruit}$ (Equation 2.1).

2.3.1 Myocyte Mechanics Model

We assessed the effects of dATP on whole myocyte mechanics using a non-spatially explicit sarcomere and myocyte mechanics model developed by [109], which is comprised of a system of differential-algebraic equations (DAEs). Analysis was carried out in MATLAB R2018b [77]. ODE15s was used to solve all differential equations. This model consists of six states: inactive (OFF), nonpermissible (N), permissible (P), weakly-bound (A_1), strongly-bound (A_2), and post-ratcheted (A_3) [109, 200, 201] (Figure 2.2).

Parameters k_f^+ and k_f^- determine transition between P and A_1, representing myosin binding to actin; parameters k_w^+ and k_w^- determine transition between A_1 and A_2, representing the transition from weakly-bound to strongly-bound; parameters k_p^+ and k_p^- determine transition between A_2 and A_3, representing the powerstroke; parameter k_g^+ determines transition from A_3 to P, representing detachment. Parameters k_{on} and k_{off} represent Ca^{2+} association to the thin filament and determine transition from N to P, along with a cooperative parameter k_{coop}. This model includes the same model of transition between the active and inactive states as the spatially explicit model utilized in Chapter 1, based on [22] (Equation 2.1), where ON represents the

active states, OFF represents the inactive states, and σ_{XB} represents active contractile force. This model also includes parallel passive and series elastic springs, and a parallel dashpot, to represent sarcomere viscoelasticity. Additional details on this model can be found in [121, 200].

$$\frac{dON}{dt} = k_m^+(1 + k_{recruit}\sigma_{XB})OFF - k_m^- ON \tag{2.1}$$

Default model parameters from the rat model [109] were used for this study, except those that were optimized as described in Table 2.2. Parameters were optimized to match steady state force-pCa rat data from [171] and average unloaded shortening data from [97, 147]. For force-pCa simulations, sarcomere length was fixed at 2.25 μm based on experimental protocols [171], and k_{SE} was set to 5×10^4 mmHg/μm to simulate isometric contraction. k_{on} was set to 50 s^{-1}, $k_{passive}$ was set to 0.1 mmHg/μm, and η was set to 1.5 mmHg/μm to match EC_{50} and steady state force for ATP. For shortening simulations, k_{SE} was set to 35 mmHg/μm, $k_{passive}$ was set to 0.1 mmHg/μm, and η was set to 0.001 mmHg/μm to match FS, RT50, and RT90 for ATP average shortening data. For each simulation, all myosin heads were initially set to the OFF state. Shortening simulations were carried out at 1 Hz for comparison to average shortening data from [97, 147], and the model was run for 3 beats to reach steady state.

$$k_x = k_{x,ATP}[1 - dATP(\%)] + k_{x,dATP}[dATP(\%)] \tag{2.2}$$

Since this model is not spatially explicit, parameters were scaled as functions of dATP level, with overall nucleotide concentrations kept constant according to Equation 2.2, where k_x represents the parameter assumed affected by dATP. Parameter k_f^+ was set based on BD results, and parameters k_f^- and k_w^+ were optimized to mach EC_{50} and steady state force for 100% dATP, further described in Figures 2.3, 2.4, and 2.5.

This achieved the same effect as increasing parameters k_f^+, k_p^+, and k_g^+ in the spatially explicit sarcomere model utilized in Chapter 1. Parameter $k_{recruit}$ was further optimized to match average shortening data for 1% dATP [97, 147]. Optimization was done using a combination of

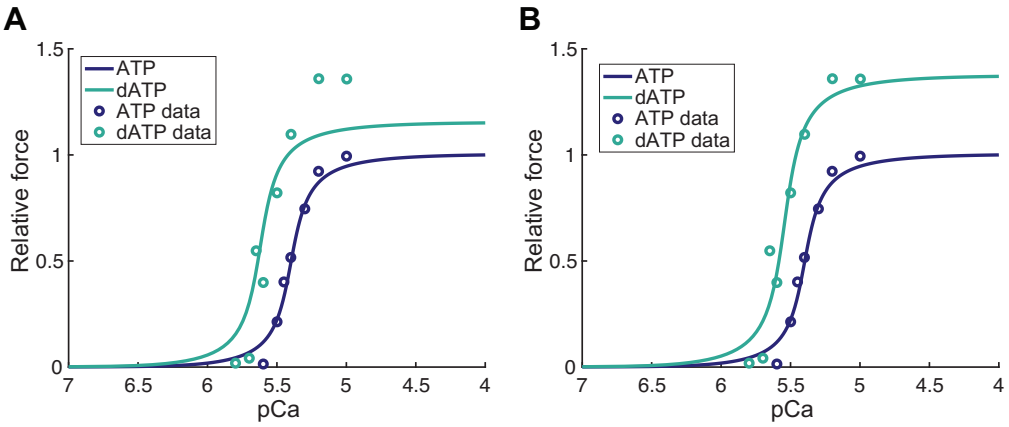

Figure 2.3. Increased actomyosin association rate and crossbridge cycling rate with elevated dATP leads to increased Ca^{2+} sensitivity and steady state force, which agrees with previous modeling results from [123]. Open circles are steady state force-pCa experimental data from [171], solid lines are model predictions for ATP in purple and 100% dATP in teal from spatially implicit sarcomere model. ATP model curve was fit to experimental data, as described in the Methods. (A) Increasing k_f^+ (actomyosin association rate) based on BD simulations results in increased Ca^{2+} sensitivity and maximum steady state force but does not fully explain experimental data. (B): Increasing k_f^- (actomyosin dissociation rate) and k_w^+ (weakly- to strongly-bound transition rate) in addition to k_f^+ in the model gives a better match to experimental data.

manual tuning (to determine a reasonable parameter range) and Particle Swarm Optimization in MATLAB [92]. Some parameter and state names were altered from original model: U_{SR} was changed to OFF, U_{NR} was changed to ON, k_{SR}^+ was changed to k_m^+, k_{SR}^- was changed to k_m^-, k_{force} was changed to $k_{recruit}$, k_a was changed to k_f^+, k_d was changed to k_f^-, k_1 was changed to k_w^+, k_{-1} was changed to k_w^-, k_2 was changed to k_p^+, k_{-2} was changed to k_p^-, and k_3 was changed to k_g^+.

The Ca^{2+} interpolation function from this model (based on experimental data from [83]) was used to simulate Ca^{2+} transients at a range of frequencies for analysis at the cellular and organ levels. We adjusted parameters a, b, c, and Ca_0 in the interpolation function to match DT50 and DT90 for ATP and dATP seen experimentally. Experimental studies have shown varying results on the effects of dATP on Ca^{2+}; Korte *et al.* [97] reported a 50% decrease in DT50 and a 49% decrease in DT90 with elevated dATP, while Nowakowski *et al.* did not report a significant decrease in DT50 or DT90 with elevated dATP. Therefore, to account for the range in experimental values, we averaged these two data points to obtain an average Ca^{2+} transient

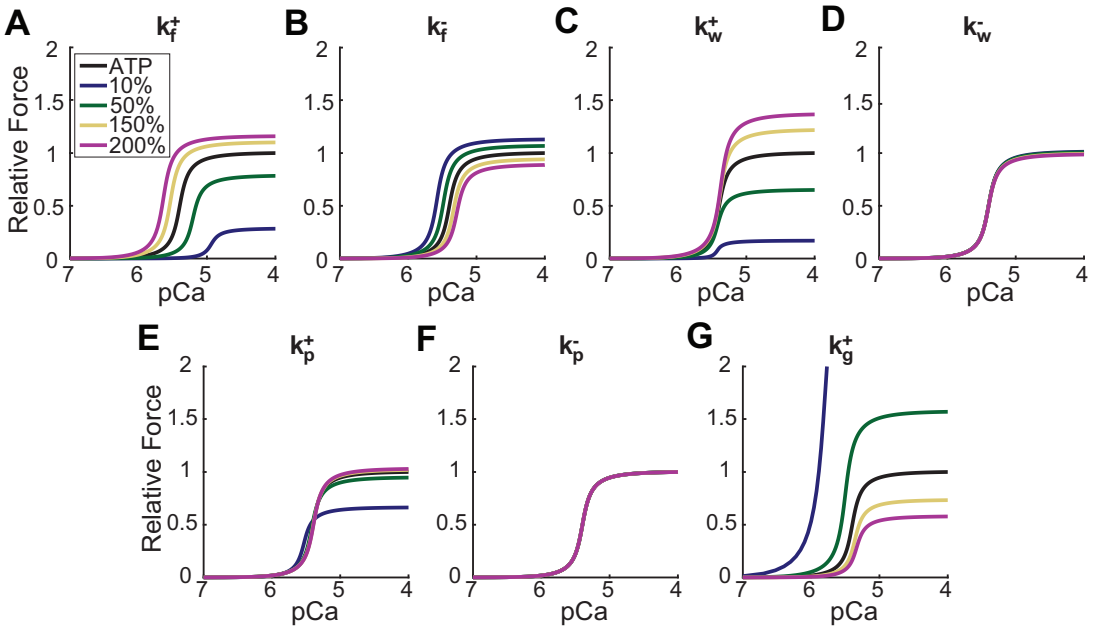

Figure 2.4. Sensitivity analysis showing force-pCa curves for model parameters k_f^+ (A), k_f^- (B), k_w^+ (C), k_w^- (D), k_p^+ (E), k_p^- (F), and k_g^+ (G) in spatially implicit model. Each parameter was scaled to 10% (purple), 50% (green), 150% (yellow), and 200% (pink) of its original value from the baseline ATP simulation (black). Parameters k_f^-, k_w^+, and k_g^+ were shown to be most sensitive and were chosen for further optimization to match dATP data (parameter k_f^+ was constrained by BD data).

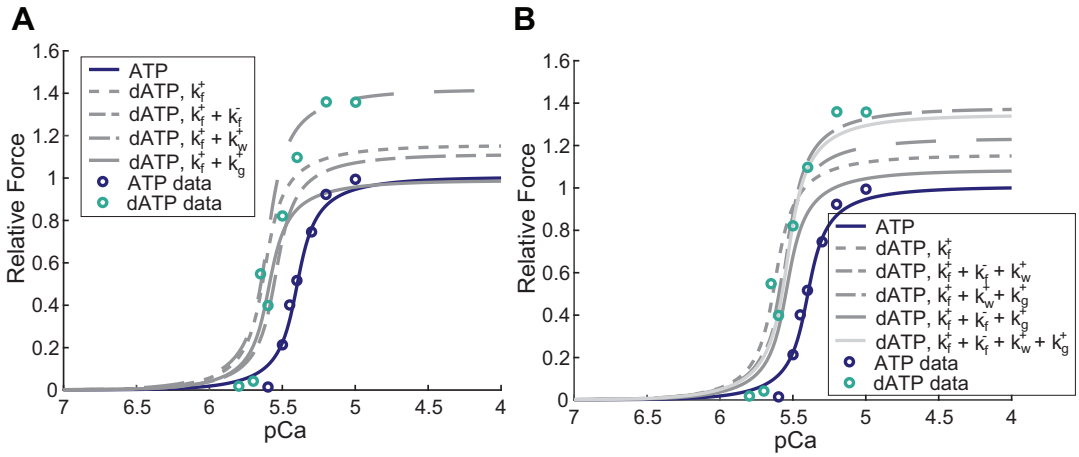

Figure 2.5. Optimizing k_f^- and k_w^+ in addition to k_f^+ in spatially implicit model gives the best fit to experimental force-pCa data. Open circles are experimental data from [171] for ATP (purple) and dATP (teal), and solid purple line is model fit to ATP data. (A) shows the effects of optimizing one parameter (after adjusting k_f^+), and (B) shows the effects of optimizing multiple parameters (after adjusting k_f^+). No single parameter alone is sufficient to match the dATP data. The combined optimization of k_f^- and k_w^+ provides the best fit to the dATP data; optimizing k_g^+ in addition does not substantially change the fit.

for dATP, where DT50 is decreased by 31% and DT90 is decreased by 25%. Corresponding shortening data was also averaged as described above, where average FS for ATP was 7.1 and average FS for dATP was 9.5. For ventricular simulations, we used the original model Ca^{2+} transient from [109], and applied these same relative changes to DT50 and DT90 for dATP. Maximum and minimum Ca^{2+} transient values were set to be equal for ATP and dATP for all simulations since they were not shown to vary significantly experimentally [97, 147]. For cellular-level simulations, minimum Ca^{2+} was set to 0, and maximum Ca^{2+} was set to 1. For organ-level simulations, minimum and maximum Ca^{2+} values were set to be be the same as in the original model from [109].

2.3.2 Crossbridge Energetics and Mitochondrial Metabolism Model

The mitochondria model implemented in Lopez *et al.* [109] (based on [12]) was utilized to simulate myocardial energetics. This model consists of 29 ordinary differential equations describing the membrane potential, metabolite concentrations, and ion concentrations in the mi-

tochondria. The mitochondria is divided into three main compartments: matrix, inter-membrane space, and cytosol. As in [109], metabolite concentrations in the mitochondria model feed into the myocyte mechanics model. The crossbridge cycling rate from the sarcomere model is used to calculate the ATPase rate, which feeds into the mitochondria model. Coupling to the energetics model was only implemented for ventricular simulations. The model from [109] was altered so that the mitochondria model updates the metabolite pools every three beats to allow for assessment of changes in metabolite concentrations over time. Three beats was chosen as a reasonable timescale to allow for a stable solution to model equations. Analysis was carried out in MATLAB R2018b [77].

2.3.3 Ventricular Mechanics and Hemodynamics Model

Ventricular simulations under healthy and failing conditions were carried out using the rat ventricular mechanics and hemodynamics model from [109] (Figure 2.6). This model is based on [111], where the left and right ventricles are modeled geometrically using thin-walled hemispheres with three segments: left ventricular free wall, right ventricular free wall, and the septum. In each of these segments, the implicit sarcomere and energetics model described above is utilized to calculate tension. Thus, sarcomere length and active force from the implicit myocyte model feed into the ventricular model, and the recomputed geometry is used to update sarcomere length in the implicit sarcomere model. This model is also coupled to a lumped-parameter circulation model, which represents the aorta, arteries, capillaries, and veins.

Mean sham rat data from [109] were used for all analysis in healthy simulations, and mean transverse aortic constriction (TAC) rat metabolite data were swapped in for heart failure simulations, as described in [109]. The optimized crossbridge parameters described above for the myocyte mechanics model were also used here (Table 2.2). We also updated the existing passive force formulation in the model (Equation 2.3, 2.4) to produce a more realistic end-diastolic pressure volume relationship, based on [94], where γ was set to 8 to produce a physiologic end-diastolic pressure-volume relationship (Equation 2.5).

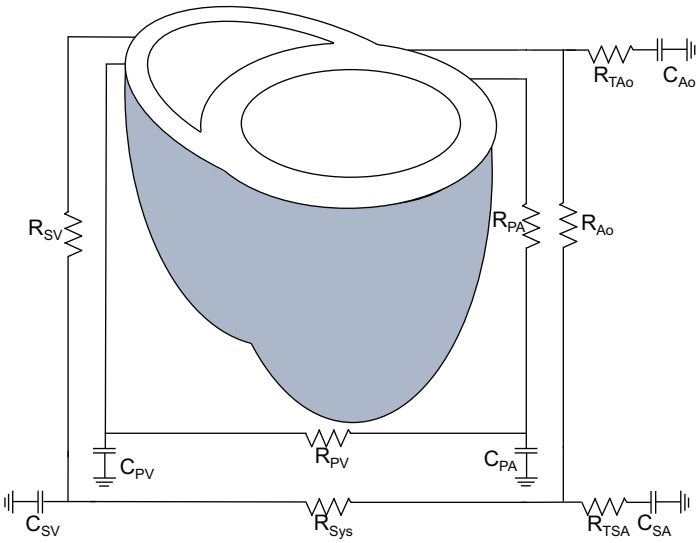

Figure 2.6. Model of ventricular mechanics and circulation, adapted from [109, 121]. Force development in biventricular model is computed using myocyte mechanics model shown in Figure 2.2. Lumped-parameter circulation model is utilized to simulate blood flow, where R_{TAo} is the transmural aortic resistance, R_{Ao} and C_{Ao} are the resistance and compliance of the proximal aorta, R_{PA} and C_{PA} are the resistance and compliance of the pulmonary arteries, R_{PV} and C_{PV} are the resistance and compliance of the pulmonary veins, R_{SV} and C_{SV} are the resistance and compliance of the systemic veins, C_{SA} is the compliance of the systemic arteries, R_{Sys} is the systemic vascular resistance, and R_{TSA} is the transmural systemic artery resistance.

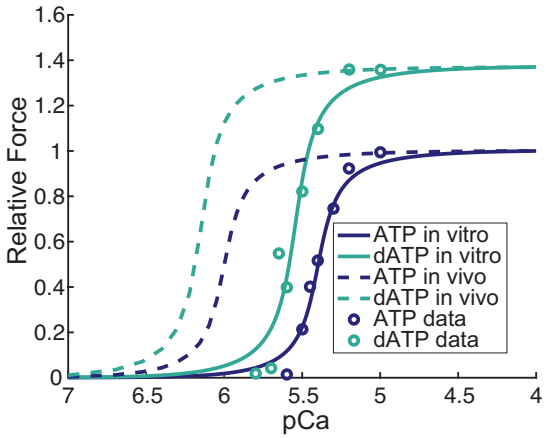

Figure 2.7. Adjusting Ca^{2+} association parameter k_{on} to account for differences between *in vitro* and *in vivo* data, based on [131]. Purple and teal circles are ATP and dATP experimental data from [171], respectively. Purple and teal lines are ATP and dATP original model fits, respectively, used in filament and myocyte simulations. Purple and teal dotted lines are shifted force-pCa curves after shifting Ca^{2+} association parameter for use in ventricular simulations.

Ca^{2+} association parameters were adjusted to account for the differences between *in vivo* and *in vitro* data [131] (Figure 2.7). K_{SE} was adjusted to 1×10^4 mmHg/μm, $k_{passive}$ was adjusted to 5.8×10^4 mmHg/μm, and η was adjusted to 1×10^{-4} (Table 2.2). Further, aortic compliance (C_{Ao}) was set to 0.0015 mL/mmHg and LV, RV, and septal midwall reference surface areas Am_{ref} were scaled by a factor of 1.28 to match the wild-type experimental EF from [147]. All other parameters were kept unchanged, and dATP was simulated in the same way as in the myocyte model. The model was run for 120 beats to reach steady state as in [109]. Analysis was carried out in MATLAB R2018b [77]. Additional details on this model can be found in [121].

$$\sigma_{passive}(SL) = k_{passive}(SL - SL_{rest}) + \sigma_{passive,collagen}(SL) \tag{2.3}$$

$$\sigma_{passive,collagen}(SL) = \left\{ \begin{array}{ll} Pcon_{collagen}[e^{PExp_{collagen}(SL-SL_{collagen})} - 1] & SL > SL_{collagen} \\ 0 & otherwise \end{array} \right\} \tag{2.4}$$

$$\sigma_{passive}(SL) = k_{passive}(SL - SL_{rest})^{\gamma} \tag{2.5}$$

2.4 Results

2.4.1 Increased Myosin Recruitment, Crossbridge Binding and Cycling, and Calcium Sequestering Dynamics are Needed to Explain Improvements in Myocyte Contractility and Lusitropy with Elevated dATP

We utilized an implicit model of sarcomere mechanics and cardiomyocyte Ca^{2+} handling (Figure 2.2) to extend our molecular and filament level findings to the whole myocyte level (Figure 2.1D). This implicit model was chosen because it is less computationally expensive than the spatially explicit sarcomere model utilized in Chapter 1 (Figure 2.1C), and is more comprehensive in its inclusion of a viscoelastic model, Ca^{2+} dynamics, and coupling to a mitochondria

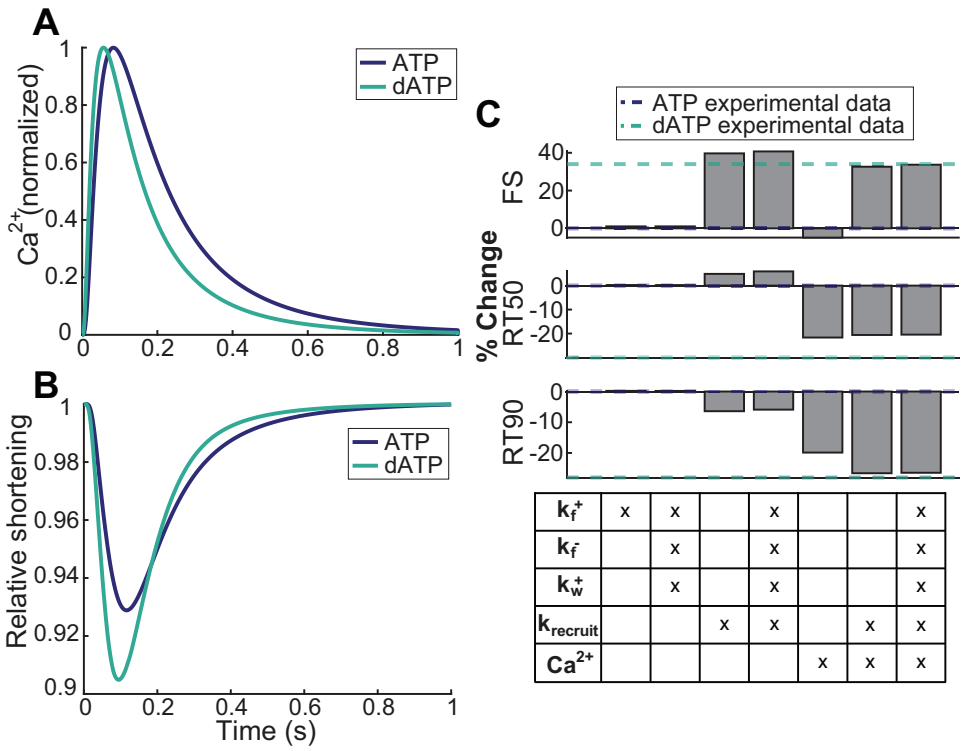

Figure 2.8. Increased myosin recruitment, crossbridge binding and cycling, and Ca^{2+} sequestering dynamics are needed to explain improvements in myocyte contractility and lusitropy with elevated dATP. (A): Model-simulated Ca^{2+} transients for ATP (purple) and dATP (teal), based on average experimental data from [97, 147]. (B): Cell shortening simulations for ATP (purple) and 1% dATP (teal), including increased crossbridge binding (increasing k_f^+) and cycling (increasing k_f^- and k_w^+), faster Ca^{2+} dynamics (shown in (A)), and increased myosin recruitment (increasing $k_{recruit}$). (C): Relative contributions of increased crossbridge binding and cycling, faster Ca^{2+} dynamics, and increased myosin recruitment to changes in FS, RT50, and RT90 compared with average experimental data from [97, 147]. Baseline experimental ATP values are shown as purple dashed lines, and experimental dATP values are shown as teal dashed lines. Differences are expressed as percentages relative to ATP.

model (Figure 2.1E) to allow for cell shortening and whole heart mechanoenergetics simulations (Figure 2.1F). The implicit myocyte model utilized in this study contains an additional cross-bridge cycling state (the weakly-bound state) (Figure 2.2) compared with the spatially explicit model utilized in the previous chapter, and we thus adjusted slightly different crossbridge cycling parameters to achieve the same effect in the implicit model (k_f^+, k_f^-, and k_w^+) as in the spatially explicit model (k_f^+, k_p^+, and k_g^+). More details on these models, including parameter selection, can be found in the Methods and Tables 2.1 and 2.2.

We found that increasing the ADP.Pi-myosin.actin association rate, k_f^+, from 2.50×10^6 $M^{-1}s^{-1}$ to 4.78×10^6 $M^{-1}s^{-1}$ in the myocyte model based on the BD results resulted in only a 1% increase in fractional shortening (FS) with 1% dATP, consistent with our findings using the spatially explicit model (Figure 2.8C). Similarly, increasing parameters k_f^- (actomyosin detachment rate) and k_w^+ (weakly- to strongly-bound transition rate) in addition to k_f^+ did not further increase FS (Figure 2.8C). However, as was the case at the filament scale, we found that increasing parameter $k_{recruit}$ from 0.2 $N^{-1}m^{-2}$ to 37 $N^{-1}m^{-2}$ in addition to k_f^+, k_f^-, and k_w^+ resulted in a 41% increase in FS with 1% dATP (Figure 2.8B, Figure 2.9 and Table 2.2), greater than the experimentally measured increase of 34%. Again, this was the only parameter which could produce this effect (Figure 2.9). This further supports the conclusion that dATP treatment leads to disproportionate increases in force with 1% dATP by disrupting the resting states of myosin, which outweighs the effects of increased crossbridge binding and cycling. However, increased recruitment of myosin with elevated dATP resulted in slowed time to 50% relaxation (RT50) and only explained 21% of the experimental changes in time to 90% relaxation (RT90) [97, 147] (Figure 2.8C), so we next sought to assess additional factors that could explain these changes in relaxation.

When the effects of 1% dATP (99% ATP) on the Ca^{2+} transient were simulated by prescribing the experimental dATP Ca^{2+} transient, which showed decreased time to 50% and 90% Ca^{2+} transient decay (DT50 and DT90, respectively) relative to the 100% ATP transient [97, 147] (Figure 2.8A), RT50 was decreased by 22% and RT90 was decreased by 20%, which

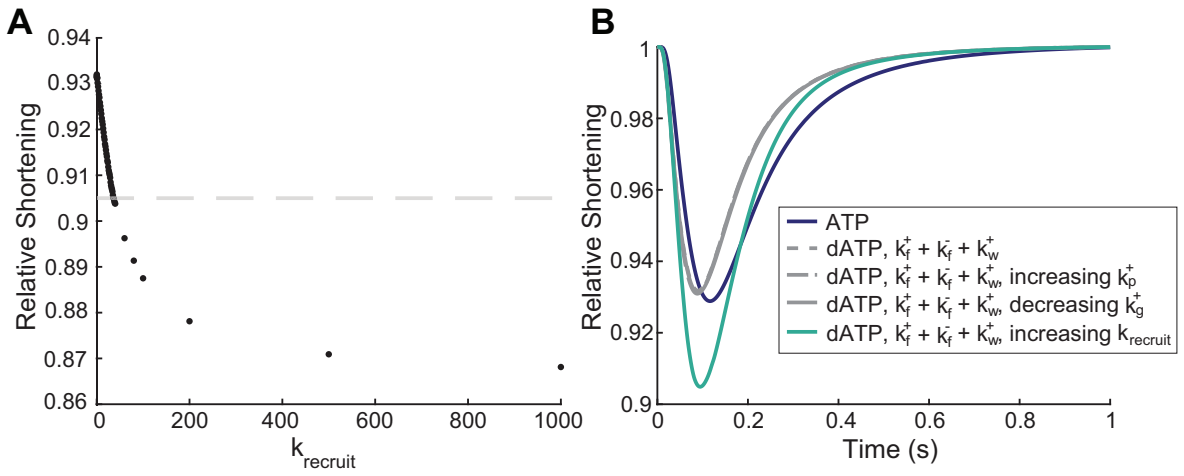

Figure 2.9. Sensitivity analysis of parameter $k_{recruit}$ in implicit sarcomere model. (A) Relative shortening vs a range of $k_{recruit}$ values. $k_{recruit}$ was set to 37 in the model (for 100% dATP) since this matches the average experimentally measured change in shortening, shown with a gray dashed line [97, 147]. (B) $k_{recruit}$ is the only parameter in the model which can be increased to produce a disproportionate change in shortening with 1% dATP. Increasing k_p^+ or k_g^+ did not substantially increase shortening. dATP Ca^{2+} transient was included in dATP model simulations. k_p^+ was increased to 100000, and k_g^+ was decreased to 0.1 (to produce the largest possible changes in force).

is closer to the experimental data [97, 147] (Figure 2.8C). When the more rapid Ca^{2+} dynamics with elevated dATP were combined with an increased crossbridge binding and cycling rate and increased myosin recruitment from resting states, as described above, these three mechanisms together explained 97% of the average experimental increase in FS, 70% of the experimental increase in RT50, and 96% of the experimental increase in RT90 (Figure 2.8B, C). Additionally, including increased rates of crossbridge binding and cycling with elevated dATP in addition to increased myosin recruitment and faster Ca^{2+} transient decay did not substantially change FS, RT50, or RT90 (Figure 2.8C).

Therefore, our model predictions suggest that the integrative mechanisms of dATP on myosin recruitment, crossbridge binding and cycling, and Ca^{2+} sequestering dynamics can explain 100% of the experimental observations of improved contractility and lusitropy with elevated dATP at the myocyte level, as well as the high sensitivity of cardiac muscle to small fractions of dATP.

2.4.2 Increased Myosin Recruitment, Crossbridge Binding and Cycling, and Calcium Sequestering Dynamics with Elevated dATP Contribute to Improved Ventricular Mechanoenergetics

In animal models, the ventricular concentration of dATP has successfully been increased *via* upregulation of the enzyme ribonucleotide reductase (R1R2), which converts ADP to dADP [202]. dADP is then converted to dATP by the normal cellular rephosphorylation process. Elevated dATP has been observed to significantly increase left ventricular developed pressure (LVDevP), CO, and EF in transgenic mice over-expressing R1R2 and infarcted pig hearts treated with R1R2 *via* an adeno-associated viral vector *in vivo* [147, 87]. Therefore, we next utilized our whole heart and circulation model (Figure 2.6) to assess how the predicted effects of dATP on sarcomere and Ca^{2+} dynamics at the myocyte level extend to altered ventricular function. This model contains the same implicit sarcomere and Ca^{2+} handling models utilized for myocyte level simulations (Figure 2.1D), which are further coupled to a mitochondria model (Figure 2.1E) and embedded within a biventricular mechanics and hemodynamics model (Figure 2.1F), as described in the Methods.

After adjusting parameters K_{SE}, $k_{passive}$, η, k_{on}, C_{Ao}, and Am_{ref} in the baseline ventricular model to match experimentally measured EF in mice [147] (all other parameters were kept the same as in the myocyte model), we simulated dATP treatment in the same way as in the myocyte shortening simulations (Table 2.2). We found that increasing k_f^+ from 2.50×10^6 $M^{-1}s^{-1}$ to 4.78×10^6 $M^{-1}s^{-1}$ in the ventricular model based on the BD results led to a $<1\%$ increase in EF, and increasing k_f^- (actomyosin detachment rate), and k_w^+ (weakly- to strongly-bound transition rate) did not further increase in EF (Figure 2.10C). Consistent with our results at the filament and myocyte scales, we found that increasing $k_{recruit}$ from 0.2 $N^{-1}m^{-2}$ to 37 $N^{-1}m^{-2}$ in addition to k_f^+, k_f^-, and k_w^+ led to a 9% increase in EF, which more closely matches experimental data, which showed a 14% increase in EF with dATP [147] (Figure 2.10C).

Interestingly, when we included faster Ca^{2+} dynamics in the ventricular model (Figure 2.10A, B, C) we observed reduced EF, contrary to our findings at the myocyte scale (Figure

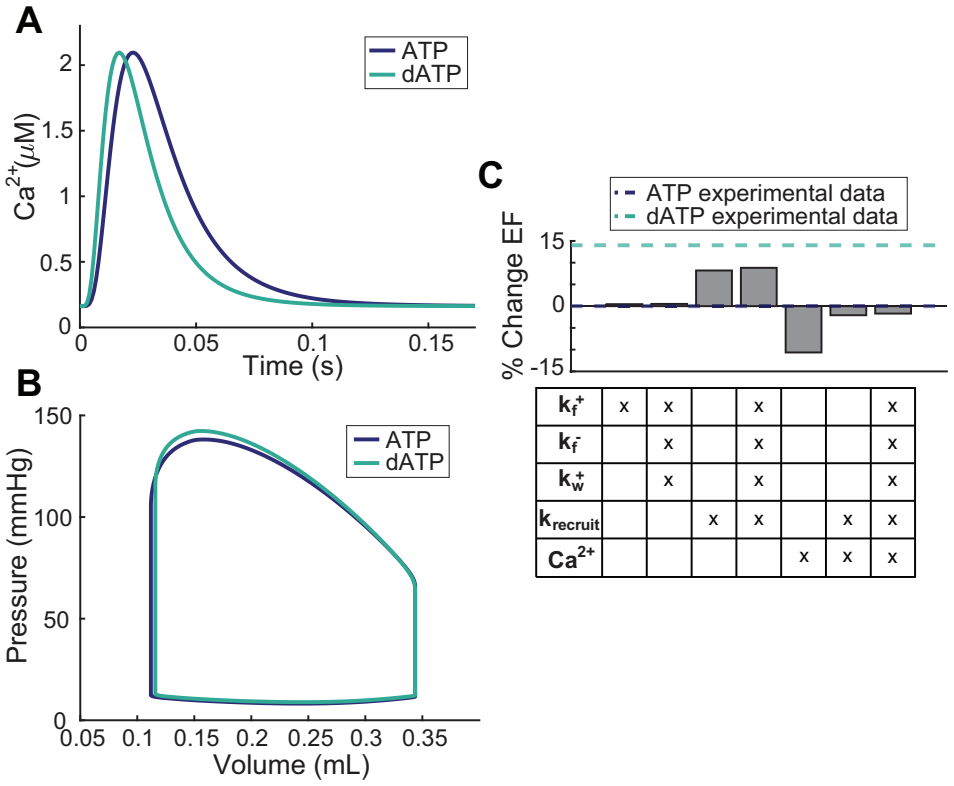

Figure 2.10. Increased myosin recruitment, crossbridge binding and cycling, and Ca^{2+} sequestering dynamics contribute to improvements in ventricular contractility with elevated dATP. (A): Model-simulated Ca^{2+} transients for ATP (purple) and dATP (teal), based on average experimental data from [97, 147]. (B): Pressure-volume loops for ATP (purple) and 1% dATP (teal), including increased crossbridge binding (increasing k_f^+) and cycling (increasing k_f^- and k_w^+), faster Ca^{2+} dynamics (shown in (A)), and increased myosin recruitment (increasing $k_{recruit}$). (C): Relative contributions of increased crossbridge binding and cycling, faster Ca^{2+} dynamics, and increased myosin recruitment to changes in EF compared with experimental data from [147]. Baseline experimental ATP values are shown as purple dashed lines, and experimental dATP values are shown as teal dashed lines. Differences are expressed as percentages relative to ATP.

2.10C). However, these findings are consistent with multiscale modeling results from [21], where increasing the Ca^{2+} reuptake rate into the SR led to reduced EF. The combined effects of dATP on myosin recruitment, crossbridge binding and cycling, and Ca^{2+} sequestering dynamics led to an overall decrease in EF with 1% dATP, likely due to these Ca^{2+} transient effects. However, these results support the conclusion that increased recruitment of myosin from the thick filament backbone is the primary mechanism by which dATP improves contractility.

2.4.3 Elevated dATP Improves Ventricular Function in the Failing Heart in Part Due to Improved Energetic Efficiency

To simulate heart failure, the metabolite concentrations in the model were adjusted to mean values previously measured experimentally in failing rat hearts [109]. This resulted in reduced EF (Figure 2.11A, C). Further, ATP and ADP concentrations were decreased and Pi concentrations were increased, consistent with [109] (Figure 2.11G-I). We found that with 1% dATP in the failing heart model, EF increased by 16%, CO increased by 16%, and LVDevP increased by 13% (Figure 2.11C-E). EF was returned closer to normal with just 1% dATP (61% vs 67% in the baseline healthy simulation), and was returned to 67% with 7% dATP (Figure 2.11C). This aligns well with experimental data in pigs which showed a 16% increase in EF with dATP in failing hearts [87]. Therefore, the mechanisms identified at the molecular (increased actomyosin association), filament (increased recruitment of myosin and faster crossbridge cycling), and cellular (faster Ca^{2+} dynamics) scales were sufficient to explain experimentally measured changes in EF with 1% dATP in the failing heart.

Overall, dATP improved ventricular function in a dose-dependent manner (Figure 2.11). Further, our model was able to predict the effects of varying percentages of dATP on metabolite concentrations and energetic function in the failing heart. ATP levels were unchanged (suggesting that dATP treatment does not substantially deplete ATP pools), while ADP and Pi levels increased with increasing dATP ratio (Figure 2.11G-I), as in [147]. The CrP/ATP ratio was decreased slightly with increasing dATP ratio (Figure 2.11K). Further, myocardial oxygen consumption

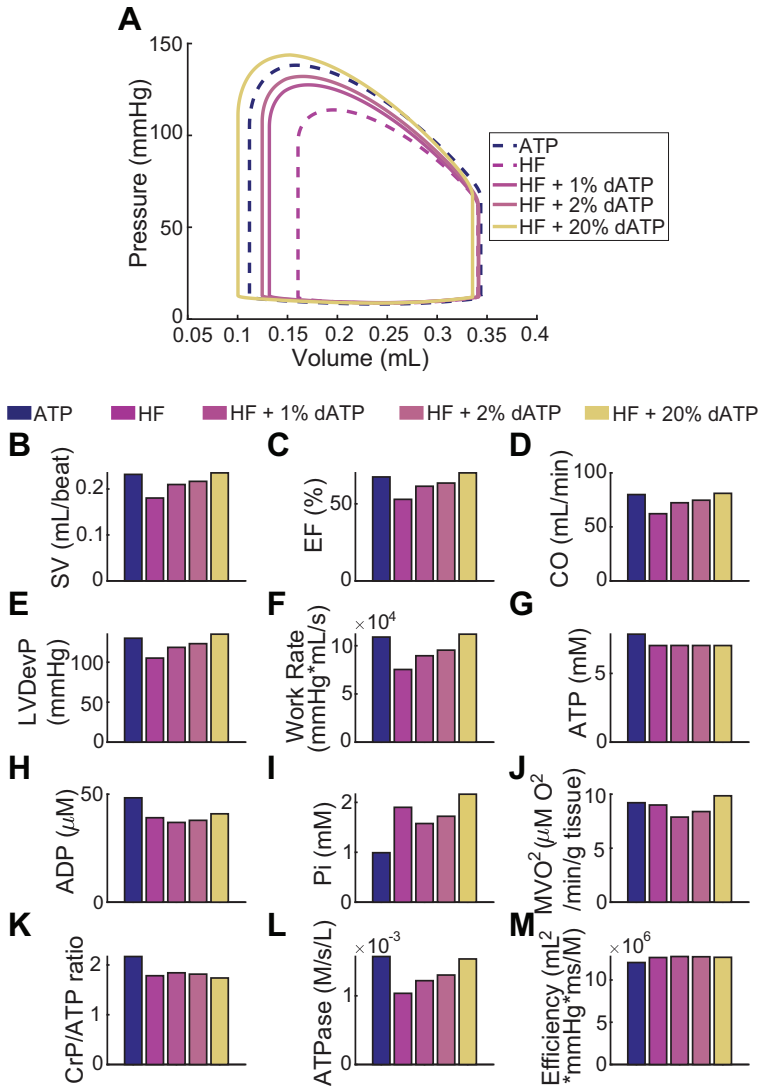

Figure 2.11. Elevated dATP leads to improved ventricular function in failing hearts with 1% dATP, and improves energetic efficiency. (A) Pressure-volume loops for varying ratios of dATP, including increased myosin recruitment (increasing $k_{recruit}$), crossbridge binding (increasing k_f^+) and cycling (increasing k_f^- and k_w^+), and Ca^{2+} sequestering dynamics with elevated dATP. Baseline ATP healthy heart simulation (fit to data from [147]) is shown as a purple dashed line. For heart failure simulations, pink dashed line is baseline heart failure simulation, yellow line is 20% dATP, and color gradient represents increasing ratios of dATP (1%, 2%, and 20%). Varying dATP percentages were simulated as described in the Methods. (B)-(M) Metrics of LV mechanical function and energetics *vs.* dATP ratio, for the same dATP percentages as in (A).

(MVO_2) and ATPase rate also increased with increasing dATP ratio (Figure 2.11J, L). However, with 1% dATP these metrics remained below normal, non-failing levels. Interestingly, efficiency, defined as the work per beat divided by ATP hydrolysis rate, increased with increasing dATP ratio, and was increased by 1% with 1% dATP (Figure 2.11M). This indicates another potential mechanism by which dATP may improve ventricular function in the failing heart, and could explain why dATP treatment does not lead to further metabolic impairment at low dATP fractions.

Finally, we assessed how each of our identified mechanisms of dATP contributed to changes in ventricular function in our normal and failing models. EF, CO, and LVDevP all increased to a greater extent with 1% dATP in failure (16%, 16%, and 13%, respectively) than in the healthy heart simulations where EF was decreased by 2%, CO was decreased by 2%, and LVDevP was increased by 3% compared to ATP (Figure 2.12A, B, C). Further, these results show that increased myosin recruitment has a larger impact in failure, leading to greater improvements in function. Interestingly, faster Ca^{2+} dynamics with dATP treatment led to increased EF in the failing heart simulations, despite decreasing them in the healthy heart simulations (Figure 2.12A, B, C). Increased myosin recruitment also led to greater increases in work rate (Figure 2.12D) and efficiency in the failing heart simulations (Figure 2.12H) (despite decreasing efficiency in the healthy heart simulations), while faster Ca^{2+} dynamics led to a 8% increase in the CrP/ATP ratio (Figure 2.12F) and a 31% decrease MVO_2 (Figure 2.12E) in the failing heart. These findings suggest that the net effect of dATP treatment is to improve contractile function, primarily due to its effects on myosin recruitment, while simultaneously improving energetic efficiency and the overall metabolic state of the failing heart, at least in part due to its effects on Ca^{2+} handling.

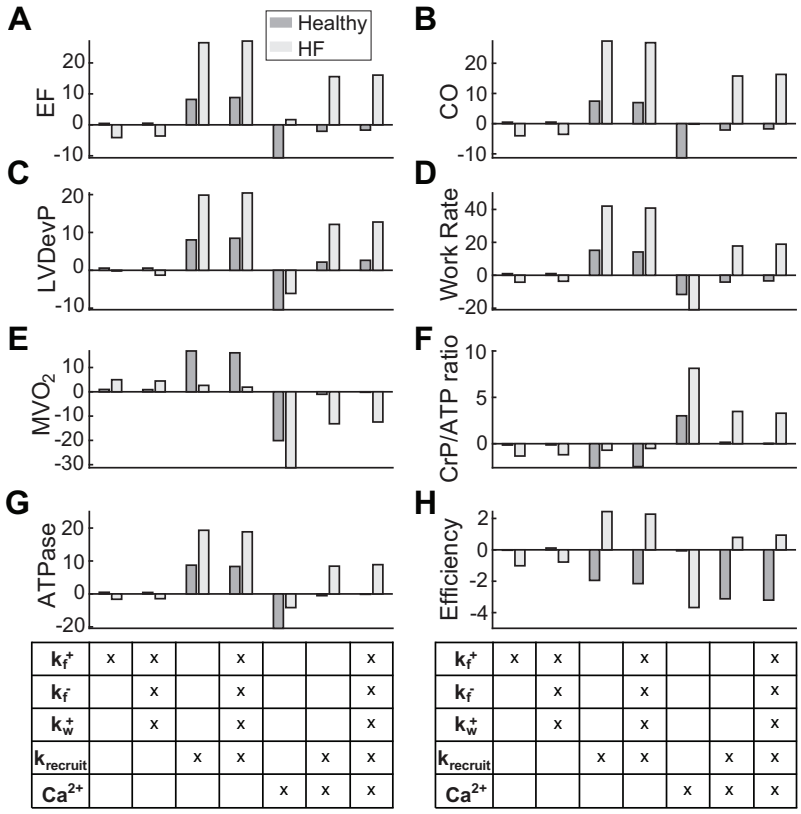

Figure 2.12. Elevated dATP improves ventricular function, especially in the failing heart. (A)-(H): Effects of parameter changes on percent change in metrics of LV function and energetics with 1% dATP in healthy and failing heart simulations, compared to ATP. Parameter changes include increased myosin recruitment (increasing $k_{recruit}$), crossbridge binding (increasing k_f^+) and cycling (increasing k_f^- and k_w^+), and Ca^{2+} sequestering dynamics with elevated dATP.

Table 2.1. Summary of parameter changes made to spatially explicit sarcomere model from [123] compared to implicit sarcomere model from [109]. All original parameters from [123] were utilized in updated model after addition of the OFF state, except for transition parameters k_m^+, k_m^-, and $k_{recruit}$, which were optimized to match steady state ATP force-pCa data [171] and to maintain a baseline OFF state occupancy of approximately 30%, based on experimental data [116, 216]. In the updated model, k_f^+ was increased to 478 s^{-1} compared to 567 s^{-1} in the original model based on updated BD data, but k_p^+ and k_g^+ were increased by the same amount to simulate dATP. $k_{recruit}$ was also increased to simulate dATP. This differs slightly from the parameters increased to simulate dATP in the spatially implicit model (k_f^+, k_f^-, k_w^+, and $k_{recruit}$). Additionally, $k_{recruit}$ was increased by a greater amount in the spatially explicit model than in the spatially implicit model. Values shown are for 100% dATP.

	Original Spatially Explicit Model		**Updated Spatially Explicit Model**		**Spatially Implicit Model**	
Parameter	ATP	dATP	ATP	dATP	ATP	dATP
k_{Ca}^+ $(\mu M^{-1}\, s^{-1})$	90		90			
k_{Ca}^- (s^{-1})	570		570			
k_b^+ (s^{-1})	13000		13000			
k_b^- (s^{-1})	100		100			
k_f^+ $(M^{-1}s^{-1})$	250	567	250	478	250	478
k_f^- (s^{-1})					304.7	460
k_w^+ $(N^{-1}m^{-2})$					112.4	170
k_p^+ (s^{-1})	50	80	50	80	811.7	
k_g^+ (s^{-1})	135	230	135	230	144.6	
γ_B	45		45			
γ_M	21		21			
μ_M	2		2			
k_m^+ (s^{-1})			16		15.5	
k_m^- (s^{-1})			15		50	
$k_{recruit}$ $(N^{-1}m^{-2}$			0.2	779	0.2	37

Table 2.2. Summary of parameter changes made to implicit model from [109] to simulate ATP and dATP compared to original model parameters. ATP and dATP parameters were fit independently. k_f^+ was altered based on actomyosin association rate from BD. k_f^-, k_w^+, and $k_{recruit}$ were optimized to match dATP experimental data [171]. Viscoelastic parameters $k_{passive}$, η and k_{SE} were adjusted based on experimental protocol (force-pCa for filament simulations, shortening for myocyte simulations, and pressure-volume loops for ventricular simulations), as described in the methods. Ca^{2+} association parameter k_{on} was adjusted to account for differences between *in vitro* and *in vivo* data [131]. Parameter values shown are for 100% ATP and 100% dATP. Parameters k_f^+, k_f^-, k_w^+, and $k_{recruit}$ were increased to simulate dATP treatment.

	Original	**Filament Simulations**		**Myocyte Simulations**		**Ventricular Simulations**	
Parameter	ATP	ATP	dATP	ATP	dATP	ATP	dATP
$k_{passive}$ $(mmHg/\ \mu m)$	25	0.1		0.1		5.8×10^4	
k_{coop}	9.68						
k_{on} (s^{-1})	101.2	50		50		200	
k_{off} (s^{-1})	723.9						
k_m^+ (s^{-1})	15.5						
k_m^- (s^{-1})	50						
$k_{recruit}$ $(N^{-1}m^{-2})$	0.2		37		37		37
k_f^+ $(M^{-1}s^{-1})$	559.6	250	478	250	478	250	478
k_f^- (s^{-1})	304.7		460		460		460
k_w^+ (s^{-1})	112.4		170		170		170
k_w^- (s^{-1})	21.3						
k_p^+ (s^{-1})	811.7						
k_p^- (s^{-1})	43.3						
k_g^+ (s^{-1})	144.6						
k_{SE} $(mmHg/\ \mu m)$	5×10^4			35		1×10^4	
η $(mmHg*s/\ \mu m)$	1	1.5		0.001		1×10^{-4}	

2.5 Discussion and Conclusions

In this study, we used multiscale computational modeling to integrate therapeutic mechanisms of dATP from the molecular scale to the cardiovascular system in the failing heart. In Chapter 1, we predicted an increase in the actomyosin association rate with elevated dATP, *via* stabilization of pre-powerstroke myosin. We found that this increase, along with enhanced crossbridge cycling and recruitment of myosin into the crossbridge cycling pool, contributed to increases in steady state force at the filament level. Enhanced recruitment of myosin was shown to dominate behavior at all scales, suggesting that this is the primary mechanism by which dATP improves contractility. Accounting for the faster Ca^{2+} transient decay observed with dATP along with these mechanisms allowed us to fully explain changes in cellular contraction and relaxation, as well as ventricular mechanics. LV function was shown to improve in a dose-dependent manner in simulations of the failing heart, with 1% dATP nearly restoring EF to normal levels, in agreement with experimental results. dATP also improved energetic efficiency without further impairing metabolic state in heart failure. Notably, dATP had a more pronounced impact on ventricular function and energetic efficiency in the failing heart. The multiscale modeling framework developed in this study not only provides a powerful tool for linking molecular effects to changes in ventricular function, but also allowed us to parse the relative effects of several mechanisms of dATP at various scales of function, which would be difficult to accomplish experimentally.

We chose to utilize two different sarcomere models in this study: a spatially explicit model [123] for filament scale force-pCa simulations in Chapter 1, and an implicit model [109] for myocyte shortening and ventricular scale pressure-volume loop simulations in Chapter 2. We chose to utilize the spatially explicit model to assess how small fractions of dATP interact with nearest-neighbor cooperativity to produce disproportionate amounts of steady state force, because this model contains a sophisticated representation of cooperative mechanisms. However, this model is computationally expensive and does not allow for simulation of myocyte shortening,

Ca^{2+} dynamics, or energetics, so we chose to utilize the implicit modeling framework developed by Lopez *et al.* [109] for larger scale simulations. Due to differences in each of these models, the parameter values adjusted in each model differed slightly, mainly due to the addition of a weakly-bound state in the implicit model. dATP may also increase the transition between the weakly- and strongly-bound states, but additional studies are needed to fully address the mechanisms by which dATP increases the rate of crossbridge cycling. Further, it was necessary to increase $k_{recruit}$ by a greater extent in the spatially explicit model than in the implicit model to achieve the same effect. This may be explained by the fact that overall forces are lower by several orders of magnitude in the spatially explicit model, which represents a single sarcomere, than in the implicit model, which represents a whole cell. Regardless, our simulation results reveal that recruitment of myosin into the pool available for crossbridge cycling is the primary mechanism by which dATP increases contractile force.

Additional work is needed to fully explore the effects of dATP on Ca^{2+} dynamics. The relative changes in DT50 and DT90 of the Ca^{2+} transient with dATP measured in isolated cardiomyocytes (*in vitro*) at 1 Hz were utilized to scale the Ca^{2+} transient for the ventricular simulations (at 7 Hz). This does not take into account possible frequency effects on changes to the Ca^{2+} transient with dATP, or the effects of the experimental preparation. Further, we assumed that the changes in the Ca^{2+} transient were independent of dATP fraction, but the validity of this assumption warrants further investigation. Additional work is also needed to determine the underlying mechanism by which dATP increases the rate of Ca^{2+} transient decay. This is investigated further in Chapter 3, where we show that dATP acts on SERCA to increase the rate by which it pumps Ca^{2+} back into the SR, but additional studies are needed to determine whether dATP also acts on other ATPase pumps or mechanisms that regulate Ca^{2+} handling in the cell. Extension of our model to include a model of the SERCA pump and other proteins involved in Ca^{2+} handling would allow us to further investigate the effects of dATP on the Ca^{2+} transient. Finally, it is possible that there are additional mechanisms at play at the ventricular level such as regulation by the autonomic nervous system that could be taken into account in

future studies [54].

We found that the combined mechanisms of increased myosin recruitment and faster Ca^{2+} dynamics led to both improvements in contractile function and energetic efficiency in the failing heart, while efficiency was decreased in healthy heart simulations. This is consistent with previous findings for OM, which has some similar mechanisms to dATP [201]. This is likely because in both healthy and failing conditions, dATP improves both work rate and ATPase rate; however, work rate is increased to a greater extent in the failing model, leading to an overall increase in efficiency, while ATPase rate is increased to a greater extent in the healthy model, leading to an overall decrease in efficiency. Interestingly, the large improvements in both ventricular function and energetic efficiency in heart failure were mainly due to increased myosin recruitment into the crossbridge cycling pool. This could plausibly be due to a larger initial pool of myosin heads in inactive states in failure, but additional data is needed to further explore this. We also observed that increased myosin recruitment led to increases in MVO_2 in the healthy heart, but not in the failing heart, which may also contribute to improvements in energetics in failure. Further, we observed that faster Ca^{2+} transient decay led to reduced EF in healthy heart simulations but increased EF in failing heart simulations, which could be due to the fact that relaxation is likely impaired in failure. Further, we found that dATP increased the CrP/ATP ratio in failure despite not changing it in healthy heart simulations with 1% dATP. Experimental data from healthy transgenic mouse hearts showed a decreased CrP/ATP ratio with elevated dATP [147], but the CrP/ATP ratio has not been measured in HFrEF with dATP, so additional data is needed. Additionally, dATP treatment may lead to functional and/or morphological changes in mitochondria, so further experimental data and expansion of our model to include these mechanisms would allow for a more complete assessment of the effects of dATP on energetics.

Our modeling approach utilized a simplified model of the heart which approximates the left and right ventricles as hemispheres. While this approach allowed us to gain valuable insight into the ways in which dATP affects ventricular performance at a relatively low computational cost, in the future this framework could be extended to capture more realistic geometries. A

finite element model of the heart would allow us to incorporate patient-specific geometries and to assess regional changes in mechanics, as well as potential growth and remodeling. This model provides a powerful tool for assessing small molecule therapeutics such as dATP by integrating existing experimental data at multiple levels spanning the molecular to whole organ levels to generate new model predictions which can be tested through further experimentation and modeling.

2.6 Acknowledgements

Chapter 2, in part, is a reprint of material as it appears in A. E. Teitgen, M. T. Hock, K. J. McCabe, M. C. Childers, G. A. Huber, B. Marzban, D. A. Beard, J. A. McCammon, M. Regnier, and A. D. McCulloch. Multiscale modeling shows how 2'-deoxy-ATP rescues ventricular function in heart failure. *In review at PNAS*, 2024. The dissertation author is the primary investigator and first author of this publication.

Chapter 3

Multiscale Computational Modeling of the Effects of 2'-deoxy-ATP on Cardiac Muscle Calcium Handling

3.1 Abstract

Ca^{2+} transients in cardiomyocytes with elevated levels of dATP show faster Ca^{2+} decay compared with cardiomyocytes with basal levels of dATP, but the mechanisms behind this are unknown. Here, we design and utilize a multiscale computational modeling framework to test the hypothesis that dATP acts on the sarcoendoplasmic reticulum Ca^{2+}-ATPase (SERCA) pump to accelerate Ca^{2+} re-uptake into the SR during cardiac relaxation. Gaussian accelerated molecular dynamics simulations of human cardiac SERCA2A in the E1 *apo*, ATP-bound and dATP-bound states showed that dATP forms more stable contacts in the nucleotide binding pocket of SERCA and leads to increased closure of cytosolic domains. These structural changes ultimately lead to changes in Ca^{2+} binding, which we assessed using BD simulations. We found that dATP increases Ca^{2+} association rate constants to SERCA and that dATP binds to *apo* SERCA more rapidly than ATP. Using a compartmental ordinary differential equation model of human cardiomyocyte excitation-contraction coupling, we found that these increased association rate constants contributed to the accelerated rates of Ca^{2+} transient decay observed experimentally. This study provides clear mechanistic evidence of enhancements in cardiac

SERCA2A pump function due to interactions with dATP.

3.2 Introduction

The sarcoendoplasmic reticulum Ca^{2+}-ATPase (SERCA) 2A is a P-Type ATPase [153, 18] which is critical for sequestration of Ca^{2+} into the SR during cardiac relaxation and is the dominant SERCA isoform in cardiac muscle [80]. SERCA is a transmembrane protein embedded in the SR lipid membrane which consists of 3 cytosolic domains (Nucleotide binding domain - "N", Phosphorylation domain - "P", Actuator domain - "A") as well as 10 transmembrane (M) helices, M1 through M10 (Figure 3.1A) [194, 206]. The nucleotide binding region is located within the N domain. Ca^{2+} binding occurs in the transmembrane region between helices M4, M5, M6, and M8, at binding locations known as Site I and Site II (Figure 3.1C) [32, 206]. Generally, SERCA transitions between two major states as it pumps Ca^{2+} into the SR in an ATP-driven manner: E1 and E2. In the first state, E1, the the Ca^{2+} binding sites face the cytosolic side of the membrane. Binding of ATP and two Ca^{2+} ions, followed by ATP dephosphorylation and hydrolysis, reconform the protein so that Ca^{2+} can be released into the SR lumen [151, 206]. The SR-facing conformation is known as E2. Release of ADP, phosphate, and Ca^{2+} ions into the SR lumen allow the protein to move back into the E1 state [19, 206]. A simplified ordinary differential equation model of SERCA function developed by Tran *et al.* [210] describes several rate-limiting steps within the cycle: (1) Mg^{2+}ATP binding, (2) binding of the first Ca^{2+} ion to site I (site II binding is then considered to occur instantaneously), (3) ADP release, coupled with the E1-E2 transition, (4) Release of Ca^{2+} ions into the SR lumen, and (5) Pi release, coupled with E2-E1 transition. Here we focus on how the first two of these rate-limiting steps may be affected by a molecular modification to ATP.

Upregulation of dATP to $\sim 1\%$ of the overall ATP pool led to increased cell shortening, but also had a marked and beneficial effect on the Ca^{2+} transient leading to improved lisutropy [97]. These results showed decreased time to 50% and 90% Ca^{2+} transient decay, suggesting

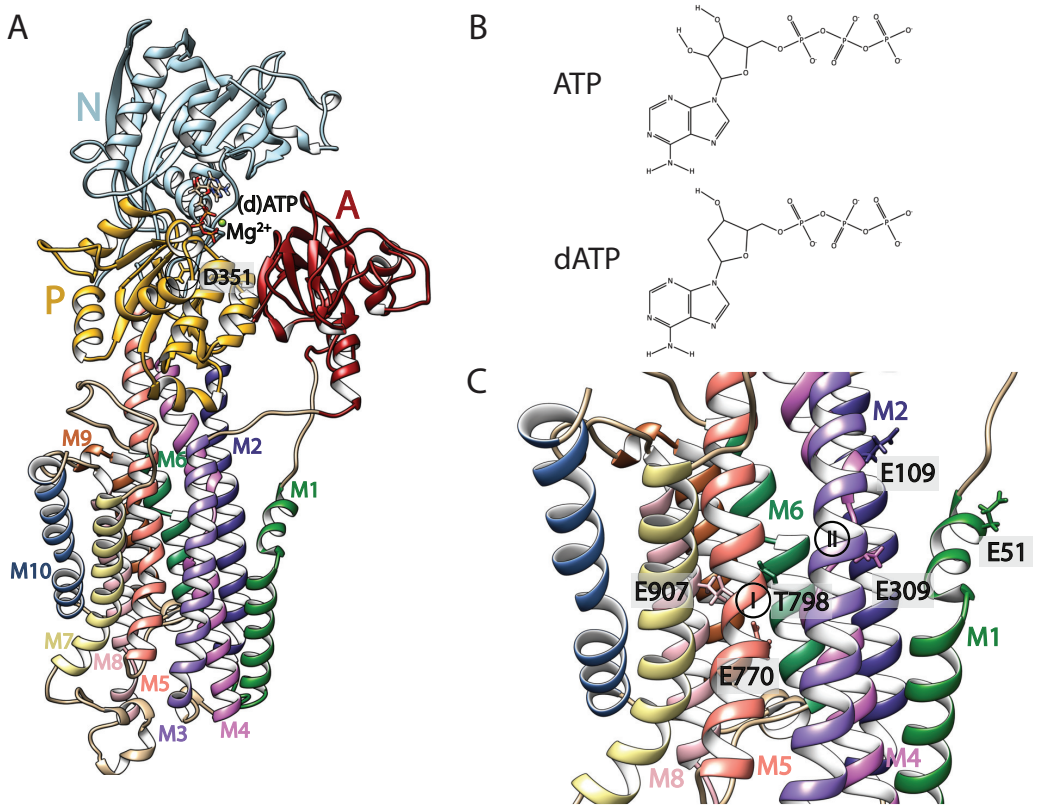

Figure 3.1. (A) Overview of the SERCA structure. A, N, and P cytosolic domains, as well as M1–M10 transmembrane helices are labeled. D351, the nucleotide phosphorylation site, is also labeled. Nucleotide and Mg2+ are shown in the binding site on the N domain. (B) ATP and dATP chemical structures. Note missing hydroxyl group on the ribose ring for dATP. (C) Ca^{2+} binding site I and site II, and key residues used for assessing Ca^{2+} binding path dynamics including E907 on M8, E770 on M5, and T798 on M6 (site I), E309 on M4 (site II), and E109 (M2) and E51 (M1) which comprise part of the Ca^{2+} entry path.

that the rate of intracellular Ca^{2+} reduction is enhanced during dATP treatment. This may confer additional therapeutic benefit in heart failure which is commonly characterized by decreased function and expression of SERCA2A in failing cardiac myocytes [158, 164, 235]. SERCA is also under investigation as a therapeutic target [158, 134, 235, 64, 212, 57]. To reveal potential therapeutic mechanisms of dATP on SERCA2A, analysis at multiple scales from atomic resolution MD to whole cell function is required.

We developed a multiscale modeling approach spanning molecular to whole cell scales. GaMD simulations of human cardiac E1 SERCA2A embedded in a lipid bilayer [128, 218, 207, 86] were conducted on three separate systems: *apo*, ATP-bound, and dATP-bound. Analysis of the GaMD trajectories allowed us to locate key sites in the cytosolic and transmembrane domains of SERCA that may be modified by dATP binding. Rigid body BD simulations [70] were then used to measure association rate constants of ATP, dATP, and Ca^{2+} ions to SERCA2A. We found that dATP bound to SERCA2A with greater affinity than ATP, and Ca^{2+} bound with a higher affinity to dATP-bound than ATP-bound SERCA. Finally, in a compartmental ordinary differential equation model of whole cell Ca^{2+} handling [66], the effects of these molecular differences on the Ca^{2+} transient were predicted.

3.3 Methods

3.3.1 Gaussian Accelerated Molecular Dynamics

We began with a crystal structure of human cardiac SERCA2A in the E2 state from the protein data bank (PDB) (PDB ID: 7BT2) [13, 86]. Since no human cardiac SERCA2A structures in the E1 state were available, we constructed a homology model using a SERCA1A crystal structure in the E1 state purified from rabbit fast-twitch skeletal muscle (PDB ID: 3W5A) [207]. Homology modeling was done using SWISS-MODEL [182]. Sequence identity was 83.7%, with 93.1% similarity, determined using Clustal Omega, [188] and the GMQE score for the model was 0.77. Chain A from the 3W5A crystal structure was used for homology modeling.

Ligands K^+, MPD, and PCW were removed from the 7BT2 structure, and Na^+, Mg^{2+}, M1, PTY, and sarcolipin were removed from the 3W5A structure. Nucleotide and Mg^{2+} position within the nucleotide binding pocket were taken directly from the 7BT2 structure. CHARMM-GUI was used to prepare all simulation files [103]. Protonation states were determined using the PDB2PQR PropKa tool, at a pH of 7.0 [42, 193, 152, 41]. Protonated residues were: HSE (683), and HSD (5, 32, 38, 190, 278, 284, 868, 872, 880, 882, 944). A disulfide bond was added between CYS 875 and CYS 887. The protein was embedded in a 12.5 by 12.5 nm lipid bilayer, and the position of SERCA within the bilayer was determined using the Orientations of Proteins in Membranes (OPM) database [108]. The lipid bilayer was composed of POPC (51% upper leaflet, 66% lower leaflet), POPE (43% upper leaflet, 17% lower leaflet), and POPS (6% upper leaflet, 17% lower leaflet), with 308 total lipids in the upper leaflet and 297 total lipids in the lower leaflet, based on experimentally determined membrane composition in the cardiac SR [16]. A rectangular water box of thickness 22.5 nm was added, and period boundary conditions were utilized for simulation. K^+ and Cl^- ions were added using the Monte Carlo placement method at a 150 mM concentration to neutralize the system [10]. AMBER input files were generated using CHARMM-GUI.

To construct the dATP structure, the extra hydroxyl group was removed from the ATP structure, taken directly from the 7BT2 crystal structure, using Chimera [159]. These ATP and dATP structures were then input into CHARMM-GUI, and antechamber was used to generate force field parameter files using the AMBER GAFF2 force field [65, 219]. The AMBER FF19SB [203] force field was used for protein residues, and the Lipid17 and OPC [81] force fields were used for lipid and water molecules, respectively. The SHAKE algorithm was used to constrain the motion of hydrogen-containing bonds [133].

MD and GaMD simulations were performed using Amber20 [26], and all simulations were run on the Triton Shared Computing Cluster through the San Diego Supercomputer Center [2]. A total of 150 ns of conventional MD and 200 ns of GaMD (3 replicates) were performed for *apo*-SERCA, and ATP- and dATP-bound SERCA. Prior to these simulations, minimization

was done over 5000 steps of steepest decent minimization with 10 kcal mol^{-1} $Å^{-2}$ positional restraints on all protein atoms and 2.5 kcal mol^{-1} $Å^{-2}$ positional restraints on all lipid atoms, with NMR restraints. Equilibration was done over 6 steps, for 1.875 ns total. The Langevin temperature equilibration scheme using a collision frequency of 1.0 ps^{-1} was utilized to set the system temperature to 303.15 K using the NVT ensemble over 2 steps (125 ps each). During these heating steps, 10 kcal mol^{-1} $Å^{-2}$ positional restraints were present on all protein atoms for the first step and 5 kcal mol^{-1} $Å^{-2}$ positional restraints were present on all protein atoms for the second step, and 2.5 kcal mol^{-1} $Å^{-2}$ positional restraints with NMR restraints were present on all lipid atoms for both steps. The system was then equilibrated over 4 stages using the semi-isotropic (with constant surface tension) NPT ensemble (constant number of particles, pressure, and temperature), for 125 ps, 500 ps, 500 ps, and 500 ps, respectively, with the system set to 1.0 bar. Positional restraints on all protein atoms were 2.5, 1.0, 0.5, and 0.1 kcal mol^{-1} $Å^{-2}$ for each step, respectively. Positional and restraints on all lipid atoms were 1.0, 0.5, 0.1, and 0 kcal mol^{-1} $Å^{-2}$ for each step, respectively, with NMR restraints.

MD and GaMD simulations were run at 303.15 K using the PMEMD (particle mesh ewald molecular dynamics) method with a 9 Å nonbonded cutoff, and 2 fs timestep. Coordinates were saved every 100 ps for MD and 20 ps for GaMD simulations. In GaMD, a Gaussian distribution is used to provide a boost potential for the system in order to enhance conformational sampling at shorter simulation time scales [128]. A single boost potential was applied to the total potential energy only. The final frame from the 150 ns MD simulations was used as the starting point for the GaMD simulations, and 0.4 ns of conventional MD prep, 2.4 ns of conventional MD (to calculate potential statistics), 0.4 ns of GaMD pre-equilibration (with boost potential applied), and 10.4 ns of GaMD equilibration (with boost potential applied and boost parameters updated) were run before all GaMD production simulations. The three GaMD replicates were averaged for analysis. Chimera, VMD, and PyMol were used for trajectory analysis and visualization [159, 71, 1]. Analysis was performed using the AMBER cpptraj [176] and the MDTraj python libraries [124]. Hydrogen bonding analysis used a 3 Å and 135° cutoff. Energetic reweighting of

trajectory data was performed after all simulations using a Gaussian approximation of cumulant expansion to the second order. This step is necessary because a boost potential was applied at each time step in order to flatten the energy landscape during the simulation and increase conformational sampling [128]. Briefly, the potential for mean force (PMF) as a function of reaction coordinate A_j is calculated as:

$$PMF(A_j) = -\frac{1}{\beta} \ln p(A_j) \tag{3.1}$$

Where $\beta = k_B T$ and $p(A_j)$ is the canonical ensemble distribution. Because boost potentials followed a Gaussian distribution, $p(A_j)$ must be calculated from the ensemble distribution of the boosted data set as:

$$p(A_j) = p^*(A_j) \frac{\langle e^{\beta \Delta V(r)} \rangle_j}{\sum_{j=1}^{M} \langle e^{\beta \Delta V(r)} \rangle_j} \ln p(A_j), J = 1, ..., M \tag{3.2}$$

Where $\Delta V(r)$ is the boost potential for each frame, M is the number of bins, and $\langle e^{\beta \Delta V(r)} \rangle_j$ is the ensemble averaged Boltzmann factor for frames in bin j. $\langle e^{\beta \Delta V(r)} \rangle$ is approximated using second order cumulant expansion and is calculated as:

$$\langle e^{\beta \Delta V(r)} \rangle = exp\{ \sum_{k=1}^{\infty} \frac{\beta^k}{k!} \sigma_{\Delta V}^2 \} \tag{3.3}$$

Re-weighting of the GaMD simulations was done using scripts and protocols developed by Miao *et al.* [129].

3.3.2 Brownian Dynamics

BD simulations with Browndye 2 [70] were used to probe SERCA binding kinetics. Browndye treats molecules as rigid cores and uses an adaptive time step to efficiently simulate binding kinetics. We first carried out BD simulations of ATP and dATP binding to the *apo* SERCA structures derived from our GaMD simulations and compared their respective association rate constants. In order to better capture the conformational dynamics and variability of SERCA, 30 SERCA structures were used independently in 30 separate simulations for ATP and dATP. The 30 conformations were obtained through hierarchical clustering of the *apo* GaMD SERCA simulations, using C_α RMS as the cutoff metric. The lipid bilayer was removed for nucleotide binding simulations to reduce simulation compute cost, given that the bilayer should not substantially affect the relative rates of binding of ATP and dATP. Browndye uses "reaction pairs" as a reaction coordinate to measure progress of binding events. These pairs were defined based on the starting homology model with ATP or dATP present. Pairs were defined by contacts between (d)ATP and residues PHE 487 and ARG 559 with a distance less than 3.5 Å. The encounter complex description in Browndye, which specifies the distance between pairs necessary for a reaction to be considered complete, was left unspecified, allowing for a range of binding probabilities to be observed as a function of reaction distance. For each of the 30 representative structures, BD simulations were carried out to measure the association of ATP, and separately with dATP, with 50,000 individual trajectories simulated per conformation. Overall, 1.5 million total ATP trajectories were simulated as well as 1.5 million dATP trajectories. The same AMBER force field used for the GaMD simulations was used to parameterize the protein and nucleotide charges and radii for BD simulations. Binding rate constant curves of the resulting simulations were then averaged based on the cluster weight of each observed representative structure.

We again employed BD simulations to investigate changes in Ca^{2+} binding to site I and II in SERCA when ATP or dATP is bound. The starting SERCA structures were clustered from the GaMD ATP and dATP simulations. Thirty representative structures were extracted from

each nucleotide condition, with the membrane intact. The same hierarchical clustering approach based on the C_α RMS was again applied to generate representative structures. The membrane was included to ensure that Ca^{2+} enters the SERCA protein through a realistic entry point, likely *via* the M1/M2/M4 path, and not through the transmembrane region buried in the lipid bilayer [206]. Reaction pairs for Ca^{2+} to site I were defined based on atoms forming hydrogen bonds in a previously solved crystal structure [209]. A second set of reaction pairs was also established from the same crystal structure for site II. For site I, the 30 structures from the ATP conditions were used to run 50,000 BD trajectories, leading to 1.5 million trajectories. Similarly, the 30 structures from the dATP GaMD simulations were used to run an additional 50,000 BD trajectories per conformation, again leading to 1.5 million trajectories simulated. The binding rate constant curves were averaged based on the frequency of the cluster throughout the GaMD simulations. The same procedure was repeated using the same structures to investigate binding to site II, with the reaction pairs adjusted accordingly for an additional 1.5 million trajectories per nucleotide condition. In total, between the two Ca^{2+} sites and two nucleotides bound, 6 million Ca^{2+} binding BD trajectories were simulated.

All BD simulations for both the nucleotide and Ca^{2+} association simulations used 150 mM ionic strength, and a desolvation parameter of 0.025 based on sensitivity analysis to allow for realistic binding distance criteria. Each BD trajectory had a maximum of 1000000 steps. The dielectric coefficient of the solvent was set to 78, while the solute dielectric coefficient was set to 4.

3.3.3 Calcium Transient Modeling

To assess how changes in nucleotide and Ca^{2+} association rate constants to SERCA impact the myocyte Ca^{2+} transient as a whole, we utilized a whole cell ECC model developed by Himeno *et al.* [66]. This model was chosen because it explicitly includes a three-state model of SERCA [210] which has parameters for ATP binding, Ca^{2+} binding, and E1-E2 transition. In this model, state P_1 is E1 SERCA, which undergoes a reversible reaction dictated by rates K_1^+

and K_1^- to state P_{2-5} (E1 with ATP and 2 Ca^{2+} ions bound). Ca^{2+} binding is considered to be fully cooperative, i.e. binding of the second Ca^{2+} ion is instantaneous after the first Ca^{2+} binding event. Reaction rates K_2^+ and K_2^- encompass MgADP dissociation as well as the E1-E2 transition, leading the model to state P_{6-10}. Finally, reversible reaction rates K_3^+ and K_3^- return the pump to state P_1 [210]. dATP experimental data were digitized from Korte *et al.* Figure 1B (GFP and R1R2, respectively) [97]. Fura ratio units were converted to Ca^{2+} concentration by setting the maximum fluorescence value to 0.45 μM, and the minimum value to 0.05 μM, since these are approximately the maximum and minimum Ca^{2+} values typically seen in the ECC model [66]. The ECC model was optimized to match the ATP experimental Ca^{2+} transient by varying Amp_{SERCA}, Amp_{NCX}, Amp_{NaK}, and f_n, the same parameters which were tuned by Himeno *et al.* in parameterizing their original model [66] (Table 3.1). Optimization was conducted using Particle Swarm Optimization in MATLAB [92]. The timescale of the applied current in the ECC model was adjusted to reflect differences between human and rat and to more closely fit control (ATP) Ca^{2+} transients.

3.4 Results

3.4.1 dATP is More Stable in the Nucleotide Binding Pocket, Facilitating E1-ATP to E1-ADP Transition *via* Enhanced Phosphorylation and Movement of Cytosolic Domains

We first assessed differential interactions of ATP and dATP in the nucleotide binding pocket in the N domain. Computing the overall number of contacts between the nucleotide and residues identified to come within 3 Å for at least one frame of any of the simulations, we found that dATP had a greater number of contacts overall (Figure 3.2A). The average number of contacts was 8.7 for ATP and 10.5 for dATP. Further, we found that dATP had a lower RMSD overall (averaged across all three GaMD simulations) than ATP (Figure 3.2B). This suggests that dATP is interacting more closely with a greater number of residues in the N domain binding pocket, and that it binds more stably, leading to less movement within the binding pocket.

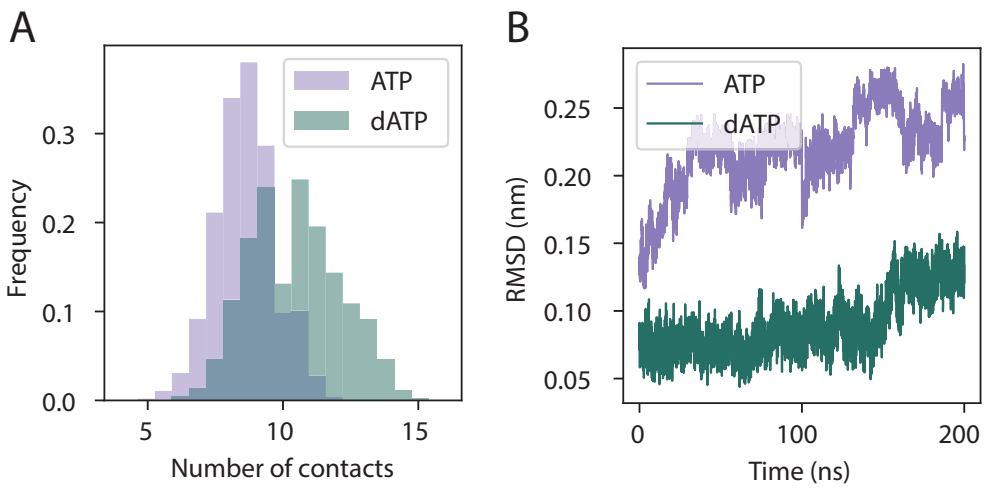

Figure 3.2. dATP is more stable in the nucleotide binding pocket. (A) The overall number of contacts in the binding pocket (averaged across three replicates) was greater for dATP than for ATP. Only residues identified to come within 3Å for at least one frame of the simulation were included. Data are displayed as histograms showing the frequency distribution across the GaMD simulations. (B) The RMSD for dATP (averaged across 3 replicates) was lower than for ATP.

We next assessed specific residue interactions with ATP and dATP in the nucleotide binding pocket. The distances across three GaMD replicates between the nucleotide and several residues of interest are shown in Figure 3.3A. Distances to known nucleotide interaction residues PHE 487, ARG 559, and LYS 514 [206, 208, 68, 33] were unchanged (the average distances were 0.39 nm, 0.30 nm, and 0.47 nm for ATP and 0.39 nm, 0.26 nm, and 0.45 nm for dATP, respectively). This suggests that interactions with these residues do not explain differences in nucleotide association. However, we found that ATP came in closer contact with several residues toward the top of the nucleotide binding pocket than dATP, including THR 441, LYS 492, ARG 677, and ARG 489 (average distances were 0.50 nm, 0.33 nm, 0.36 nm, and 0.43 nm for ATP and 0.56 nm, 0.39 nm, 0.53 nm, and 0.49 nm for dATP, respectively) (Figure 3.3B). The phosphate tail of dATP was shown to come in closer contact with several residues toward the bottom of the nucleotide binding pocket than ATP, including LYS 352, THR 353, THR 624, and ASP 626 (average distances were 0.83 nm, 0.95 nm, 0.91 nm, and 0.56 nm for ATP and 0.45 nm, 0.47 nm, 0.41 nm, and 0.42 nm for dATP, respectively (Figure 3.3C).

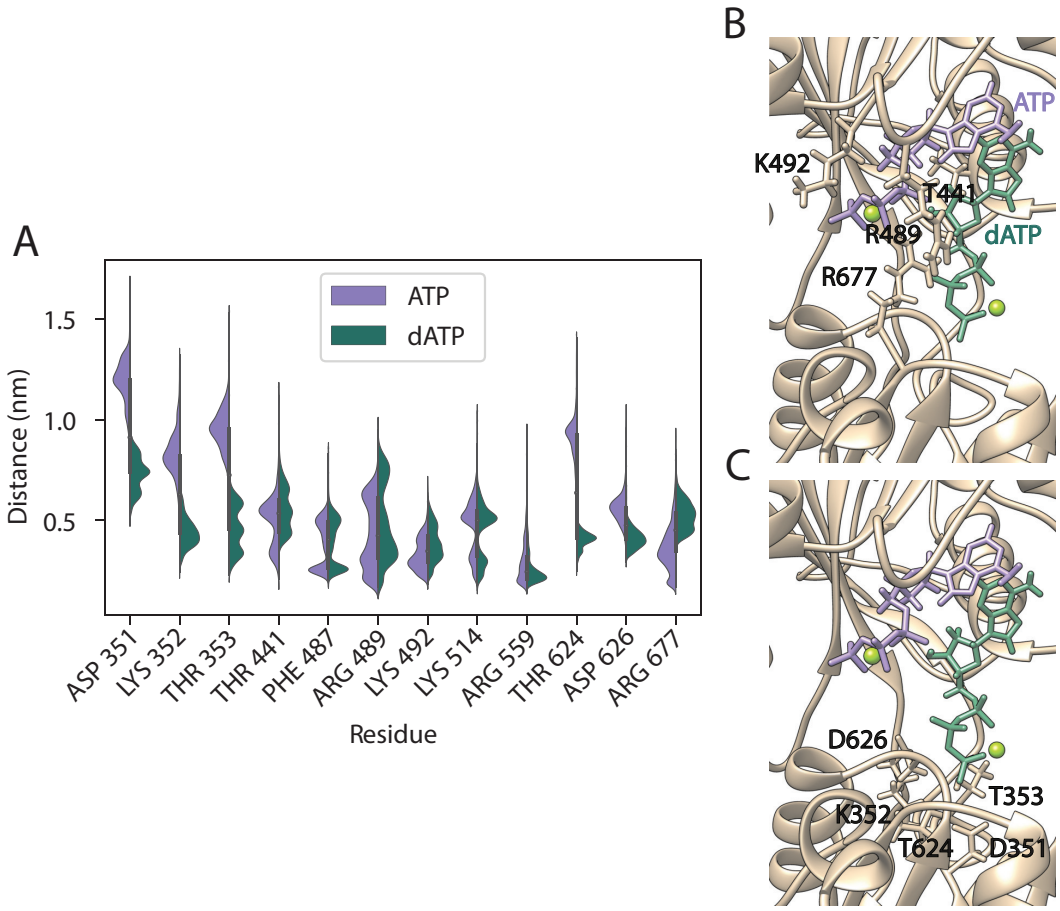

Figure 3.3. dATP occupies a more vertically aligned conformation in the binding pocket than ATP. (A) Distance between nucleotide and residues of interest for ATP and dATP (averaged across three replicates). For each residue of interest, distance distributions (between the residue and nucleotide) are shown as violin plots, where the white dot in the center represents the median, and the thick gray bar represents the interquartile range. Density curves are shown for ATP on the left side of the plot and dATP on the right side of the plot, where the width of the curve represents the frequency of the data (nucleotide-residue distance) at that point. ATP came in closer contact with residues toward the top of the binding pocket, including THR 441, LYS 492, ARG 677, and ARG 489 [shown in (B)]. dATP was shown to come in closer contact with residues toward the bottom of the binding pocket including LYS 352, THR 353, THR 624, ASP 626, and phosphorylation residue ASP 351 [shown in (C)]. This may be explained by the missing hydroxyl group on dATP leading to weaker interactions with residues at the top of the binding pocket. Distances to nucleotide association residues PHE 487 and ARG 559, as well as LYS 514, were unchanged.

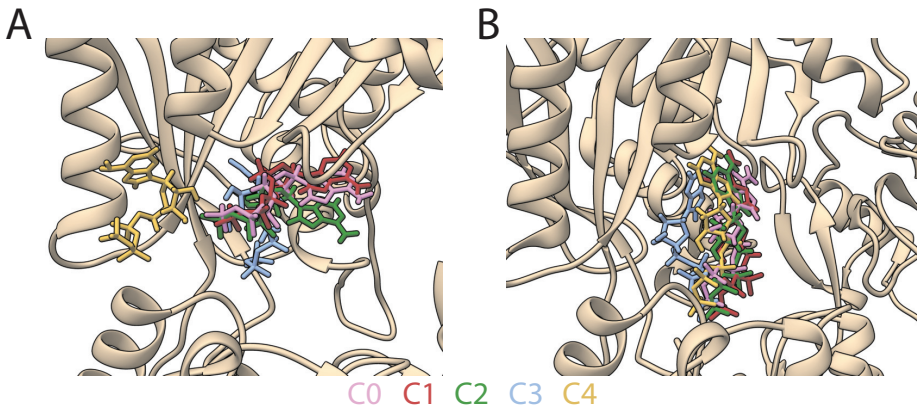

Figure 3.4. Clustering analysis on nucleotide position within the binding pocket, including all three GaMD simulations. Top five clusters are shown for ATP (A) and dATP (B).

We hypothesize that this is due to the additional hydroxyl group on ATP (Figure 3.1B), allowing it to form additional hydrogen bonding interactions with residues at the top of the binding pocket, while dATP does not, causing the phosphate tail to be pulled downwards. The hydrogen bond occupancy of the 2' hydroxyl group on ATP was measured to be 8.21% as a hydrogen bond acceptor, 4.80% as a donor, and overall acting as either a donor or acceptor in 12.4% of the simulation. While this is a minority of the simulation time, the consistent interaction significantly alters its orientation and behavior in the pocket. The preserved 3' hydroxyl shows similar levels of hydrogen bonding occupancy between ATP and dATP, at 30.4% and 34.8% occupancy respectively as either a donor or acceptor. Interestingly, in dATP, the 3' hydroxyl almost never bonds as a donor, at only 0.0312% of frame compared to 4.92% in ATP. These results are further supported by clustering analysis, which confirmed that ATP is most commonly located more horizontally across the top portion of the binding pocket across all 3 replicates, while dATP shows a more vertically aligned conformation in which the phosphate tail is drawn downwards toward the P domain (Figure 3.4). This serves to position dATP such that the gamma phosphate is located substantially closer to the phosphorylation residue ASP 351 (average distance was 1.2 nm for ATP and 0.74 nm for dATP) (Figure 3.3A, C) [206]. This may

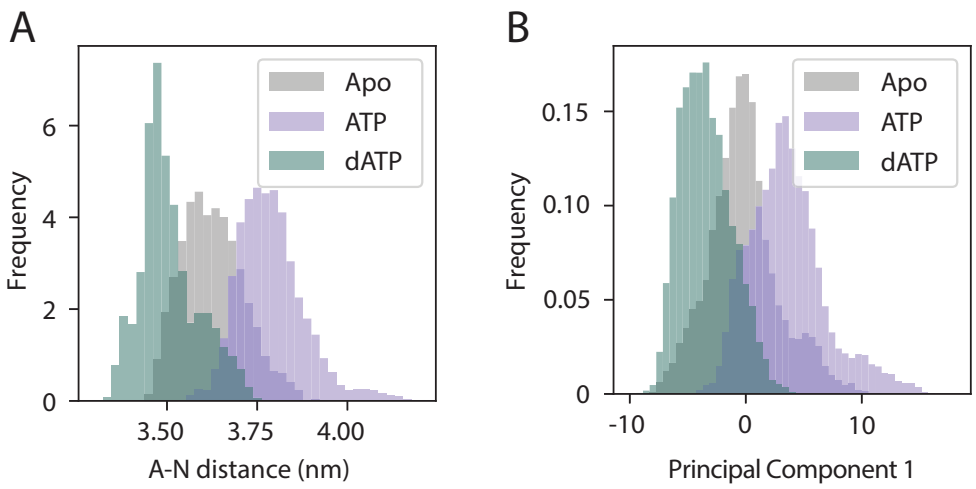

Figure 3.5. dATP enhances transition from E1-ATP to E1-ADP *via* A-N domain closure. Data are displayed as histograms showing the frequency distribution across the GaMD simulations. (A) A-N domain distance (averaged across three replicates), measured from the center of mass for each domain, was lower for dATP than ATP. (B) First principal component from PCA analysis of C_α movement performed on GaMD trajectories, which corresponds to A-N domain movement.

allow for faster phosphorylation by dATP compared with ATP.

Finally, we assessed the differential effects of ATP and dATP on the movement of cytosolic domains of SERCA2A. Closure of the A and N domains (Figure 3.1A) in particular is important for the E1-ATP to E1-ADP transition [206, 18, 136]. We found that the average difference between the center of mass of the A and N domains was smaller for dATP than for ATP (average distance was 3.8 nm for ATP and 3.5 nm for dATP), suggesting that dATP enhances closure of these domains (Figure 3.5A). Further, the standard deviation in A-N domain distances was smaller for dATP than ATP (0.09 nm for ATP vs 0.08 nm for dATP), suggesting that dATP may also stabilize these domains in a more closed conformation. This was also shown to correspond to the first principal component from a PCA analysis conduced on SERCA structures from the GaMD simulations (Figure 3.5B), suggesting that this is the major motion captured by our simulations. Further, reweighting analysis confirmed that these effects were not due to bias in the GaMD simulations since the decrease in A-N distance with dATP, represented by a minimum in the Potential of Mean Force (PMF), was still present even after recovering the

original energy landscape (without the GaMD boost potential) *via* reweighting. Interestingly, ATP increased A-N domain distances with respect to the *apo* structure, while dATP decreased A-N domain distances with respect to the *apo* structure. This may be due to the fact that our GaMD simulations do not have Ca^{2+} present; in the absence of Ca^{2+}, the nucleotide can bind to the N domain and can lead to opening of the cytosolic domains, but cannot lead to subsequent complete closure of these domains or phosphorylation [206, 86]. The effects of dATP on SERCA appear to be pronounced enough to lead to greater closure of the A and N domains. We expect that if Ca^{2+} was present in the GaMD simulations, ATP A-N distances would be smaller than the *apo* case, and dATP A-N distances would be decreased even further.

3.4.2 dATP Binding to SERCA Leads to Opening of Calcium Binding Path

Next, we assessed whether dATP binding affects Ca^{2+} association in the transmembrane region. The Ca^{2+} binding sites have been shown to be allosterically linked to the nucleotide binding site *via* transmembrane helix M5 [206]. Ca^{2+} binds first to site I (passing through site II, which is gated by GLU 309) [18, 206, 69, 79]. This is believed to occur through a cooperative mechanism, where binding of Ca^{2+} to site I increases Ca^{2+} binding affinity for site II [78, 69, 234]. We computed distances between THR 798 (M6), GLU 770 (M5), and GLU 907 (M8), since these residues make up Ca^{2+} binding site I [206] (Figure 3.1C). We found that the average distances between M5 and M6 were increased (average distances were 0.55 nm for ATP and 0.66 for dATP) (Figure 3.6A). Average distances between M5 and M8 were also increased (average distances were 0.45 nm for ATP and 0.52 nm for dATP) (Figure 3.6B). Average distances between M6 and M8, on the other hand, were decreased (average distances were 0.26 nm for ATP and 0.25 nm for dATP) (Figure 3.6C). This suggests that the net effect of dATP is to cause opening of Ca^{2+} binding site I, since M5-M6 and M5-M8 distances were increased by a greater magnitude than M6-M8 distances were decreased with dATP. Similar to the effects of dATP on A-N domain distances, here we observed again that ATP and dATP had

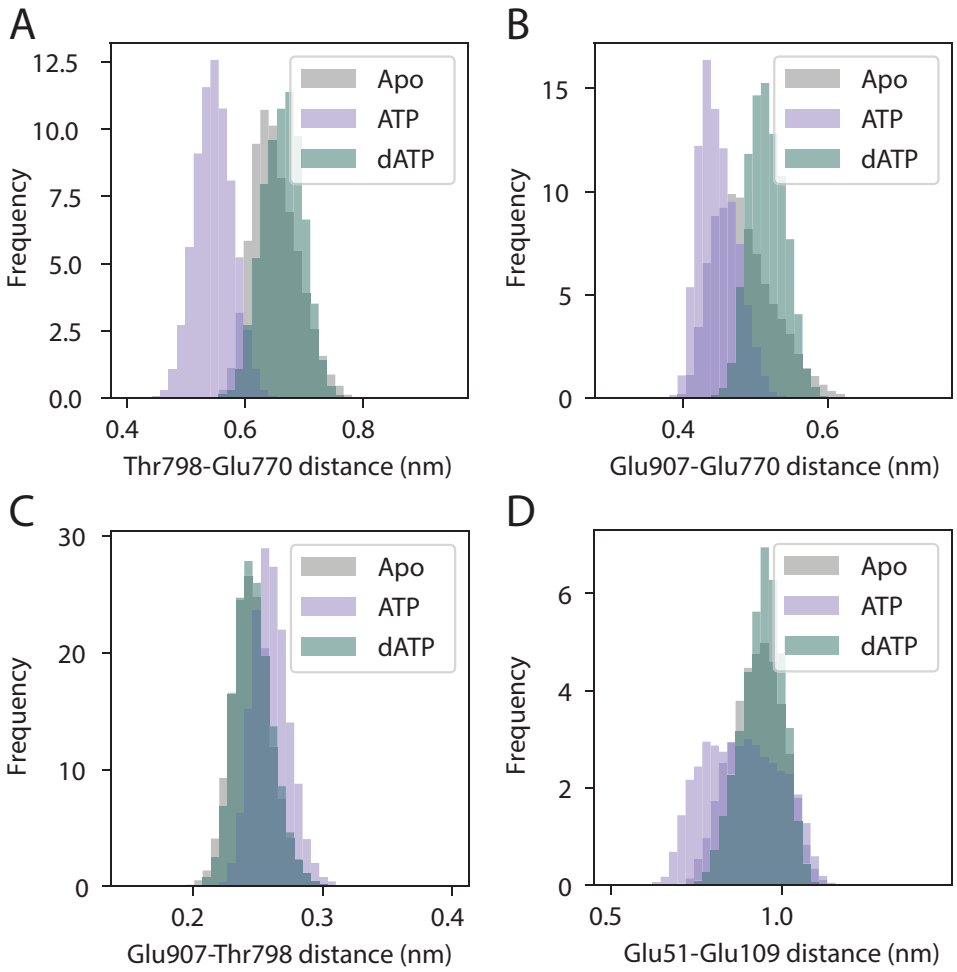

Figure 3.6. dATP binding leads to rearrangement of Ca^{2+} binding path. Distances for key residues on M5 (GLU 770), M6 (THR 798), and M8 (GLU 907) that make up Ca^{2+} binding site I, as well as Ca^{2+} sensing residues on M1 (GLU 51) and M2 (GLU 109) that make up the Ca^{2+} entry path are shown. Distances were averaged across 3 replicates. Data are displayed as histograms showing the frequency distribution across the GaMD simulations. Distances between M5 and M6 (A) and M5 and M8 (B) were increased, while distances between M6 and M8 (C) were decreased with dATP. Distances between M1 and M2 were increased with dATP (D). This suggests that dATP may facilitate Ca^{2+} binding by opening the Ca^{2+} entry path to site I.

opposing effects on transmembrane helix distances with respect to the *apo* structure. This may again be due to the fact that our GaMD simulations were carried out in the absence of Ca^{2+}.

Further, we assessed the effects of dATP on Ca^{2+} entry. Ca^{2+} is proposed to enter SERCA through two different paths [91, 69]. The first is composed of M6, M7, M8, and M9, while the second is composed of M1, M2, and M4. We chose to focus on the second, since there is greater evidence supporting this path [91, 46, 102, 138]. We assessed distances between GLU 51 (M1) and GLU 109 (M2), residues which have been implicated in Ca^{2+} sensing and compose part of the binding path [91] (Figure 3.1C), and found that dATP also led to an increase in this distance (average distance was 0.88 nm for ATP and 0.94 nm for dATP) (Figure 3.6D). We again verified that these results were not due to bias in the GaMD simulations by conducting a reweighting analysis since the changes in residue distances with dATP, represented by a minimum in the Potential of Mean Force (PMF), were still present even after recovering the original energy landscape (without the GaMD boost potential) *via* reweighting. Further, the standard deviation of the distance distribution was smaller for dATP than ATP (0.11 nm for ATP and 0.06 nm for dATP), suggesting that dATP also acts to stabilize these residues in a more open position. Thus, dATP may lead to opening of both the Ca^{2+} binding path and Ca^{2+} binding site I, which could facilitate enhanced Ca^{2+} association.

3.4.3 dATP Increases Rates of Nucleotide and Calcium Association to SERCA Compared with ATP

BD simulations revealed that dATP bound more rapidly to the *apo* structure of SERCA compared with ATP. The weighted average binding curve shows that across a wide range of reaction distances greater than 7 Å, dATP binds more rapidly to the *apo* structure than ATP (Figure 3.7A, B). Selecting a reaction distance of 8.11 Å corresponding to the ATP binding rate constant of 2.59×10^{7} $(\text{M s})^{-1}$ used by Tran *et al.* [210], the corresponding dATP association rate constant was 36% higher (3.52×10^{7} $(\text{M s})^{-1}$). We attribute the lower dATP binding rate constants at low reaction distances to noise, since very few BD simulations reached these small

distances. Less than 0.05% of simulations reached a distance of less than 8 Å and less than 0.03% of reactions reached a distance of less than 5 Å. Although ATP does have an additional polar hydroxyl group that may promote additional electrostatic attraction to the nucleotide binding pocket, we anticipate that removal of this functional group reduces steric hindrance, therefore allowing dATP easier access to the binding site, and that this effect dominates the BD simulations. Furthermore, analysis of a structure by structure comparison of the 30 SERCA conformations used in our simulations revealed that although the nucleotide binding rate constant varied considerably from conformation to conformation, dATP consistently associated more rapidly to SERCA compared with ATP.

Further, BD simulations of dATP-bound SERCA showed differences in Ca^{2+} binding compared to ATP-bound SERCA (Figure 3.7C, D). For reaction distances between 4 and 12 Å, Ca^{2+} bound more rapidly to site I when dATP was bound than ATP. Experimental estimates of Ca^{2+} association rate constants to SERCA vary by up to three orders of magnitude, making determining an absolute binding distance and rate constant difficult, however a previous BD study estimated a Ca^{2+} association rate constant of 3.13×10^9 $(M\ s)^{-1}$ to ATP-bound SERCA [91]. In our simulations, this value corresponded to a reaction distance of 10 Å at which Ca^{2+} binding to site I of dATP-bound SERCA was 23% greater (3.85×10^9 $(M\ s)^{-1}$). Interestingly, dATP reduced the association rate constant of Ca^{2+} to site II. It is believed that Ca^{2+} binds to site I first and initiates a conformational change before a second Ca^{2+} ion can bind to site II. Therefore, the structures extracted from our GaMD simulations may not be an accurate representation of SERCA when the first Ca^{2+} ion is bound. This process is also cooperative, so we anticipate that this sequential step significantly alters the binding kinetics of the second Ca^{2+} ion. As such, we focus our subsequent multiscale analysis on the effects of dATP on Ca^{2+} binding to SERCA at site I.

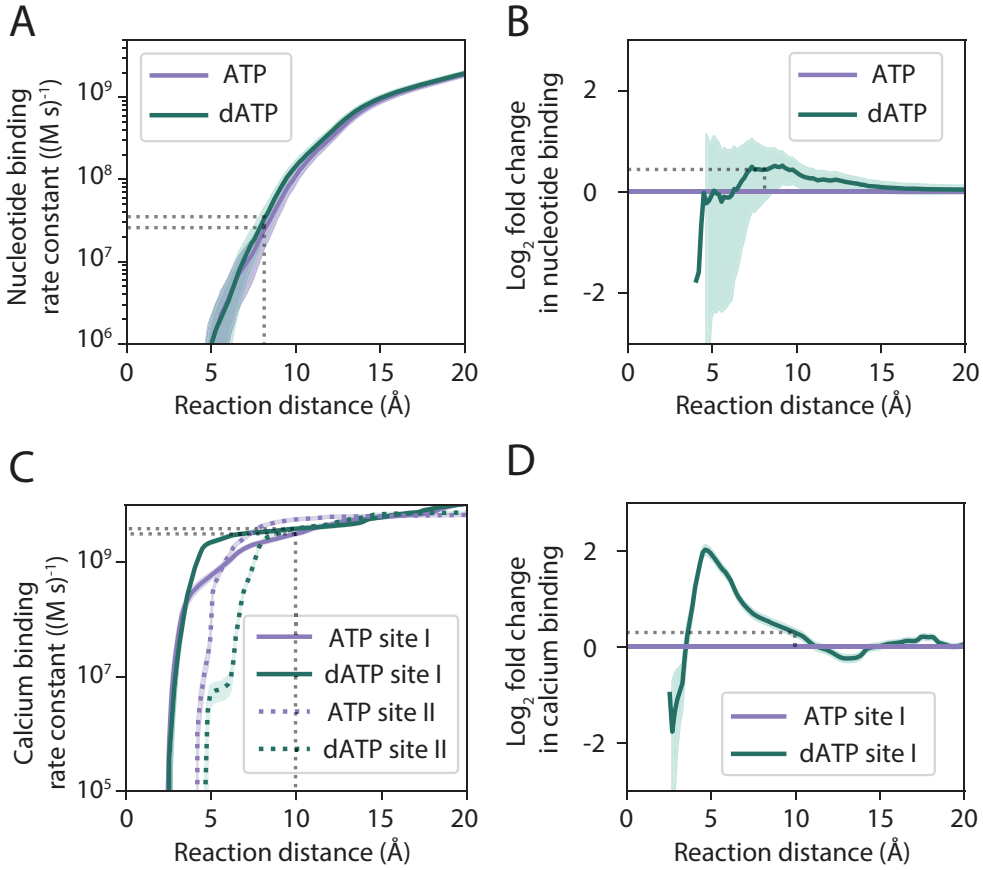

Figure 3.7. (A) BD-predicted binding rate constants as a function of reaction distance. Dotted lines represent reaction distance for association rate constant of ATP to SERCA used in the Tran *et al.* model. [210] (B) Log_2 fold change in nucleotide binding rate constant as a function of reaction distance. Log_2 fold change is used to more easily visualize changes in binding rate constant e.g., a doubling of the binding rate constant is equivalent to a Log_2 fold change of 1, quadrupling is equivalent to a Log_2 fold change of 2, etc. Log fold changes of less than 1 are negative while fold changes greater than 1 are positive (e.g., a halving of the binding rate constant is equivalent to a Log_2 fold change of -1). dATP binds more rapidly to the nucleotide site for reaction distances greater than 7Å below which sampling errors increase owing to the low number of simulations reaching lower reaction distances. (C) BD-predicted association rate constant of Ca^{2+} to sites I and II. dATP increases Ca^{2+} binding to site I compared with ATP. Ca^{2+} binds site II more rapidly when ATP is bound to SERCA than dATP. Dotted lines represent reaction distance that corresponds to the Ca^{2+} association rate constant determined from a previous BD study [91]. (D) Log_2 fold change in the association rate constant of Ca^{2+} to site I when dATP is bound compared with ATP.

Table 3.1. Optimized values for WT (ATP) and dATP-treated Ca^{2+} transients based on the Himeno *et al.* model [66], including parameter changes based on BD results.

Parameter	ATP model	dATP model, 23% decrease $K_{d,Cai}$	dATP model, 41% decrease $K_{d,Cai}$
Amp_{SERCA}	94.47		
Amp_{NCK}	128.52		
Amp_{NaK}	17.77		
f_n	1.37		
K_1^+ (M s)$^{-1}$	2.59×10^7	3.52×10^7	3.52×10^7
$K_{d,Cai}$ (mM)	0.0027	0.0021	0.0016

3.4.4 Enhanced Calcium Binding to dATP-bound SERCA Accelerates Myocyte Calcium Transient Decay

We optimized parameters of the Himeno ECC model to match measured Ca^{2+} transients in the presence of ATP, as described in the methods [66, 92, 97]. In the Tran model of SERCA kinetics [210] (incorporated within the Himeno model), K_1^+ (rate of ATP binding to SERCA) and $K_{d,Cai}$ (dissociation constant for Ca^{2+} binding to SERCA) were then adjusted based on the results of the BD simulations (Table 3.1). Thus, K_1^+ was increased from 2.59×10^7 (M s)$^{-1}$ to 3.52×10^7 (M s)$^{-1}$ based on the BD-predicted change in nucleotide association to SERCA, and $K_{d,Cai}$ was was decreased by 23% from 0.0027 mM to 0.0021 mM based on the BD-predicted change in Ca^{2+} binding to site I. These changes decreased time to 50% decay (DT50) of the Ca^{2+} transient, but only modestly from 308 to 279 ms (Figure 3.8A). However, decreasing $K_{d,Cai}$ by 41%, which is still within the range of the BD simulation results, shortened DT50 by an amount similar to experimental observations in the presence of dATP (Figure 3.8B). In contrast, changes in the nucleotide association rate constant had little effect, suggesting that increasing Ca^{2+} binding to site I may be the primary mechanism by which dATP increases SR Ca^{2+} reuptake (Figure 3.9).

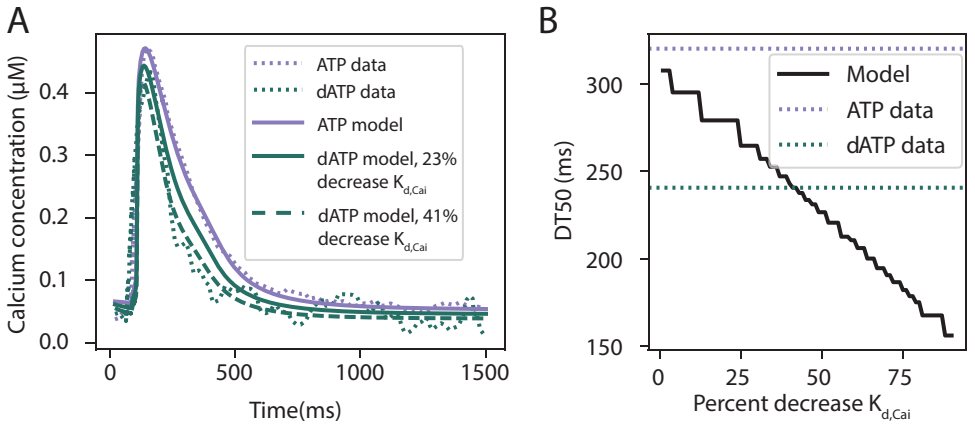

Figure 3.8. dATP accelerates the rate of myocyte Ca^{2+} transient decay *via* enhanced Ca^{2+} association. (A) Effects of changing model parameters K_1^+ and $K_{d,Cai}$ (nucleotide and Ca^{2+} association rate constants, respectively) in the Tran *et al.* model [210] ATP and dATP experimental data digitized from Korte *et al.* [97] are shown as dotted lines. ATP model Ca^{2+} transient (optimized to match ATP experimental data), and dATP predicted model Ca^{2+} transients for 36% increase in K_1^+ combined with 23% and 41% decreases in K_d, Cai are also shown. (B) Percent decrease in K_d, Cai vs DT50. With a 23% decrease in K_d, Cai (based on BD results), we are not able to fully match experimental measurements. However, with a 41% decrease in K_d, Cai, we are able to match experimental measurements of DT50 with dATP. These simulations also include a 36% increase in K_1^+ based on BD results, but changes in K_1^+ were not shown to substantially affect DT50 (Figure 3.9)

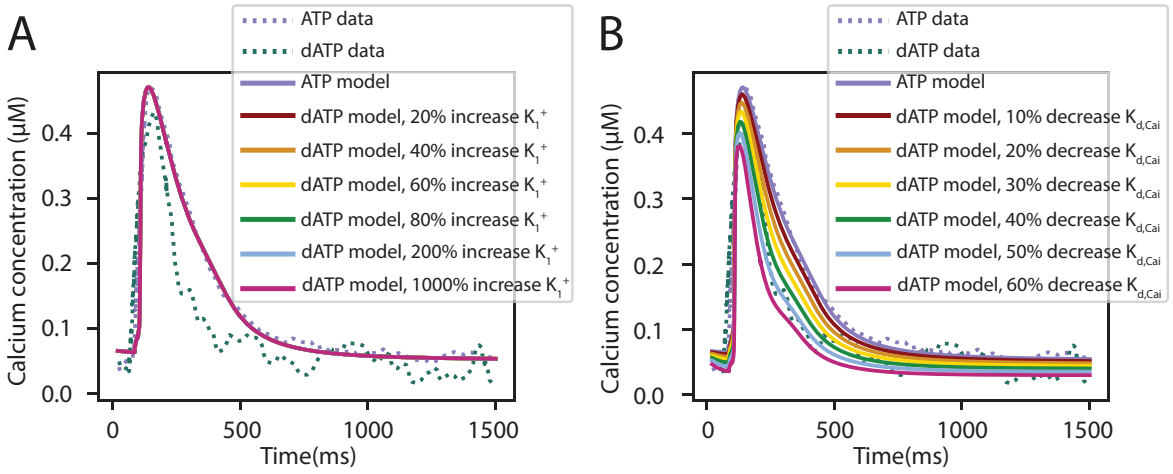

Figure 3.9. Sensitivity analysis on relative effects of adjusting K_1^+ and $K_{d,Cai}$ in the Tran *et al.* ECC model [210]. Changes to K_1^+ did not substantially affect Ca^{2+} dynamics, while decreases to $K_{d,Cai}$ resulted in decreasing time to 50% Ca^{2+} transient decay.

3.5 Discussion and Conclusions

The results of this study provide new evidence for mechanisms by which dATP treatment may contribute to improved SERCA pump function in cardiac myocytes. First, dATP was shown to be more stable in the binding pocket of SERCA and was positioned to facilitate faster phosphorylation. Increased closure of the A-N cytosolic domains indicates faster pump function with dATP treatment. Further, we observed separation of transmembrane helices M5 and M6 and M5 and M8, as well as M1 and M2, which may facilitate faster Ca^{2+} association. dATP demonstrates a 36% higher association rate constant than ATP to the N domain of SERCA. However, inputting the nucleotide and Ca^{2+} association rate constants determined from BD analysis (K_1^+ and $K_{d,Cai}$) into an ECC model did not fully explain experimentally observed differences in the Ca^{2+} transient due to dATP, but further decreasing the Ca^{2+} dissociation constant could.

While this study provides valuable insight into the molecular mechanisms by which dATP affects SERCA function, our GaMD simulations did not capture the phosphorylation event or downstream protein conformational changes after Ca^{2+} binding. Future MD or quantum mechanics simulation studies would aid in better elucidating these effects. Our BD simulations also allowed for the entry of the nucleotides and Ca^{2+} from any orientation from the SERCA pump, not only the cytosolic side, which is a limit of our approach. Moreover, there are also other ATPases that contribute to intracellular Ca^{2+} dynamics such as the PMCA and NCX pumps, which may also be affected by dATP to enhance Ca^{2+} efflux from the cell. SERCA is regulated by phospholamban and several post-translational modifications that could also affect its pump function [235]. It is likely that both SERCA upregulation and these other pumps together could explain the improved relaxation observed experimentally due to dATP treatment. This could be further explored with computational and experimental studies that specifically focus on the effects of the cooperative binding of Ca^{2+} with relation to dATP and ATP. For instance, additional MD simulations of SERCA with one or both Ca^{2+} binding sites occupied

will certainly change the free-energy landscape and thus, yield additional structures and insights. Additionally, since dATP is a candidate therapeutic approach for heart failure with reduced EF, which is characterized by prolonged twitch relaxation and Ca^{2+} transient decay associated with downregulated SERCA function, it would be useful to apply this analysis to a model of ECC in the failing cardiac myocyte.

In this study, we analyzed the effects of nucleotide binding on SERCA pump kinetics and the differential effects of ATP and dATP on Ca^{2+} affinity *via* changes to the transmembrane domain. This study has demonstrated the power of multiscale modeling for investigating the effects of ATP analogs on cardiac cells, as we integrated knowledge from the atomic to the cellular level to uncover potential mechanisms of dATP which scale up to a significantly altered Ca^{2+} transient and cardiac function as a whole.

3.6 Acknowledgements

Chapter 3, in part, is a reprint of material as it appears in M. T. Hock*, A. E. Teitgen*, K. J. McCabe*, S. P. Hirakis, G. A. Huber, M. Regnier, R. E. Amaro, J. A. McCammon, and A. D. McCulloch. Multiscale computational modeling of the effects of 2'-deoxy-ATP on cardiac muscle Ca^{2+} handling. *J. Appl. Phys.* 134(7):074905, 2023. *Equal contribution. The dissertation author was the co-first author of this publication.

Chapter 4

Applications of Multiscale Modeling Framework for In Silico Development of Novel Heart Failure Treatments

4.1 Abstract

Many mutations linked to the development of DCM, which can lead to the progression of HFrEF, lead to reduced Ca^{2+} sensitivity and decreased sarcomere force production. However, it is not always clear how these molecular level mechanisms lead to long-term growth and remodeling, and progression to heart failure. Computational modeling can provide a useful tool not only for better understanding these mechanisms, but for generating predictions about potential treatment options for specific mutations. In this study, we demonstrate how computational modeling can be utilized to predict a novel treatment strategy for a specific mutation linked to DCM, the D230N-Tm mutation. To do this, we utilized the twitch tension-time integral, which has been shown to be an indicator of adverse remodeling, to predict that the L48Q-cTnC mutation reverses the effects of the D230N mutation, leading to increased Ca^{2+} sensitivity and force production similar to WT at the myocyte level. Model development was informed by experimental data, and model predictions were validated using experimental data from double-transgenic (D230N/L48Q) mice, which showed improved cardiac function, demonstrating the utility of combining computational and experimental approaches. These techniques, along with

the framework utilized in the previous three chapters, can be extended to investigate additional mutations linked to cardiomyopathies and the development of HFrEF, as well as additional potential gene therapy treatment options or small molecule therapeutics that can be targeted to treat specific heart failure genotypes and phenotypes.

4.2 Introduction

Cardiomyopathies typically lead to adverse growth and remodeling of the heart. However, the link between molecular and cellular level alterations in mechanical function and long term remodeling is not always clear. There is also a need to develop precision medicine approaches to target specific mutations linked to the development of these cardiomyopathies. In a recent study, Davis *et al.* [36] showed that the area under the twitch curve can be utilized to predict whether the heart will remodel eccentrically (as in DCM) or concentrically (as in HCM) given a particular perturbation. This "Tension index" (TI), calculated as the integral of the twitch-time curve relative to control, strongly correlated with the degree of remodeling measured experimentally. A positive TI was correlated with eccentric remodeling, while a negative TI was correlated with concentric remodeling. The TI encompasses both peak twitch force and the rate of force development and relaxation, and can thus be a useful tool for screening potential therapeutic strategies targeted to specific mutations.

In this study, we showed that the TI can be utilized to predict therapeutic interventions that can prevent deleterious remodeling in DCM, specifically in relation to the D230N-Tm mutation [196, 197]. *In vitro* studies have shown that this mutation decreases Ca^{2+} sensitivity and ATPase turnover rate, leading to a reduction in force production and the TI [99, 114, 62]. *In vivo*, D230N transgenic mice were also shown to develop a DCM phenotype with systolic dysfunction and eccentric hypertrophy [114].

We utilized an implicit sarcomere model to predict that increasing thin filament Ca^{2+} sensitivity increased the TI of D230N hearts to a greater extent than increasing the actomyosin

association rate (which is one mechanism of some inotropic interventions including dATP). This prediction was compared to experimental data from double-transgenic mice expressing the L48Q-cTnC mutation, which increases Ca^{2+} sensitivity [36, 204, 217, 47, 187, 90, 155], in addition to the D230N mutation. These double-transgenic mice had significantly increased TI and contractility and did not progress towards DCM remodeling, illustrating the power of combining computational and experimental approaches to design novel treatment options for genetic cardiomyopathies.

4.3 Methods

4.3.1 Calculation of TIs

Similar to what has been done previously [36], twitch tension-time traces were normalized to the maximum wild type (WT) value. The time integral of the twitch tension curve was calculated using a point-by-point integration method based on cumulative trapezoidal approximations using MATLAB [77]. The TI was then calculated as the difference between the time integral relative to WT (The TI for WT is therefore 0 by definition).

4.3.2 Computational Simulations of Cardiac Twitches

Similar to what has been done previously [36], we simulated cardiomyocyte twitches by modifying the parameters in the Negroni-Lascano model [143] to fit experimental measurements of cardiac twitches. As shown in Figure 4.1, the model consists of 6 states: no Ca^{2+} bound to Tn (TS), Ca^{2+} bound to Tn with no crossbridges ($TSCa_3$), Ca^{2+} bound to Tn with weak crossbridge attachment ($TSCa_3 \sim$), Ca^{2+} bound to Tn with strong (tension-generating) crossbridge attachment ($TSCa_3*$), no Ca^{2+} bound to Tn with strong (tension-generating) crossbridge attachment ($TS*$), and no Ca^{2+} bound with weak crossbridge attachment ($TS \sim$). This model was chosen due to its explicit definition of multiple thin filament states, as well as its use in previous studies using the TI [36]. Original parameter values and initial conditions from the

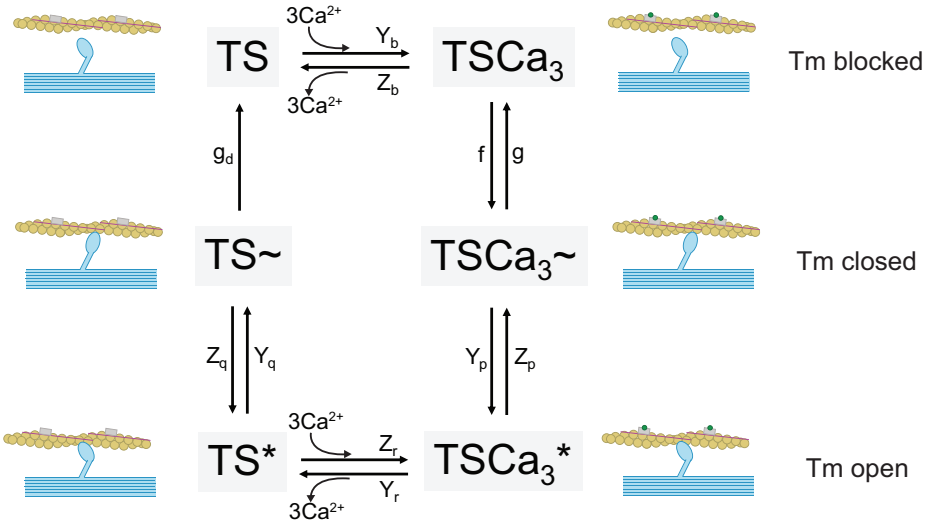

Figure 4.1. Schematic of the Negroni-Lascano model of cardiac tension development during twitch transients, adapted from [143]. For clarity, we have labeled the states in which Tm is occupied (blocked, closed, or open)

Negroni-Lascano model [143] were used to simulate "WT" twitches. To simulate D230N-Tm twitches, we reduced the transition rate from $TSCa_3$ to $TSCa_3 \sim$ (parameter f, see Table 4.1) by 43.5% such that the peak tension was decreased by the same amount compared with WT (∼50%) as observed experimentally. Y_b, Z_b, Y_r, and Z_r, which represent Ca^{2+} association and dissociation from Tn, were varied to assess the effects of Ca^{2+} modulation on sarcomeres with the simulated D230N-Tm mutation. Z_p, and Y_p, the transition rates between $TSCa_3 \sim$ and $TSCa_3*$, and g, the transition rate from $TSCa_3 \sim$ to $TSCa_3$, were varied to assess the effects of cross-bridge modulation on cardiomyocytes with the simulated D230N-Tm mutation. Forward rates (Y_b, Z_r, and Y_p) were progressively increased by factors of 2–10 (with the exception of Y_b, which was increased by a maximum of 9-fold to allow for model convergence), and reverse rates (Z_b, Y_r, Z_p, and g) were simultaneously decreased by factors of 0.9–0.5 to assess a range of Ca^{2+} and crossbridge modulation (Table 4.1). SL was set to 1.8 μm. Model equations were implemented using MATLAB [77] and solved using a forward Euler method for 1000 ms under isometric conditions.

4.4 Results

4.4.1 Increasing Calcium Sensitivity Increases the TI of Cardiomyocytes with D230N-Tm to a Greater Extent Than Increasing the Crossbridge Binding Rate

We utilized a computational modeling approach to assess whether the TI of cardiomyocytes containing the D230N-Tm mutation can be modulated using inotropic intervention and, if so, whether augmented Ca^{2+} sensitivity of thin filament activation or augmented cross-bridge binding has a greater effect on the TI. To do so, we used a model of cardiomyocyte contraction [143], as has been done previously [36], to independently and systematically increase either the Ca^{2+} affinity of cTnC or the rate of strong crossbridge attachment in a sarcomere with the D230N-Tm mutation and calculated the TI for each case. Twitches of cardiomyocytes containing dysfunctional Tm were simulated by reducing the rate of transition of Tm from "blocked" to "closed" [143, 125] (Figure 4.1, Table 4.1) until peak tension was reduced by the same amount observed experimentally in intact trabeculae from transgenic hearts containing D230N-Tm ($\sim$50%) (Figure 4.2A). The resulting TI of simulated D230N cardiomyocytes is –13.4 $\times 10^4$ Tension*ms. Progressively increasing the rate of strong crossbridge binding increased the TI of simulated D230N cardiomyocytes (Figure 4.2B, dotted line) until it eventually asymptoted at a value well below 0 (the point at which the TI equals that of WT). Conversely, progressively increasing the Ca^{2+} affinity of cTnC increased the TI of simulated D230N cardiomyocytes well beyond 0 (Figure 4.2B, dashed line) and did not asymptote for the range of parameters explored here.

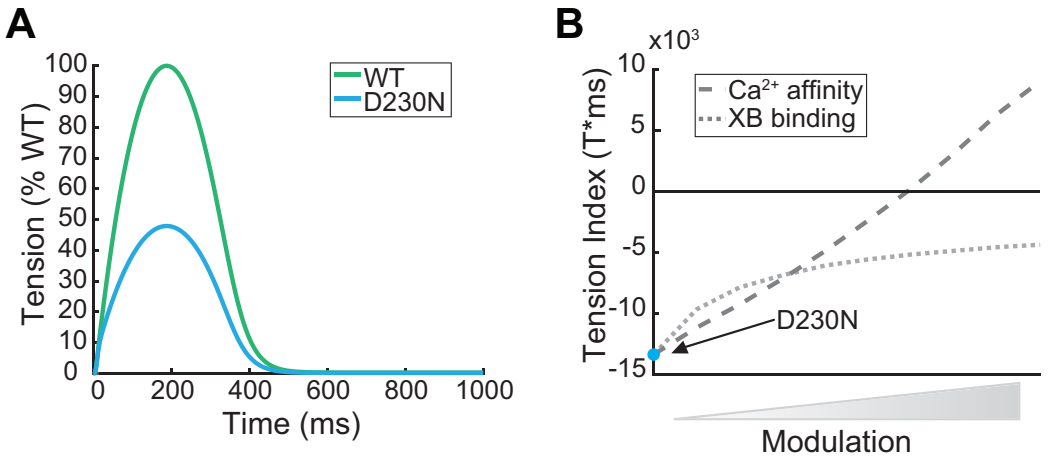

Figure 4.2. (A) Model simulated twitches for WT and D230N. (B) Dependence of the tension index of simulated D230N twitches on modulation of crossbridge or Ca^{2+} binding. The simulated tension index for D230N twitches without any modulation is indicated by the blue circle. The rate of crossbridge transition from a weak to a strong (tension-generating) state was independently increased to simulate D230N twitches with augmented crossbridge binding (dotted line). The affinity of Ca^{2+} for cTnC was also independently increased to simulate twitches of D230N cardiomyocytes with augmented Ca^{2+} sensitivity (dashed line).

Table 4.1. Fold-changes in parameters used in the Negroni-Lascano model [143] simulate D230N twitches with different inotropic targets

Simulated Twitch	Y_b	Z_b	Y_r	Z_r	f	g	Z_p	Y_p	g_d	Z_q	Y_q
WT	1	1	1	1	1	1	1	1	1	1	1
D230N	1	1	1	1	0.435	1	1	1	1	1	1
D230N + crossbridge modulator	1	1	1	1	0.435	0.9-0.5	0.9-0.5	2-10	1	1	1
D230N + Ca^{2+} modulator	2-9	0.9-0.5	0.9-0.5	2-10	0.435	1	1	1	1	1	1

4.4.2 Increasing Calcium Sensitivity Using the cTnC L48Q Mutation Successfully Augments Twitch Tension-Time Integrals of D230N-Tm Hearts

Our simulated twitches suggest that the TI of D230N cardiomyocytes can be greatly increased by augmenting Ca^{2+} binding to cTnC. The L48Q-cTnC mutation has been shown to increase Ca^{2+} sensitivity [36, 204, 217, 47, 187, 90, 155], so Powers *et al.* hypothesized that double transgenic (DTG) mice carrying both of these mutations would have a phenotype similar to WT [165]. A structural model of the cardiac thin filament [224, 225, 120, 4] showed that the L48Q-cTnC variant likely augments the Ca^{2+} sensitivity of thin filaments containing D230N-Tm by allosterically increasing the strength of the cTnC–cTnI interaction [165]. Results from the DTG (D230N/L48Q) mouse model showed increased Ca^{2+} sensitivity and improved contractility, and DTG mice did not develop a DCM phenotype compared to D230N mice [165], thus validating our computational predictions. Therefore, computational simulations can be utilized to target the TI to successfully predict interventions to prevent the development of DCM for specific sarcomeric mutations.

4.5 Discussion and Conclusions

This study provides an example of how computational modeling can be utilized to test different interventions and predict an optimal strategy based on the underlying genetic perturbation. These predictions can then be tested experimentally. The TI provides one useful tool to assess this, which can also be applied to inotropes like dATP, but other strategies, including adjusting rates in the sarcomere model to match experimental data as was done in Chapters 1 and 2, can also provide useful information. This approach can provide useful information for identifying new potential gene therapy approaches as more genetic sequencing becomes available and additional mutations of interest in heart failure are identified. L48Q cTnC was successfully utilized to treat post-myocaridal infarction development of heart failure in rat and mouse models [204, 47, 187], and computational modeling can aid in the identification of

similar therapeutics in the future, building on work done by others in modeling and gene therapy [37, 36, 96, 205, 163, 67].

In this study, we utilized a relatively simple ODE sarcomere model to simulate twitch kinetics. We were able to match the TI of WT and D230N twitches measured experimentally well with this model, and our model predictions on increasing Ca^{2+} sensitivity were validated experimentally, suggesting that this model is detailed enough to achieve the aims of this study. Still, a spatially explicit model such as the one utilized in Chapter 1 [123] would provide more detail on cooperative thin filament mechanisms and could be better integrated with findings from MD studies to provide greater mechanistic insight into this mutation and its interactions with cTnC L48Q.

Further, this analysis could be expanded to include larger scale simulations of ventricular function, utilizing the framework developed in Chapter 2, and validated against experimental echocardiography data. This would allow us to extend this approach to predict not only how mutations will affect the TI and twitch kinetics, but also larger scale ventricular function before testing in animals or humans. This may prove important in assessing, for example, whether delayed or faster twitch relaxation may impair or improve ventricular function, since the TI does not explicitly account for these effects. Further, this modeling approach could be extended to include longer term growth and remodling to predict development of a DCM or HCM phenotype, and to tune optimal timing of gene delivery to prevent or reverse this.

4.6 Acknowledgements

Chapter 4, in part, is a reprint of material as it appears in J. D. Powers, K. B. Kooiker, A. B. Mason, A. E. Teitgen, G. V. Flint, J. C. Tardiff, S. D. Schwartz, A. D. McCulloch, M. Regnier, J. Davis, and F. Moussavi-Harami. Modulating the tension-time integral of the cardiac twitch prevents dilated cardiomyopathy in murine hearts. *JCI Insight*, 5(20):e142446, 2020. The dissertation author was a contributing author on this publication, and contributed computational

simulations of WT and D230N twitches, as well as computational predictions on the effects of modulating crossbridge binding and Ca^{2+} sensitivity.

Chapter 5

Conclusions

This work establishes a novel multiscale modeling framework extending from atomic simulations of protein dynamics, to changes in cooperative force production in individual sarcomeres, to viscoelastic cellular mechanics, to alterations in ventricular pump function and energetics in heart failure. Using this framework, we showed that recruitment of myosin into the pool available for crossbridge cycling contributed the most significantly to producing disproportionate increases in force with small fractions of dATP, which held true at all scales of function we investigated. These effects were even more notable in simulations of heart failure. According to our model predictions, the underlying mechanism may depend on a cooperative mechanosensing mechanism. Previously identified mechanisms of dATP including increased actomyosin association *via* changes in electrostatics and faster crossbridge cycling can explain experimental results with higher fractions of dATP, but were insufficient to explain supralinear force increases with 1% dATP. Further, we found that the effects of dATP on SERCA, including increased Ca^{2+} association with dATP, were crucial for increasing the rate of myocyte relaxation and improving energetic function at the ventricular level. This provides promising evidence that dATP may indeed have advantages over other similar inotropes which may slow relaxation and lead to higher energy consumption, and the effects of dATP on Ca^{2+} dynamics counteract these negative effects which may normally be caused by increased myosin recruitment. dATP has the potential to permanently restore function in heart failure, providing a significant advance

over current therapies. Furthermore, we showed that our modeling approach can be extended to investigate other putative therapeutics beyond dATP, including targeted gene therapy. Overall, this work shows how computational modeling may be utilized to integrate experimental data from disparate sources to allow us to gain mechanistic insight, and can in turn be utilized to generate new predictions that can be tested experimentally. This combination of experimental testing and computational modeling provides a powerful path forward in developing next-generation tools for better understanding and treating heart failure.

Our approach has several advantages over existing multiscale modeling frameworks. We carried out more detailed simulations of molecular level protein dynamics and protien-protein association, which we then utilized to constrain larger scale models of the sarcomere and cardiac myocyte. We also incorporated cardiac energetics, and validated our model predictions with experimental data on a specific cardiac therapeutic. Still, our multiscale modeling approach has several limitations, and can be expanded in the future to improve computational predicitons and allow for translation to other therapeutics, and closer translation to the clinic.

5.0.1 Limitations and Future Directions

One limitation of molecular modeling techniques including MD and BD is lack of availability of atomically detailed structures, which is largely limited by computational power. Still, advances in computing are allowing for increasingly advanced simulations. Our simulations of myosin and actomyosin dynamics only included the myosin S1 head, but a complete model of the cardiac thick and thin filaments including multiple myosin heads would improve the accuracy of these simulations. Further, the BD simulations utilized in this work allow myosin to freely diffuse and bind to actin; nucleotides and Ca^{2+} were also allowed to freely diffuse around SERCA from any orientation. This could be improved by adding additional constraints on this movement, or utilizing a spring to model the behavior of myosin as it binds to actin. Further, more recent iterations of the BrownDye software allow for the addition of flexible regions within the protein. This could improve our simulation accuracy, especially in the actin-binding region

of myosin and the nucleotide and Ca^{2+} binding regions of SERCA. Finally, longer simulations, ideally including more steps in the myosin and SERCA chemomechanical cycles, would allow for better assessment of their dynamics in response to dATP binding. Implementing tools such as SEEKR would also allow for better assessment of binding kinetics [215].

The sarcomere model we utilized could be improved by incorporating spatial data. The sarcomere is divided into several zones (P, C, and D), each of which have varying ratios of regulatory proteins. Further, recent single molecule imaging data showed that a greater proportion of myosin heads were in the SRX state in the C zone compared to neighboring zones [161]. This may lead to differential effects of modulators that affect the SRX state, like dATP, in different areas of the sarcomere. Further, mutations that lead to the development of cardiomyopathies do not always have the same degree of penetrance [110], leading to some myosin motors carrying the mutation while others do not. This would be especially important in considering gene therapy approaches such as TnC L48Q, where the penetrance of the gene therapy is also not always 100%. A more detailed spatially explicit sarcomere could incorporate this spatial imaging data and more granular, patient specific mutation information, for instance using techniques employed by Mijailovich *et al.* [132] in a recent study using a spatially explicit model to study varying incorporation of the L48Q and I61Q TnC mutations on twitches.

In this work, we utilized models of both sarcomere mechanics and myocyte electrophysiology, but did not assess the effects of dATP simultaneously on both myosin and SERCA using a coupled excitation-contraction coupling model. In the future, such an approach may provide useful insight into whether there is feedback between buffering of Ca^{2+} on the sarcomere, crossbridge cycling, and Ca^{2+} transient dynamics [25]. Unpublished simulation results suggest that this is not a major contributor to the effects of dATP on Ca^{2+} dynamics, but expanding our analysis to include other ATPase pumps would allow us to further examine alternative mechanisms by which dATP may enhance relaxation. Further, cardiac electrophysiology is affected by heart failure, which was not accounted for in this study and would be important to incorporate in the future [227], in addition to regulation by phosphorylation and other regulatory proteins.

Additional experimental data where force and Ca^{2+} dynamics are measured simultaneously, as well as additional cellular level data where dATP or other small molecules are applied in models of heart failure would also allow for further model development.

We utilized a simplified model of ventricular geometry and hemodynamics in this study, which was sufficient for model predictions of global ventricular function, including EF, CO, SV, and LVDevP. However, to improve model predictions in the future, this modeling framework could be extended to a finite element model. This would allow us to assess changes in regional stresses and strains, as well as transmural heterogeneity, and to incorporate patient-specific geometries. This would be especially important in treating heart failure post-myocardial infarction, where there are differences in regional mechanics due to fibrosis in the scar region [192]. dATP has shown promise as a potential gene therapy approach, and transplantation of human induced pluripotent stem cell-derived cardiomyocytes over-expressing R1R2 successfully improved cardiac function in rat hearts [112]. This approach warrants further investigation in the future, and knowledge of how placement of these stem cells interacts with regional mechanics could be used to guide treatment strategies. These models can also be extended to account for growth and remodeling over time, to make predictions about longer term clinical outcomes and optimal timing of interventions including gene therapy and/or inotropic small molecules in terms of preventing and/or reversing maladaptive remodeling. The modeling framework developed recently by Sharifi *et al.* could be extended to achieve this [185].

Another limitation of this work is that it does not incorporate the spatially explicit, stochastic sarcomere model in Chapter 1 in cell or organ level simulations. We instead chose to utilize a more coarse-grained DAE-based sarcomere model for these simulations. Ideally, we could incorporate a spatially explicit sarcomere model with mechanistic detail like the one utilized in Chapter 1 into a finite element model, allowing us to assess the full mechanisms of small molecule therapeutics like dATP at each spatial scale. However, this poses several computational and numerical challenges. First, solving a stochastic model within an DAE, ODE, or PDE modeling framework can be challenging numerically. There are techniques that can be

utilized to accomplish this [236, 139], but computational expense is still often the limiting factor. There are additional challenges and potential instabilities that arise when integrate DAEs at the cellular level with PDEs in a finite element model of the ventricle. This has been approached using techniques like operator splitting or updating [25]. Further, our spatially explicit model would need to be adapted to allow for simulation of muscle shortening, rather than just isometric twitch generation. This could be done using a framework similar to previous ODE sarcomere models [174]. However, it is still important to assess exactly how much mechanistic detail is needed at each scale to answer the questions posed by the study.

Finally, this modeling approach relies on optimization of several parameters. We tried to limit the amount of optimization done, and primarily carried out optimization for fitting to baseline experimental data. Further, we were interested in modeling a specific drug with extensive existing experimental data. However, optimization approaches can still be prone to error from local minima and overfitting. Uncertainty quantification techniques are one way to avoid some of these challenges [3]. In general, machine learning techniques can provide another way to avoid overfitting, quantify uncertainty, and expand this approach to assess new mutations and potential small molecules or gene therapy approaches [5]. A recent study utilized machine learning approaches to assess how shape features of a cardiac twitch relate to underlying changes in rate constants, and how this relates to disease phenotype [6]. Further, artificial intelligence has been successfully utilized for drug screening [154, 34]. As the field of artificial intelligence continues to grow, it can provide a powerful tool for assessing new information on novel mutations that lead to heart failure, and determining optimal treatment approaches.

Bibliography

[1] *The PyMOL Molecular Graphics System, Version 2.0 Schrödinger, LLC*, 2015.

[2] *San Diego Supercomputer Center: Triton Shared Computing Cluster. University of California, San Diego*, 2023.

[3] M. Abdar, F. Pourpanah, S. Hussain, D. Rezazadegan, L. Liu, M. Ghavamzadeh, P. Fieguth, X. Cao, A. Khosravi, U. R. Acharya, V. Makarenkov, and S. Nahavandi. A review of uncertainty quantification in deep learning: Techniques, applications and challenges. *Inf. Fusion*, 76:243–297, 2021.

[4] S. Abdullah, M. L. Lynn, M. T. McConnell, M. M. Klass, A. P. Baldo, S. D. Schwartz, and J. C. Tardiff. Fret-based analysis of the cardiac troponin t linker region reveals the structural basis of the hypertrophic cardiomyopathy-causing δ160e mutation. *J. Biol. Chem.*, 294(40):14634–14647, 2019.

[5] M. Alber, A. B. Tepole, W. R. Cannon, S. De, S. Dura-Bernal, K. Garikipati, G. Karniadakis, W. W. Lytton, P. Perdikaris, L. Petzold, and E. Kuhl. Integrating machine learning and multiscale modeling—perspectives, challenges, and opportunities in the biological, biomedical, and behavioral sciences. *NPJ Digit. Med.*, 2:115, 2019.

[6] A. Asencio, S. Malingen, K. B. Kooiker, J. D. Powers, J. Davis, T. Daniel, and F. Moussavi-Harami. Machine learning meets monte carlo methods for models of muscle's molecular machinery to classify mutations. *J. Gen. Physiol.*, 155(5):e202213291, 2023.

[7] F. Asiri, M. I. H. Siddiqui, M. A. Ali, T. Alam, D. Dobrotă, R. Chicea, and R. D. Dobrotă. Mathematical modeling of active contraction of the human cardiac myocyte: A review. *Heliyon*, 9(9):e20065, 2023.

[8] R. D. Astumian. Huxley's model for muscle contraction revisited: The importance of microscopic reversibility. *Top. Curr. Chem.*, 369:285–316, 2015.

[9] D. Auguin, J. Robert-Paganin, S. Réty, C. Kikuti, A. David, G. Theumer, A. W. Schmidt, H. Knölker, and A. Houdusse. Omecamtiv mecarbil and mavacamten target the same myosin pocket despite antagonistic effects in heart contraction. *bioRxiv*, 2023.

[10] H. E. Autzen and M. Musgaard. In M. Bublitz, editor, *P-Type ATPases: Methods and Protocols*, Methods Mol. Biol., page 459. Springer, New York, NY, 2016.

[11] N. A. Baker, D. Sept, S. Joseph, M. J. Holst, and J. A. McCammon. Electrostatics of nanosystems: Application to microtubules and the ribosome. *Proc. Natl. Acad. Sci. U.S.A.*, 98(18):10037–10041, 2001.

[12] J. N. Bazil, D. A. Beard, and K. C. Vinnakota. Catalytic coupling of oxidative phosphorylation, atp demand, and reactive oxygen species generation. *Biophys. J.*, 110(4):962–971, 2016.

[13] H. M. Berman, J. Westbrook, Z. Feng, G. Gilliland, T. N. Bhat, H. Weissig, I. N. Shindyalov, and P. E. Bourne. The protein data bank. *Nucleic Acids Res.*, 28(1):235–242, 2000.

[14] T. D. Bernier and L. F. Buckley. Cardiac myosin activation for the treatment of systolic heart failure. *J. Cardiovasc. Pharmacol.*, 77(1):4–10, 2021.

[15] D. M. Bers and S. Despa. Cardiac myocytes ca2+ and na+ regulation in normal and failing hearts. *J. Pharmacol. Sci.*, 100(5):315–322, 2006.

[16] R. J. Bick, L. M. Buja, W. B. Van Winkle, and G. E. Taffet. Membrane asymmetry in isolated canine cardiac sarcoplasmic reticulum: comparison with skeletal muscle sarcoplasmic reticulum. *J. Membr. Biol.*, 164(2):169–175, 1998.

[17] M. W. Bloom, B. Greenberg, T. Jaarsma, J. L. Januzzi, C. S. P. Lam, A. P. Maggioni, J. Trochu, and J. Butler. Heart failure with reduced ejection fraction. *Nat. Rev. Dis. Primers*, 3:17058, 2017.

[18] M. Brini and E. Carafoli. Calcium pumps in health and disease. *Physiol. Rev.*, 89(4):1341–1378, 2009.

[19] M. Bublitz, M. Musgaard, H. Poulsen, L. Thøgersen, C. Olesen, B. Schiøtt, J. P. Morth, J. V. Møller, and P. Nissen. Ion pathways in the sarcoplasmic reticulum ca2+-atpase. *J. Biol. Chem.*, 288(15):10759–10765, 2013.

[20] K. S. Campbell. Impact of myocyte strain on cardiac myofilament activation. *Pflügers Archiv: European Journal of Physiology*, 462(1):3–14, 2011.

[21] K. S. Campbell, B. S. Christman, and S. G. Campbell. Multiscale modeling of cardiovascular function predicts that end-systolic pressure volume relationship can be targeted via multiple therapeutic strategies. *Front. Physiol.*, 11:1043, 2020.

[22] K. S. Campbell, P. M. L. Janssen, and S. G. Campbell. Force-dependent recruitment from the myosin off state contributes to length-dependent activation. *Biophys. J.*, 115(3):543–553, 2018.

[23] S. G. Campbell, S. N. Flaim, C. H. Leem, and A. D. McCulloch. Mechanisms of transmurally varying myocyte electromechanics in an integrated computational model. *Philos. Trans. A. Math Phys. Eng. Sci.*, 366(1879):3361–3380, 2008.

[24] S. G. Campbell, F. V. Lionetti, K. S. Campbell, and A. D. McCulloch. Coupling of adjacent tropomyosins enhances cross-bridge-mediated cooperative activation in a markov model of the cardiac thin filament. *Biophys. J.*, 98(10):2254–2264, 2010.

[25] S. G. Campbell and A. D. McCulloch. Multi-scale computational models of familial hypertrophic cardiomyopathy: genotype to phenotype. *J. R. Soc. Interface*, 8(64):1550–61, 2011.

[26] D. A. Case, K. Belfon, I. Y. Ben-Shalom, S. R. Brozell, D. S. Cerutti, T. E. Cheatham, III, V. W. D. Cruzeiro, T. A. Darden, R. E. Duke, G. Giambasu, M. K. Gilson, H. Gohlke, A. W. Goetz, R. Harris, S. Izadi, S. A. Izmailov, K. Kasavajhala, A. Kovalenko, R. Krasny, T. Kurtzman, T. S. Lee, S. LeGrand, P. Li, C. Lin, J. Liu, T. Luchko, R. Luo, V. Man, K. M. Merz, Y. Miao, O. Mikhailovskii, G. Monard, H. Nguyen, A. Onufriev, F. Pan, S. Pantano, R. Qi, D. R. Roe, A. Roitberg, C. Sagui, S. Schott-Verdugo, J. Shen, C. L. Simmerling, N. R. Skrynnikov, J. Smith, J. Swails, R. C. Walker, J. Wang, L. Wilson, R. M. Wolf, X. Wu, Y. Xiong, Y. Xue, D. M. York, and P. A. Kollman. Amber 2020. *University of California, San Francisco*, 2020.

[27] CDC. Heart failure. 2023.

[28] Y. Cheng, K. A. Hogarth, M. L. O'Sullivan, M. Regnier, and W. G. Pylec. 2-deoxyadenosine triphosphate restores the contractile function of cardiac myofibril from adult dogs with naturally occurring dilated cardiomyopathy. *Am. J. Physiol. Heart Circ. Physiol.*, 310(1):H80–H91, 2016.

[29] M. C. Childers, M. Geeves, V. Daggett, and M. Regnier. Modulation of post-powerstroke dynamics in myosin ii by 2'- deoxy-adp. *Arch. Biochem. Biophys.*, 699:108733, 2021.

[30] M. C. Childers and M. Regnier. In M. C. Childers and M. Regnier, editors, *Familial Cardiomyopathies*, volume 2735 of *Methods Mol. Biol.*, chapter Atomistic simulations of sarcomere proteins. Humana, New York, NY, 2024.

[31] R. Clark, M. A. Ansari, S. Dash, M. A. Geeves, and L. M. Coluccio. Loop 1 of transducer region in mammalian class i myosin, myo1b, modulates actin affinity, atpase activity, and nucleotide access. *J. Biol. Chem.*, 280(35):30935–30942, 2005.

[32] D. M. Clarke, T. W. Loo, G. Inesi, and D. H. MacLennan. Location of high affinity ca2 +-binding sites within the predicted transmembrahe domain of the sarco-plasmic reticulum ca2+-atpase. *Nature*, 339:476–478, 1989.

[33] J. D. Clausen, D. B. McIntosh, B. Vilsen, D. G. Woolley, and J. P. Andersen. Importance of conserved n-domain residues thr441, glu442, lys515, arg560, and leu562 of sarcoplasmic reticulum ca2+-atpase for mgatp binding and subsequent catalytic steps. plasticity of the nucleotide-binding site. *J. Biol. Chem.*, 278(22):20245–20258, 2003.

[34] F. S. Costabal, K. Matsuno, J. Yao, P. Perdikaris, and E. Kuhl. Machine learning in drug development: Characterizing the effect of 30 drugs on the qt interval using gaussian

process regression, sensitivity analysis, and uncertainty quantification. *Comput. Methods Appl. Mech. Eng.*, 348:313–333, 2019.

[35] R. Craig and R. Padrón. Structural basis of the super- and hyper-relaxed states of myosin ii. *J. Gen. Physiol.*, 154(1):e202113012, 2022.

[36] J. Davis, L. C. Davis, R. N. Correll, C. A. Makarewich, J. A. Schwanekamp, F. Moussavi-Harami, D. Wang, A. J. York, H. Wu, S. R. Houser, C. E. Seidman, J. G. Seidman, M. Regnier, J. M. Metzger, J. C. Wu, and J. D. Molkentin. A tension-based model distinguishes hypertrophic versus dilated cardiomyopathy. *Cell*, 165(5):1147–1159, 2016.

[37] J. Davis and J. M. Metzger. Combinatorial effects of double cardiomyopathy mutant alleles in rodent myocytes: a predictive cellular model of myofilament dysregulation in disease. *PLoS One*, 5(2):e9140, 2010.

[38] A. E. Deranek, A. P. Baldo, M. L. Lynn, S. D. Schwartz, and J. C. Tardiff. Structure and dynamics of the flexible cardiac troponin t linker domain in a fully reconstituted thin filament. *Biochemistry*, 61(13):1229–1242, 2022.

[39] S. Dewan, A. Krishnamurthy, D. Kole, G. Conca, R. Kerckhoffs, M. D. Puchalski, J. H. Omens, H. Sun, V. Nigam, and A. D. McCulloch. Model of human fetal growth in hypoplastic left heart syndrome: Reduced ventricular growth due to decreased ventricular filling and altered shape. *Front. Pediatr.*, 5:25, 2017.

[40] T. Doenst, T. D. Nguyen, and E. D. Abel. Cardiac metabolism in heart failure: Implications beyond atp production. *Circ. Res.*, 113(6):709–724, 2013.

[41] T. J. Dolinsky, P. Czodrowski, H. Li, J. E. Nielsen, J. H. Jensen, G. Klebe, and N. A. Baker. Pdb2pqr: expanding and upgrading automated preparation of biomolecular structures for molecular simulations. *Nucleic Acids Res.*, 35(Web Server issue):W522–W525, 2007.

[42] T. J Dolinsky, J. E. Nielsen, J. A. McCammon, and N. A. Baker. Pdb2pqr: an automated pipeline for the setup of poisson-boltzmann electrostatics calculations. *Nucleic Acids Res.*, 32(suppl 2):W665–W667, 2004.

[43] M. H. Doran, E. Pavadai, M. J. Rynkiewicz, J. Walklate, E. Bullitt, J. R. Moore, M. Regnier, M. A. Geeves, and W. Lehman. Cryo-em and molecular docking shows myosin loop 4 contacts actin and tropomyosin on thin filaments. *Biophys. J.*, 119(4):821–830, 2020.

[44] D. Dutta, V. Nguyen, K. S. Campbell, R. Padrón, and R. Craig. Cryo-em structure of the human cardiac myosin filament. *Nature*, 623:853–862, 2023.

[45] J. Eargle, D. Wright, and Z. Luthey-Schulten. Multiple alignment of protein structures and sequences for vmd. *Bioinformatics*, 22(4):504–506, 2006.

[46] A. P. Einholm, B. Vilsen, and J. P. Andersen. Importance of transmembrane segment m1 of the sarcoplasmic reticulum ca2+-atpase in ca2+ occlusion and phosphoenzyme processing. *J. Biol. Chem.*, 279(16):15888–15896, 2004.

[47] E. R. Feest, F. S. Korte, A. Tu, J. Dai, M. V. Razumova, C. E. Murry, and M. Regnier. Thin filament incorporation of an engineered cardiac troponin c variant (l48q) enhances contractility in intact cardiomyocytes from healthy and infarcted hearts. *J. Mol. Cell Cardiol.*, 27:219–227, 2014.

[48] G. M. Felker, S. D. Solomon, B. Claggett, R. Diaz, J. J. V. McMurray, M. Metra, I. Anand, M. G. Crespo-Leiro, U. Dahlström, E. Goncalvesova, J. G. Howlett, P. MacDonald, A. Parkhomenko, J. Tomcsányi, S. A. Abbasi, S. B. Heitner, T. Hucko, S. Kupfer, F. I. Malik, and J. R. Teerlink. Assessment of omecamtiv mecarbil for the treatment of patients with severe heart failure. *JAMA Cardiol.*, 7(1):26–34, 2022.

[49] C. G. Fonseca, M. Backhaus, D. A. Bluemke, R. D. Britten, J. D. Chung, B. R. Cowan, I. D. Dinov, J. P. Finn, P. J. Hunter, A. H. Kadish, D. C. Lee, J. A. C. Lima, P. Medrano-Gracia, K. Shivkumar, A. Suinesiaputra, W. Tao, and A. A. Young. The cardiac atlas project–an imaging database for computational modeling and statistical atlases of the heart. *Bioinformatics*, 27(16):2288–2295, 2011.

[50] G. S. Francis, J. A. Bartos, and S. Adatya. Inotropes. *J. Am. Coll. Cardiol.*, 63(20):2069–2078, 2014.

[51] M. A. Geeves. Dynamic interaction between actin and myosin subfragment 1 in the presence of adp. *Biochemistry*, 28(14):5864–5871, 1989.

[52] A. Gizzi, R. Ruiz-Baier, S. Rossi, A. Laadhari, C. Cherubini, and S. Filippi. *Modeling the heart and the circulatory system, MSA*, volume 14, chapter A three-dimensional continuum model of active contraction in single cardiomyocytes, pages 157–176. Springer, Cham, 2015.

[53] C. C. Goodno. Inhibition of myosin atpase by vanadate ion. *Proc. Natl. Acad. Sci. U.S.A.*, 76(6):2620–2624, 1979.

[54] R. Gordan, J. K. Gwathmey, and L. Xie. Autonomic and endocrine control of cardiovascular function. *World J. Cardiol.*, 7(4):204–214, 2015.

[55] S. Gourinath, D. M. Himmel, J. H. Brown, L. Reshetnikova, A. G. Szent-Gyorgyi, and C. Cohen. Crystal structure of scallop myosin s1 in the pre-power stroke state to 2.6 Å resolution: flexibility and function in the head. *Structure*, 11(12):1621–1627, 2003.

[56] E. Grandi, F. S. Pasqualini, and D. M. Bers. A novel computational model of the human ventricular action potential and ca transient. *J. Mol. Cell. Cardiol.*, 48(1):112–121, 2010.

[57] B. Greenberg, J. Butler, G. M. Felker, P. Ponikowski, A. A. Voors, A. S. Desai, D. Barnard, A. Bouchard, B. Jaski, A. R. Lyon, J. M. Pogoda, J. J. Rudy, and K. M. Zsebo. Cardiovascular diseases and metabolic syndrome. *Lancet*, 387(10024):1178–1186, 2016.

[58] D. M. Greenfield and J. A. Snowden. In E. Carreras, C. Dufour, M. Mohty, and N. Kröger, editors, *Cardiovascular Diseases and Metabolic Syndrome*, The EBMT Handbook:

Hematopoietic Stem Cell Transplantation and Cellular Therapies. 7th Edition., page Chapter 55. Springer, Cham (CH), 2019.

[59] A. Grinzato, D. Auguin, C. Kikuti, N. Nandwani, D. Moussaoui, D. Pathak, E. Kandiah, K. M. Ruppel, J. A. Spudich, A. Houdusse, and J. Robert-Paganin. Cryo-em structure of the folded-back state of human β-cardiac myosin. *Nat. Commun.*, 14:3166, 2023.

[60] J. M. Guccione, K. D. Costa, and A. D. McCulloch. Finite element stress analysis of left ventricular mechanics in the beating dog heart. *J. Biomechanics*, 28(10):1167–1177, 1995.

[61] J. M. Guccione, A. D. McCulloch, and L. K. Waldman. Passive material properties of intact ventricular myocardium determined from a cylindrical model. *J. Biomech. Eng.*, 113(1):42–55, 1991.

[62] T. M. Gupte, F. Haque, B. Gangadharan, M. S. Sunitha, S. Mukherjee, S. Anandhan, D. S. Rani, N. Mukundan, A. Jambekar, K. Thangaraj, R. Sowdhamini, R. F. Sommese, S. Nag, J. A. Spudich, and J. A. Mercer. Mechanistic heterogeneity in contractile properties of -tropomyosin (tpm1) mutants associated with inherited cardiomyopathies. *J. Biol. Chem.*, 290(11):7003–7015, 2015.

[63] K. D. Hammonds and D. M. Heyes. Shadow hamiltonian in classical nve molecular dynamics simulations: A path to long time stability. *J. Chem. Phys.*, 152(2):024114, 2020.

[64] C. Hayward, N. R. Banner, A. Morley-Smith, A. R. Lyon, and S. E. Harding. The current and future landscape of serca gene therapy for heart failure: A clinical perspective. *Hum. Gene Ther.*, 26(5):293–304, 2015.

[65] X. He, V. H. Man, W. Yang, T. Lee, and J. Wang. A fast and high-quality charge model for the next generation general amber force field. *J. Chem. Phys.*, 153(11):114502, 2020.

[66] Y. Himeno, K. Asakura, Y. C. Cha, H. Memida, T. Powell, A. Amano, and A. Noma. A human ventricular myocyte model with a refined representation of excitation-contraction coupling. *Biophys. J*, 109(2):415–427, 2015.

[67] M. Hoshijima, Y. Ikeda, Y. Iwanaga, S. Minamisawa, M. Date, Y. Gu, M. Iwatate, M. Li, L. Wang, J. M. Wilson, Y. Wang, J. Ross Jr, and K. R. Chien. Chronic suppression of heart-failure progression by a pseudophosphorylated mutant of phospholamban via in vivo cardiac raav gene delivery. *Nat. Med.*, 8(8):864–71, 2002.

[68] S. Hua, H. Ma, D. Lewis, G. Inesi, and C. Toyoshima. Functional role of "n" (nucleotide) and "p" (phosphorylation) domain interactions in the sarcoplasmic reticulum (serca) atpase. *Biochemistry*, 41(7):2264–2272, 2002.

[69] Y. Huang, H. Li, and Y. Bu. Molecular dynamics simulation exploration of cooperative migration mechanism of calcium ions in sarcoplasmic reticulum ca2+-atpase. *J. Comput. Chem.*, 30(13):2136–2145, 2009.

[70] G. A. Huber and J. A. McCammon. Browndye: A software package for brownian dynamics. *Comput. Phys. Commun.*, 181(11):1896–1905, 2010.

[71] W. Humphrey, A. Dalke, and K. Schulten. Vmd: Visual molecular dynamics. *J. Mol. Graph.*, 14(1):33–38, 1996.

[72] P. J. Hunter, A. D. McCulloch, and H. E. D. J. ter Keurs. Modelling the mechanical properties of cardiac muscle. *Prog. Biophys. Mol. Biol.*, 69(2–3):289–331, 1998.

[73] A. F. Huxley and R. Niedergerke. Structural changes in muscle during contraction; interference microscopy of living muscle fibres. *Nature*, 173(4412):971–973, 1954.

[74] H. E. Huxley. The mechanism of muscular contraction. *Science*, 164(3886):1356–1366, 1969.

[75] H. E. Huxley and J. Hanson. Changes in the cross-striations of muscle during contraction and stretch and their structural interpretation. *Nature*, 173(4412):973–976, 1954.

[76] H. E. Huxley and R. M. Simmons. Proposed mechanism of force generation in striated muscle. *Nature*, 233:533–538, 1971.

[77] The MathWorks Inc. Matlab version: 9.5.0 (r2018b), 2018.

[78] G. Inesi, M. Kurzmack, C. Coan, and D. E. Lewis. Cooperative calcium binding and atpase activation in sarcoplasmic reticulum vesicles. *J. Biol. Chem.*, 255(7):3025–3031, 1980.

[79] G. Inesi, D. Lewis, C. Toyoshima, A. Hirata, and L. Meis. Conformational fluctuations of the ca2+-atpase in the native membrane environment. effects of ph, temperature, catalytic substrates, and thapsigargin. *J. Biol. Chem.*, 283(2):1189–1196, 2008.

[80] G. Inesi, A. M. Prasad, and R. Pilakatta. The ca2+ atpase of cardiac sarcoplasmic reticulum: physiological role and relevance to diseases. *Biochem. Biophys. Res. Commun.*, 369(1):182, 2008.

[81] S. Izadi, R. Anandakrishnan, and A. V. Onufriev. Building water models: A different approach. *J. Phys. Chem. Lett.*, 5(21):3863–3871, 2014.

[82] A. Jafari, E. Pszczolkowski, and A. Krishnamurthy. A framework for biomechanics simulations using four-chamber cardiac models. *J. Biomech.*, 91:91–101, 2019.

[83] P. M. L. Janssen, L. B. Stull, and E. Marbán. Myofilament properties comprise the rate-limiting step for cardiac relaxation at body temperature in the rat. *Am. J. Physiol. Heart Circ. Physiol.*, 282(2):H499–H507, 2002.

[84] P. B. Joel, H. L. Sweeney, and K. M. Trybus. Addition of lysines to the 50/20 kda junction of myosin strengthens weak binding to actin without affecting the maximum atpase activity. *Biochemistry*, 42(30):9160–9166, 2003.

[85] W. L Jorgensen, J. Chandrasekhar, J. D. Madura, R. W. Impey, and M. L. Klein. Comparison of simple potential functions for simulating liquid water. *J. Chem. Phys.*, 79(2):926–935, 1983.

[86] Y. Kabashima, H. Ogawa, R. Nakajima, and C. Toyoshima. What atp binding does to the ca2+ pump and how nonproductive phosphoryl transfer is prevented in the absence of ca2+. *Proc. Natl. Acad. Sci. U.S.A.*, 117(31):18448–18458, 2020.

[87] S. Kadota, J. Carey, H. Reinecke, J. Leggett, S. Teichman, M. A. Laflamme, C. E. Murry, M. Regnier, and G. G. Mahairas. Ribonucleotide reductase-mediated increase in datp improves cardiac performance via myosin activation in a large animal model of heart failure. *Eur. J. Heart Fail.*, 17(8):772–781, 2015.

[88] A. D. Kaiser, R. Shad, W. Hiesinger, and A. L. Marsden. A design-based model of the aortic valve for fluid-structure interaction. *Biomech. Model Mechanobiol.*, 20(6):2413–2435, 2021.

[89] E. Kayvanpour, T. Mansi, F. Sedaghat-Hamedani, A. Amr, D. Neumann, B. Georgescu, P. Seegerer, A. Kamen, J. Haas, K. S. Frese, M. Irawati, E. Wirsz, V. King, S. Buss, D. Mereles, E. Zitron, A. Keller, H. A Katus, D. Comaniciu, and B. Meder. Towards personalized cardiology: Multi-scale modeling of the failing heart. *PLoS One*, 10(7):e0134869, 2015.

[90] P. M. Kekenes-Huskey, S. Lindert, and J. A. McCammon. Molecular basis of calcium-sensitizing and desensitizing mutations of the human cardiac troponin c regulatory domain: A multi-scale simulation study. *PLOS Comput. Biol.*, 8(11):e1002777, 2012.

[91] P. M. Kekenes-Huskey, V. T. Metzger, B. J. Grant, and J. A. McCammon. Calcium binding and allosteric signaling mechanisms for the sarcoplasmic reticulum ca2+ atpase. *Protein Sci.*, 21(10):1429–1443, 2012.

[92] J. Kennedy and R. Eberhart. Particle swarm optimization. *Proceedings of ICNN'95 - International Conference on Neural Networks, Perth, WA, Australia*, 4:1942–1948, 1995.

[93] R. C. P. Kerckhoffs, J. H. Omens, and A. D. McCulloch. A single strain-based growth law predicts concentric and eccentric cardiac growth during pressure and volume overload. *Mech. Res. Commun.*, 42:40–50, 2012.

[94] S. M. Kim, B. E. Randall, F. Jezek, D. A. Beard, and N. C. Chesler. Computational modeling of ventricular-ventricular interactions suggest a role in clinical conditions involving heart failure. *Front. Physiol.*, 134:1231688, 2023.

[95] J. C. Klein, A. R. Burr, B. Svensson, D. J. Kennedy, J. Allingham, M. A. Titus, I. Rayment, and D. D. Thomas. Actin-binding cleft closure in myosin II probed by site-directed spin labeling and pulsed epr. *Proc. Natl. Acad. Sci. U.S.A.*, 105(35):12867–12872, 2008.

[96] S. C. Kolwicz Jr., G. L. Odom, S. G. Nowakowski, F. Moussavi-Harami, X. Chen, H. Reinecke, S. D. Hauschka, C. E. Murry, G. G. Mahairas, and M. Regnier. Aav6-mediated cardiac-specific overexpression of ribonucleotide reductase enhances myocardial contractility. *Mol. Ther.*, 24(2):240–250, 2016.

[97] F. S. Korte, J. Dai, K. Buckley, E. R. Feest, N. Adamek, M. A. Geeves, C. E. Murry, and M. Regnier. Upregulation of cardiomyocyte ribonucleotide reductase increases intracellular 2 deoxy-atp, contractility, and relaxation. *J. Mol. Cell. Cardiol.*, 51(6):894–901, 2011.

[98] A. Krishnamurthy, C. T. Villongco, J. Chuang, L. R. Frank, V. Nigam, E. Belezzuoli, P. Stark, D. E. Krummen, S. Narayan, J. H. Omens, A. D. McCulloch, and R. C. Kerckhoffs. Patient-specific models of cardiac biomechanics. *J. Comput. Phys.*, 244:4–21, 2013.

[99] N. K. Lakdawala, L. Dellefave, C. S. Redwood, E. Sparks, A. L. Cirino, S. Depalma, S. D. Colan, B. Funke, R. S. Zimmerman, P. Robinson, H. Watkins, C. E. Seidman, J. G. Seidman, E. M. McNally, and C. Y. Ho. Familial dilated cardiomyopathy caused by an alpha-tropomyosin mutation: The distinctive natural history of sarcomeric dilated cardiomyopathy. *J. Am. Coll. Cardiol.*, 55(4):320–329, 2010.

[100] S. Land and S. A. Niederer. A spatially detailed model of isometric contraction based on competitive binding of troponin i explains cooperative interactions between tropomyosin and crossbridges. *PLoS Comput Biol.*, 11(8):e1004376, 2015.

[101] S. Land, S. Park-Holohan, N. P. Smith, C. G. dos Remedios, J. C. Kentish, and S. A. Niederer. A model of cardiac contraction based on novel measurements of tension development in human cardiomyocytes. *J. Mol. Cell Cardiol.*, 106:68–83, 2017.

[102] A. G. Lee and J. M. East. What the structure of a calcium pump tells us about its mechanism. *Biochem. J.*, 356(Pt 3):665–683, 2001.

[103] J. Lee, D. S. Patel, J. Ståhle, S. Park, N. R. Kern, S. Kim, J. Lee, X. Cheng, M. A. Valvano, O. Holst, Y. A. Knirel, Y. Qi, J. Jo, J. B. Klauda, G. Widmalm, and W. Im. Charmm-gui membrane builder for complex biological membrane simulations with glycolipids and lipoglycans. *J. Chem. Theory Comput.*, 15(1):775–786, 2019.

[104] P. Li and K. M. Merz, Jr. Taking into account the ion-induced dipole interaction in the nonbonded model of ions. *J. Chem. Theor. Comput.*, 10(1):289–297, 2014.

[105] P. Li, L. F. Song, and K. M. Merz, Jr. Parameterization of highly charged metal ions using the 12-6-4 lj-type nonbonded model in explicit water. *J. Phys. Chem. B.*, 119(3):883–895, 2015.

[106] P. Li, L. F. Song, and K. M. Merz, Jr. Systematic parameterization of monovalent ions employing the nonbonded model. *J. Chem. Theor. Comput.*, 11(4):1645–1657, 2015.

[107] M. Linari, E. Brunello, M. Reconditi, L. Fusi, M. Caremani, T. Narayanan, G. Piazzesi, V. Lombardi, and M. Irving. Force generation by skeletal muscle is controlled by mechanosensing in myosin filaments. *Nature*, 528:276–279, 2015.

[108] M. A. Lomize, A. L. Lomize, I. D. Pogozheva, and H. I. Mosberg. Opm: orientations of proteins in membranes database. *Bioinformatics*, 22(5):623–625, 2006.

[109] R. Lopez, B. Marzban, X. Gao, E. Lauinger, F. Van den Bergh, S. E. Whitesall, K. Converso-Baran, C. F. Burant, D. E. Michele, and D. A. Beard. Impaired myocardial energetics causes mechanical dysfunction in decompensated failing hearts. *Function (Oxf.)*, 1(2):zqaa018, 2020.

[110] M. Lorenzini, G. Norrish, E. Field, J. P. Ochoa, M. Cicerchia, M. M. Akhtar, P. Syrris, L. R. Lopes, J. P. Kaski, and P. M. Elliott. Penetrance of hypertrophic cardiomyopathy in sarcomere protein mutation carriers. *J. Am. Coll. Cardiol.*, 76(5):550–559, 2020.

[111] J. Lumens, T. Delhaas, B. Kirn, and T. Art. Three-wall segment (triseg) model describing mechanics and hemodynamics of ventricular interaction. *Ann. Biomed. Eng.*, 37(11):2234–2255, 2009.

[112] S. D. Lundy, S. A. Murphy, S. K. Dupras, J. Dai, C. E. Murry, M. A. Laflamme, and M. Regnier. Cell-based delivery of datp via gap junctions enhances cardiac contractility. *J. Mol. Cell. Cardiol.*, 72:350–359, 2014.

[113] C. H. Luo and Y. Rudy. A dynamic model of the cardiac ventricular action potential. i. simulations of ionic currents and concentration changes. *Circ. Res.*, 74(6):1071–1096, 1994.

[114] M. L. Lynn, L. T. Grinspan, T. A. Holeman, J. Jimenez, J. Strom, and J. C. Tardiff. The structural basis of alpha-tropomyosin linked (asp230asn) familial dilated cardiomyopathy. *J. Mol. Cell. Cardiol.*, 108:127–137, 2017.

[115] W. Ma, M. Childers, J. Murray, F. Moussavi-Harami, H. Gong, R. Weiss, V. Daggett, T. Irving, and M. Regnier. Myosin dynamics during relaxation in mouse soleus muscle and modulation by 2-deoxy-atp. *J. Physiol.*, 598(22):5165–5182, 2020.

[116] W. Ma, T. S. McMillen, M. C. Childers, H. Gong, M. Regnier, and T. Irving. Structural off/on transitions of myosin in relaxed porcine myocardium predict calcium-activated force. *Proc. Natl. Acad. Sci. U.S.A.*, 120(5):e2207615120, 2023.

[117] J. A. Maier, C. Martinez, K. Kasavajhala, L. Wickstrom, K. E. Hauser, and C. Simmerling. ff14sb: Improving the accuracy of protein side chain and backbone parameters from ff99sb. *J. Chem. Theor. Comput.*, 11(8):3696–3713, 2015.

[118] F. I. Malik, J. J. Hartman, K. A. Elias, B. P. Morgan, H. Rodriguez, K. Brejc, R. L. Anderson, S. H. Sueoka, K. H. Lee, J. T. Finer, R. Sakowicz, R. Baliga, D. R. Cox, M. Garard, G. Godinez, R. Kawas, E. Kraynack, D. Lenzi, P. P. Lu, A. Muci, C. Niu,

X. Qian, D. W. Pierce, M. Pokrovskii, I Suehiro, S. Sylvester, T. Tochimoto, C. Valdez, W. Wang, T. Katori, D. A. Kass, Y. Shen, S. F. Vatner, and D. J. Morgans. Cardiac myosin activation: A potential therapeutic approach for systolic heart failure. *Science*, 331(6023):1439–1443, 2011.

[119] C. K. Mann, L. C. Lee, K. S. Campbell, and J. F. Wenk. Force-dependent recruitment from myosin off-state increases end-systolic pressure-volume relationship in left ventricle. *Biomech. Model. Mechanobiol.*, 19:2683–2690, 2020.

[120] M. Mark McConnell, L. T. Grinspan, M. R. Williams, M. L. Lynn, B. A. Schwartz, O. Z. Fass, S. D. Schwartz, and J. C. Tardiff. Clinically divergent mutation effects on the structure and function of the human cardiac tropomyosin overlap. *Biochemistry*, 56(26):3403–3413, 2017.

[121] B. Marzban, R. Lopez, and D. A. Beard. Computational modeling of coupled energetics and mechanics in the rat ventricular myocardium. *Physiome*, 2020.

[122] J. Mayourian, E. A. Sobie, and K. D. Costa. An introduction to computational modeling of cardiac electrophysiology and arrhythmogenicity. *Methods Mol. Biol.*, 1816:17–35, 2018.

[123] K. J. McCabe, Y. Aboelkassem, A. E. Teitgen, G. A. Huber, J. A. McCammon, M. Regnier, and A. D. McCulloch. Predicting the effects of datp on cardiac contraction using multiscale modeling of the sarcomere. *Arch. Biochem. Biophys.*, 30(695):108582, 2020.

[124] R. T. McGibbon, K. A. Beauchamp, M. P. Harrigan, C. Klein, J. M. Swails, C. X. Hernández, C. R. Schwantes, L. Wang, T. J. Lane, and V. S. Pande. Mdtraj: A modern open library for the analysis of molecular dynamics trajectories. *Biophys. J.*, 109(8):1528–1532, 2015.

[125] D. F. A. McKillop and M. A. Geeves. Regulation of the interaction between actin and myosin subfragment 1: Evidence for three states of the thin filament. *Biophys. J.*, 65:693–701, 1993.

[126] J. J. V. McMurray. Systolic heart failure. *N. Engl. J. Med.*, 362:228–238, 2010.

[127] E. M. McNally, J. R. Golbus, and M. J. Puckelwartz. Genetic mutations and mechanisms in dilated cardiomyopathy. *J. Clin. Invest*, 123(1):19–26, 2013.

[128] Y. Miao, V. A. Feher, and J. A. McCammon. Gaussian accelerated molecular dynamics: unconstrained enhanced sampling and free energy calculation. *J. Chem. Theory Comput.*, 11(8):3584–3595, 2015.

[129] Y. Miao, W. Sinko, L. Pierce, D. Bucher, R. C. Walker, and J. A. McCammon. Improved reweighting of accelerated molecular dynamics simulations for free energy calculation. *J. Chem. Theory Comput.*, 10(7):2677–2689, 2014.

[130] S. M. Mijailovich, O. Kayser-Herold, B. Stojanovic, D. Nedic, T. C. Irving, and M. A. Geeves. Three-dimensional stochastic model of actin–myosin binding in the sarcomere lattice. *J. Gen. Physiol.*, 148(6):459–488, 2016.

[131] S. M. Mijailovich, M. Prodanovic, C. Poggesi, M. A. Geeves, and M. Regnier. Multiscale modeling of twitch contractions in cardiac trabeculae. *J. Gen. Physiol.*, 153(3):e202012604, 2021.

[132] S. M. Mijailovich, M. Prodanovic, C. Poggesi, J. D. Powers, J. Davis, M. A. Geeves, and M. Regnier. The effect of variable troponin c mutation thin filament incorporation on cardiac muscle twitch contractions. *J. Mol. Cell Cardiol.*, 155:112–124, 2021.

[133] S. Miyamoto and P. A. Kollman. Settle: An analytical version of the shake and rattle algorithm for rigid water models. *J. Comput. Chem.*, 13(8):952–962, 1992.

[134] L. J. Motloch, M. Cacheux, K. Ishikawa, C. Xie, J. Hu, J. Aguero, K. M. Fish, R. J. Hajjar, and F. G. Akar. Primary effect of serca 2a gene transfer on conduction reserve in chronic myocardial infarction. *J. Am. Heart. Assoc.*, 7(18):e009598, 2018.

[135] F. Moussavi-Harami, M. V. Razumova, A. W. Racca, Y. Cheng, A. Stempien-Otero, and M. Regnier. 2-deoxy adenosine triphosphate improves contraction in human end-stage heart failure. *J. Mol. Cell Cardiol.*, 79:256–263, 2015.

[136] B. Mueller, M. Zhao, I. V. Negrashov, R. Bennett, and D. D. Thomas. Serca structural dynamics induced by atp and calcium. *Biochemistry*, 43(40):12846–12854, 2004.

[137] S. P. Murphy, N. E. Ibrahim, and J. L. Januzzi Jr. Heart failure with reduced ejection fraction: A review. *JAMA*, 324(5):488–504, 2020.

[138] M. Musgaard, L. Thøgersen, B. Schiøtt, and E. Tajkhorshidk. Tracing cytoplasmic ca(2+) ion and water access points in the ca(2+)-atpase. *Biophys. J.*, 102(2):268–277, 2012.

[139] J. T. Nardini, R. E. Baker, M. J. Simpson, and K. B. Flores. Learning differential equation models from stochastic agent-based model simulations. *J. R. Soc. Interface*, 18(176):20200987, 2021.

[140] M. P Nash and P. J. Hunter. Computational mechanics of the heart. *J. Elast.*, 61:113–141, 2000.

[141] F. Neese. Software update: the orca program system, version 4.0. *Wiley Interdiscip. Rev. Comput. Mol.*, 8(1):e1327, 2018.

[142] F. Neese and J. Wiley. The orca program system. *Wiley Interdiscip. Rev. Comput. Mol.*, 2(1):73–78, 2012.

[143] J. A. Negroni and E. C. Lascano. Simulation of steady state and transient cardiac muscle response experiments with a huxley-based contraction model. *J. Mol. Cell Cardiol.*, 45(2):300–312, 2008.

[144] D. P. Nickerson, N. P. Smith, and P. J. Hunter. A model of cardiac cellular electromechanics. *Phil. Trans. R. Soc. Lond. A*, 359:1159–1172, 2001.

[145] D. Noble, A. Varghese, P. Kohl, and P. Nobel. Improved guinea-pig ventricular cell model incorporating a diadic space, ikr, and iks, and length- and tension-dependent processes. *Can. J. Cardiol.*, 14:123–134, 1998.

[146] D. A. Nordsletten, S. A. Niederer, M. P. Nash, P. J. Hunter, and N. P. Smith. Coupling multi-physics models to cardiac mechanics. *Prog. Biophys. Mol. Bio.*, 104(1–3):77–88, 2011.

[147] S. G. Nowakowski, S. C. Kolwicz, F. S. Korte, Z. Luo, J. N. Robinson-Hamm, J. L. Page, F. Brozovich, R. S. Weiss, R. Tian, C. E. Murry, and M. Regnier. Transgenic overexpression of ribonucleotide reductase improves cardiac performance. *Proc. Natl. Acad. Sci. U.S.A.*, 110(15):6187–6192, 2013.

[148] S. G. Nowakowski, M. Regnier, and V. Daggett. Molecular mechanisms underlying deoxy-adp.pi activation of pre-powerstroke myosin. *Protein Sci.*, 26(4):749–762, 2017.

[149] NVIDIA, P. Vingelmann, and F. H. P. Fitzek. Cuda, release: 11.7, 2022.

[150] T. O'Hara, L. Virág, A. Varró, and Y. Rudy. Simulation of the undiseased human cardiac ventricular action potential: Model formulation and experimental validation. *PLOS Comput. Biol.*, 7(5):e1002061, 2011.

[151] C. Olesen, T. L. Sørensen, R. C. Nielsen, J. V. Møller, and P. Nissen. Dephosphorylation of the calcium pump coupled to counterion occlusion. *Science*, 306(5705):2251–2255, 2004.

[152] M. H. M. Olsson, C. R. Søndergaard, M. Rostkowski, and J. H. Jensen. Propka3: consistent treatment of internal and surface residues in empirical pka predictions. *J. Chem. Theory Comput.*, 7(2):525–537, 2011.

[153] M. G. Palmgren and P. Nissen. P-type atpases. *Annu. Rev. Biophys.*, 40:243–266, 2011.

[154] P. Parijat, S. Attili, Z. Hoare, M. Shattock, V. Kenyon, and T. Kampourakis. Discovery of a novel cardiac-specific myosin modulator using artificial intelligence-based virtual screening. *Nat. Commun.*, 14(1):7692, 2023.

[155] M. S. Parvatiyar, J. R. Pinto, J. Liang, and J. D. Potter. Predicting cardiomyopathic phenotypes by altering ca2+ affinity of cardiac troponin c. *J. Biol. Chem.*, 285(36):27785–27797, 2010.

[156] M. Peirlinck, F. S. Costabal, K. L. Sack, J. S. Choy, G. S. Kassab, J. M. Guccione, M. De Beule, P. Segers, and E. Kuhl. Using machine learning to characterize heart failure across the scale. *Biomech. Model. Mechanobiol.*, 18:1987–2001, 2019.

[157] M. Peirlinck, F. S. Costabal, J. Yao, J. M. Guccione, S. Tripathy, Y. Wang, D. Ozturk, P. Segars, T. M. Morrison, S. Levine, and E. Kuhl. Precision medicine in human heart modeling: Perspectives, challenges, and opportunities. *Biomech. Model. Mechanobiol.*, 20:803–831, 2021.

[158] M. Periasamy and S. Huke. Serca pump level is a critical determinant of ca2+ homeostasis and cardiac contractility. *J. Mol. Cell. Cardiol.*, 33(6):1053–1063, 2001.

[159] E. F. Pettersen, T. D. Goddard, C. C. Huang, G. S. Couch, D. M. Greenblatt, E. C. Meng, and T. E. Ferrin. Ucsf chimera — a visualization system for exploratory research and analysis. *J. Comput. Chem.*, 25(13):1605–1612, 2004.

[160] B. Pieske, L. S. Maier, V. Piacentino 3rd, J. Weisser, G. Hasenfuss, and S. Houser. Rate dependence of [na+]i and contractility in nonfailing and failing human myocardium. *Circulation*, 106(4):447–453, 2002.

[161] M. Pilagov, L. W. H. J. Heling, J. Walklate, M. A. Geeves, and N. M. Kad. Single-molecule imaging reveals how mavacamten and pka modulate atp turnover in skeletal muscle myofibrils. *J. Gen. Physiol.*, 155(1):e202213087, 2023.

[162] V. J. Planelles-Herrero, J. J. Hartman, J. Robert-Paganin, F. I. Malik, and A. Houdusse. Mechanistic and structural basis for activation of cardiac myosin force production by omecamtiv mecarbil. *Nat. Commun.*, 8:190, 2017.

[163] S. T. Pleger, C. Shan, J. Ksienzyk, R. Bekeredjian, P. Boekstegers, R. Hinkel, S. Schinkel, B. Leuchs, J. Ludwig, G. Qiu, C. Weber, P. Raake, W. J. Koch, H. A. Katus, O. J. Müller, and P. Most. Cardiac aav9-s100a1 gene therapy rescues post-ischemic heart failure in a preclinical large animal model. *Sci. Transl. Med.*, 3(92):92ra64, 2011.

[164] S. M. Pogwizd, K. Schlotthauer, L. Li, W. Yuan, and D. M. Bers. Roles of sodium-calcium exchange, inward rectifier potassium current, and residual -adrenergic responsiveness. *Circ. Res.*, 88:1159–1167, 2001.

[165] J. D. Powers, K. B. Kooiker, A. B. Mason, A. E. Teitgen, G. V. Flint, J. C. Tardiff, S. D. Schwartz, A. D. McCulloch, M. Regnier, J. Davis, and F. Moussavi-Harami. Modulating the tension-time integral of the cardiac twitch prevents dilated cardiomyopathy in murine hearts. *Proc. Natl. Acad. Sci. U.S.A.*, 166(23):11502–11507, 2019.

[166] J. D Powers, C. D. Williams, M. Regnier, and T. L. Daniel. A spatially explicit model shows how titin stiffness modulates muscle mechanics and energetics. *Integr. Comp. Biol.*, 58(2):186–193, 2018.

[167] J. D. Powers, C. C. Yuan, K. J. McCabe, J. D. Murray, M. C. Childers, G. V. Flint, F. Moussavi-Harami, S. Mohran, R. Castillo, C. Zuzek, W. Ma, V. Daggett, A. D. McCulloch, T. C. Irving, and M. Regnier. Cardiac myosin activation with 2-deoxy-atp via increased electrostatic interactions with actin. *Proc. Natl. Acad. Sci. U.S.A.*, 166(23):11502–11507, 2019.

[168] J. Prinz, H. Wu, M. Sarich, B. Keller, M. Senne, M. Held, J. D. Chodera, C. Schütte, and F. Noé. Markov models of molecular kinetics: generation and validation. *J. Chem. Phys*, 134(17):174105, 2011.

[169] A. Quarteroni, A. Veneziani, and C. Vergara. Geometric multiscale modeling of the cardiovascular system, between theory and practice. *Comput. Methods Appl. Mech. Eng.*, 302:193–252, 2016.

[170] M. Regnier, D. M. Lee, and E. Homsher. Atp analogs and muscle contraction: mechanics and kinetics of nucleoside triphosphate binding and hydrolysis. *Biophys. J.*, 74(6):3044–3058, 1998.

[171] M. Regnier, H. Martin, R. J. Barsotti, A. J. Rivera, D. A. Martyn, and E. Clemmens. Cross-bridge versus thin filament contributions to the level and rate of force development in cardiac muscle. *Biophys. J.*, 87(3):1815–1824, 2004.

[172] M. Regnier, A. J. Rivera, Y. Chen, and P. B. Chase. 2-deoxy-atp enhances contractility of rat cardiac muscle. *Circ. Res.*, 86(12):1211–1217, 2000.

[173] J. J. Rice, M. S. Jafri, and R. L. Winslow. Modeling gain and gradedness of ca2+ release in the functional unit of the cardiac diadic space. *Biophys. J.*, 77(4):1871–1884, 1999.

[174] J. J. Rice, F. Wang, D. M. Bers, and P. P. de Tombe. Approximate model of cooperative activation and crossbridge cycling in cardiac muscle using ordinary differential equations. *Biophys. J.*, 95(5):2368–2390, 2008.

[175] E. K. Rodriguez, A. Hoger, and A. D. McCulloch. Stress-dependent finite growth in soft elastic tissues. *J. Biomech.*, 27(4):455–467, 1994.

[176] D. R. Roe and T. E. Cheatham III. Ptraj and cpptraj: Software for processing and analysis of molecular dynamics trajectory data. *J. Chem. Theory Comput.*, 9(7):3084–3095, 2013.

[177] R. Salomon-Ferrer, D. A. Case, and R. C. Walker. An overview of the amber biomolecular simulation package. *Wiley Interdiscip. Rev. Comput. Mol.*, 3(2):198–210, 2013.

[178] G. Savarese and L. H. Lund. Global public health burden of heart failure. *Card. Fail. Rev.*, 3(1):7–11, 2017.

[179] M. K. Scherer, B. Trendelkamp-Schroer, F. Paul, G. Pérez-Hernández, M. Hoffmann, N. Plattner, C. Wehmeyer, J. Prinz, and F. Noé. Pyemma 2: A software package for estimation, validation, and analysis of markov models. *J. Chem. Theory Comput.*, 11(11):5525–5542, 2015.

[180] B. Schoffstall, A. Clark, and P. B. Chase. Positive inotropic effects of low datp/atp ratios on mechanics and kinetics of porcine cardiac muscle. *Biophys. J.*, 91(6):2216–2226, 2006.

[181] S. Schultze and H. Grubmüller. Time-lagged independent component analysis of random walks and protein dynamics. *J. Chem. Theory Comput.*, 17(9):5766–5776, 2021.

[182] T. Schwede, J. Kopp, N. Guex, and M. C. Peitsch. Swiss-model: An automated protein homology-modeling server. *Nucleic Acids Res.*, 31(13):3381–3385, 2003.

[183] P. M. Seferović, M. Polovina, J. Bauersachs, M. Arad, T. B. Gal, L. H. Lund, S. B. Felix, E. Arbustini, A. L. P. Caforio, D. Farmakis, S. G. Filippatos, E. Gialafos, V. Kanjuh, G. Krljanac, G. Limongelli, A. Linhart, A. R. Lyon, R. Maksimović, D. Miličić, I. Milinković, M. Noutsias, A. Oto, O. Oto, S. U. Pavlović, M. F. Piepoli, A. D. Ristić, G. M. C. Rosano, H. Seggewiss, M. Ašanin, J. P. Seferović, F. Ruschitzka, J. Čelutkiene, T. Jaarsma, C. Mueller, B. Moura, L. Hill, M. Volterrani, Y. Lopatin, Metra M., J. Backs, W. Mullens, O. Chioncel, R. A. de Boer, S. Anker, C. Rapezzi, A. J. S. Coats, and C. Tschöpe. Heart failure in cardiomyopathies: a position paper from the heart failure association of the european society of cardiology. *Eur. J. Heart Fail.*, 21(5):553–576, 2019.

[184] T. R. Shannon, K. S. Ginsburg, and D. M. Bers. Reverse mode of the sarcoplasmic reticulum calcium pump and load-dependent cytosolic calcium decline in voltage-clamped cardiac ventricular myocytes. *Biophys. J.*, 78(1):322–333, 2000.

[185] H. Sharifi, L. C. Lee, K. S. Campbell, and J. F. Wenk. A multiscale finite element model of left ventricular mechanics incorporating baroreflex regulation. *Comput. Biol. Med.*, 168:107690, 2024.

[186] F. Sheikh, K Ouyang, S. G. Campbell, R. C. Lyon, J. Chuang, D. Fitzsimons, J. Tangney, C. G. Hidalgo, C. S. Chung, H. Cheng, N. D. Dalton, Y. Gu, H. Kasahara, M. Ghassemian, J. H. Omens, K. L. Peterson, H. L. Granzier, R. L. Moss, A. D. McCulloch, and J. Chen. Mouse and computational models link mlc2v dephosphorylation to altered myosin kinetics in early cardiac disease. *J. Clin. Invest.*, 122(4):1209–1221, 2012.

[187] V. Shettigar, B. Zhang, S. C. Little, H. E. Salhi, B. J. Hansen, N. Li, J. Zhang, S. R. Roof, H. Ho, L. Brunello, J. K. Lerch, N. Weisleder, V. V. Fedorov, F. Accornero, J. A. Rafael-Fortney, S. Gyorke, P. M. L. Janssen, B. J. Biesiadecki, M. T. Ziolo, and J. P. Davis. Rationally engineered troponin c modulates in vivo cardiac function and performance in health and disease. *Nat. Commun.*, 7:10794, 2016.

[188] F. Sievers and D. G. Higgins. Clustal omega for making accurate alignments of many protein sequences. *Protein Sci.*, 27(1):135–145, 2018.

[189] N. P. Smith, D. P. Nickerson, E. J. Crampin, and P. J. Hunter. Multiscale computational modelling of the heart. *Acta Numerica*, 13:371–431, 2004.

[190] J. E. Stone. An efficient library for parallel ray tracing and animation. page 191–194, 1998.

[191] J. E. Stone, J. Gullingsrud, and K. Schulten. A system for interactive molecular dynamics simulation. 2001.

[192] M. G. Sutton and N. Sharpe. Left ventricular remodeling after myocardial infarction: pathophysiology and therapy. *Circulation*, 101(25):2981–2988, 2000.

[193] C. R. Søndergaard, M. H. M. Olsson, M. Rostkowski, and J. H. Jensen. Improved treatment of ligands and coupling effects in empirical calculation and rationalization of pka values. *J. Chem. Theory Comput.*, 7(7):2284–2295, 2011.

[194] T. L. Sørensen, J. V. Møller, and P. Nissen. Phosphoryl transfer and calcium ion occlusion in the calcium pump. *Science*, 304(5677):1672–1675, 2004.

[195] B. C. W. Tanner, T. L. Daniel, and M. Regnier. Sarcomere lattice geometry influences cooperative myosin binding in muscle. *PLOS Comput. Biol.*, 3(7):e115, 2007.

[196] J. C. Tardiff. Tropomyosin and dilated cardiomyopathy: Revenge of the actinomyosin "gatekeeper". *J. Am. Coll. Cardiol.*, 55(4):330–332, 2010.

[197] J. C. Tardiff. Thin filament mutations: developing an integrative approach to a complex disorder. *Circ. Res.*, 108(6):765–782, 2011.

[198] S. Tariq and W. S. Aronow. Use of inotropic agents in treatment of systolic heart failure. *Int. J. Mol. Sci.*, 16(12):29060–29068, 2015.

[199] K. H. W. ten Tusscher, D. Noble, P. J. Noble, and A. V. Panfilov. A model for human ventricular tissue. *Am. J. Physiol Heart Circ Physiol.*, 286(4):H1573–H1589, 2004.

[200] S. G. Tewari, S. M. Bugenhagen, B. M. Palmer, and D. A. Beard. Dynamics of cross-bridge cycling, atp hydrolysis, force generation, and deformation in cardiac muscle. *J. Mol. Cell Cardiol.*, 96:11–25, 2016.

[201] S. G. Tewari, S. M. Bugenhagen, K. C. Vinnakota, J. J. Rice, P. M. L. Janssen, and D. A. Beard. Influence of metabolic dysfunction on cardiac mechanics in decompensated hypertrophy and heart failure. *J. Mol. Cell Cardiol.*, 94:162–175, 2016.

[202] K. S. Thomson, G. L. Odom, C. E. Murry, G. G. Mahairas, F. Moussavi-Harami, S. L. Teichman, X. Chen, S. D. Hauschka, J. S. Chamberlain, and M. Regnier. Translation of cardiac myosin activation with 2-deoxy-atp to treat heart failure via an experimental ribonucleotide reductase-based gene therapy. *J. Am. Coll. Cardiol. Basic Trans. Science*, 1(7):666–679, 2016.

[203] C. Tian, K. Kasavajhala, ZK. A. A. Belfon, L. Raguette, H. Huang, A. N. Migues, J. Bickel, Y. Wang, J. Pincay, Q. Wu, and C. Simmerling. ff19sb: amino-acid-specific protein backbone parameters trained against quantum mechanics energy surfaces in solution. *J. Chem. Theory Comput.*, 16(1):528–552, 2020.

[204] S. B. Tikunova and J. P. Davis. Designing calcium-sensitizing mutations in the regulatory domain of cardiac troponin c. *J. Biol. Chem.*, 279(34):35341–35352, 2004.

[205] L. Tilemann, K. Ishikawa, T. Weber, and R. J. Hajjar. Gene therapy for heart failure. *Circ. Res.*, 110(5):777–93, 2012.

[206] C. Toyoshima. Structural aspects of ion pumping by ca2+-atpase of sarcoplasmic reticulum. *Arch. Biochem. Biophys.*, 476(1):3–11, 2008.

[207] C. Toyoshima, S. Iwasawa, H. Ogawa, A. Hirata, J. Tsueda, and G. Inesi. Crystal structures of the calcium pump and sarcolipin in the mg2+-bound e1 state. *Nature*, 495(7440):260–264, 2013.

[208] C. Toyoshima and T. Mizutani. Crystal structure of the calcium pump with a bound atp analogue. *Nature*, 430(6999):529–535, 2004.

[209] C. Toyoshima, M. Nakasako, H. Nomura, and H. Ogawa. Crystal structure of the calcium pump of sarcoplasmic reticulum at 2.6 a resolution. *Nature*, 405(6787):647–655, 2000.

[210] K. Tran, N. P. Smith, D. S. Loiselle, and E. J. Crampin. A thermodynamic model of the cardiac sarcoplasmic/endoplasmic ca(2+) (serca) pump. *Biophys. J.*, 96(5):2029–2042, 2009.

[211] B. Trendelkamp-Schroer, H. Wu, F. Paul, and F. Noé. Estimation and uncertainty of reversible markov models. *J. Chem. Phys.*, 143(17):174101, 2015.

[212] T. Tsuji, F. del Monte, Y. Yoshikawa, T. Abe, J. Shimizu, C. Nakajima-Takenaka, S. Taniguchi, R. J. Hajjar, and M. Takaki. Rescue of ca2+ overload-induced left ventriclur dysfunction by targeted ablation of phospholamban. *Am. J. Physiol. Heart Circ. Physiol.*, 296(2):H310–H317, 2009.

[213] G. Van Rossum and F. L. Drake. *Python 3 Reference Manual*. CreateSpace, Scotts Valley, CA, 2009.

[214] J. von der Ecken, M. Müller, W. Lehman, D. J. Manstein, P. A. Penczek, and S. Raunser. Structure of the f-actin–tropomyosin complex. *Nature*, 519(7541):114–117, 2015.

[215] L. W. Votapka, B. R. Jagger, A. L. Heyneman, and R. E. Amaro. Seekr: Simulation enabled estimation of kinetic rates, a computational tool to estimate molecular kinetics and its application to trypsin-benzamidine binding. *J. Phys. Chem. B*, 121(15):3597–3606, 2018.

[216] J. Walklate, K. Kao, M. Regnier, and M. A. Geeves. Exploring the super-relaxed state of myosin in myofibrils from fast-twitch, slow-twitch, and cardiac muscle. *J. Biol. Chem.*, 298(3):101640, 2022.

[217] D. Wang, I. M. Robertson, M. X. Li, M. E. McCully, M. L. Crane, Z. Luo, A. Tu, V. Daggett, B. D. Sykes, and M. Regnier. Structural and functional consequences of the cardiac troponin c l48q ca2+-sensitizing mutation. *Biochemistry*, 51(22):4473–4487, 2012.

[218] J. Wang, P. R. Arantes, A. Bhattarai, R. V. Hsu, S. Pawnikar, Y. M. Huang, G. Palermo, and Y. Miao. Gaussian accelerated molecular dynamics (gamd): principles and applications. *Wiley Interdiscip. Rev. Comput. Mol. Sci.*, 11(5):e1521, 2021.

[219] J. Wang, W. Wang, P. A. Kollman, and D. A. Case. Automatic atom type and bond type perception in molecular mechanical calculations. *J. Mol. Graph. Model.*, 25(2):247–260, 2006.

[220] J. Wang, R. M. Wolf, J. W. Caldwell, P. A. Kollman, and D. A. Case. Development and testing of a general amber force field. *J. Comput. Chem.*, 25(9):1157–1174, 2004.

[221] B. Webb and A. Sali. Comparative protein structure modeling using modeller. *Curr. Protoc. Protein Sci.*, 86(2.9.1–2.9.37), 2016.

[222] H. D. White and E. W. Taylor. Energetics and mechanism of actomyosin adenosine triphosphatase. *Biochemistry*, 15(26):5818–5826, 1976.

[223] C. D. Williams, M. K. Salcedo, T. C. Irving, M. Regnier, and T. L. Daniel. The length–tension curve in muscle depends on lattice spacing. *Proc. Royal Soc. B*, 280(1766):20130697, 2013.

[224] M. R. Williams, S. J. Lehman, J. C. Tardiff, and S. D. Schwartz. Atomic resolution probe for allostery in the regulatory thin filament. *Proc. Natl. Acad. Sci. USA*, 113(12):3257–62, 2016.

[225] M. R. Williams, J. C. Tardiff, and S. D. Schwartz. Mechanism of cardiac tropomyosin transitions on filamentous actin as revealed by all-atom steered molecular dynamics simulations. *J. Phys. Chem. Lett.*, 9(12):3301–3306, 2018.

[226] D. A. Winkelmann, E. Forgacs, M. T. Miller, and A. M. Stock. Structural basis for drug-induced allosteric changes to human -cardiac myosin motor activity. *Nat. Commun.*, 6:7974, 2015.

[227] R. L. Winslow, J. Rice, S. Jafri, E. Marbán, and B. O'Rourke. Mechanisms of altered excitation-contraction coupling in canine tachycardia-induced heart failure, ii: model studies. *Circ. Res.*, 84(5):571–586, 1999.

[228] C. M. Witzenburg and J. W. Holmes. Predicting the time course of ventricular dilation and thickening using a rapid compartmental model. *J. Cardiovasc. Transl. Res.*, 11(2):109–122, 2018.

[229] F. Wu, E. Y. Zhang, J. Zhang, R. J. Bache, and D. A. Beard. Phosphate metabolite concentrations and atp hydrolysis potential in normal and ischaemic hearts. *J. Physiol.*, 586(Pt 17):4193–4208, 2008.

[230] C. Xi, G. S. Kassab, and L. C. Lee. Microstructure-based finite element model of left ventricle passive inflation. *Acta Biomater.*, 90:241–253, 2019.

[231] X. Zhang, Z. Liu, K. S. Campbell, and J. F. Wenk. Evaluation of a novel finite element model of active contraction in the heart. *Front. Physiol.*, 9:425, 2018.

[232] Y. Zhang, V. H. Barocas, S. A. Berceli, C. E. Clancy, D. M. Eckmann, M. Garbey, G. S. Kassab, D. R. Lochner, A. D. McCulloch, R. Tran-Son-Tay, and N. A Trayanova. Multi-scale modeling of the cardiovascular system: disease development, progression, and clinical intervention. *Ann. Biomed. Eng.*, 44(9):2642–2660, 2016.

[233] Y. Zhang, X. Liang, J. Ma, Y. Jing, M. J. Gonzales, C. Villongco, A. Krishnamurthy, L. R. Frank, V. Nigam, P. Stark, S. M. Narayan, and A. D. McCulloch. An atlas-based geometry pipeline for cardiac hermite model construction and diffusion tensor reorientation. *Med. Image Anal.*, 16(6):1130–1141, 2012.

[234] Z. Zhang, D. Lewis, C. Strock, G. Inesi, M. Nakasako, H. Nomura, and C. Toyoshima. Detailed characterization of the cooperative mechanism of ca2+ binding and catalytic activation in the ca2+ transport (serca) atpase. *Biochemistry*, 39:8758–8767, 2000.

[235] L. Zhihao, N. Jingyu, L. Lan, S. Michael, G. Rui, B. Xiyun, L. Xiaozhi, and F. Guanwei. Serca2a: a key protein in the ca2+ cycle of the heart failure. *Heart Fail. Rev.*, 25(3):523–535, 2020.

[236] B. Øksendal. *Stochastic Differential Equations*. Springer Berlin, Heidelberg, 2003.